

**SURFACE AND INTERFACIAL REACTIONS INVOLVING
INORGANIC AND ORGANIC SEMICONDUCTOR SUBSTRATES**

CAI QINJIA

NATIONAL UNIVERSITY OF SINGAPORE

2006

**SURFACE AND INTERFACIAL REACTIONS INVOLVING
INORGANIC AND ORGANIC SEMICONDUCTOR SUBSTRATES**

CAI QINJIA
(M.S., FUDAN UNIV)

**A THESIS SUBMITTED
FOR THE DEGREE OF DOCTOR OF PHILOSOPHY
DEPARTMENT OF CHEMICAL AND BIOMOLECULAR
ENGINEERING**

NATIONAL UNIVERSITY OF SINGAPORE

2006

ACKNOWLEDGEMENT

First of all, the author would like to express my cordial gratitude to my supervisors, Dr. Furong Zhu and Prof. En-Tang Kang, as well as Prof. Koon-Gee Neoh, for their heartfelt guidance, invaluable suggestions, and profound discussion throughout this work, and for sharing with me their enthusiasm and active research interests, which are the constant source for inspiration accompanying me throughout this project. The valued knowledge I learned from them on how to do research work and how to enjoy it paves my way for this study and for my life-long study.

The author would like to thank Dr. Sheng Li for his kind help in XPS operation, training, and sample analysis. I also would like to thank all my colleagues for their help and encouragement, especially to Dr. Yan Zhang, Dr. Guanghui, Yang, Dr. Luping Zhao, Dr. Guodong Fu, Mr. Fujian Xu, Mr. Ong Kian Soo, and Ms Tan Li wei. In addition, I also appreciate the assistance and cooperation from lab technologists and offices of Institute of Materials Research and Engineering (IMRE) and Department of Chemical and Biomolecular Engineering.

Finally, I would give my most special thank his mother, Mdm Li Aixiang, and his wife, Ms Li Nan, for their continuous love, support, and encouragement.

TABLE OF CONTENTS

ACKNOWLEDGEMENT	I
TABLE OF CONTENTS	II
SUMMARY	IV
NOMENCLATURES	VII
LIST OF FIGURES	IX
LIST OF TABLES	XII
LIST OF PUBLICATIONS	XIII
Chapter 1 Introduction	1
Chapter 2 Literature Survey	7
2.1 Passivation of GaAs surface	8
2.2 Polymer brushes via surface-initiated polymerizations	13
2.3 Fluoropolymer films deposited by plasma polymerization of fluoro-monomers	20
2.4 Organic-metal interfaces in organic electroluminescence	24
Chapter 3 GaAs-Polymer Hybrids via Surface-Initiated Atom Transfer Radical Polymerization of Methyl Methacrylate	32
3.1 Introduction	33
3.2 Experimental	35
3.3 Results and Discussion	41
3.4 Conclusions	58
Chapter 4 ZnO-PMMA Core-Shell Hybrid Nanoparticles via Surface-Initiated Atom Transfer Radical Polymerization and Their Enhanced Optical Properties	59
4.1 Introduction	60

4.2	Experimental	62
4.3	Results and Discussion	65
	4.3.1 Synthesis and Characterization of ZnO-PMMA Hybrids	65
	4.3.2 Morphology and Structure of the Hybrid Nanoparticles	69
	4.3.3 UV-visible Absorption and Photoluminescence Spectra of the ZnO-PMMA Hybrid Nanoparticles	72
4.4	Conclusions	77
Chapter 5	Self-Assembled Monolayers of ZnO Colloidal Quantum Dots (QDs) on 3-Mercaptopropyltrimethoxysilane-Passivated GaAs(100)	78
5.1	Introduction	79
5.2	Experimental	81
5.3	Results and Discussion	83
5.4	Conclusions	91
Chapter 6	Plasma Polymerization and Deposition of Fluoropolymers on Hydrogen-Terminated Si(100) Surfaces	92
6.1	Introduction	93
6.2	Experimental	95
6.3	Results and Discussion	100
	6.3.1 Surface and Interfacial Characterization of Plasma-deposited Fluoro-polymers on Silicon Surface by XPS	100
	6.3.2 Chemical Structure of the Plasma-Deposited Fluoropolymer Films	111
	6.3.3 Surface Topography and Water Contact Angles of the Plasma-Deposited Fluoropolymer Films	118
	6.3.4 Adhesion Characteristics of the Plasma-Deposited Fluoropolymer Films with the hydrogen-terminated	123

silicon Surface.

6.4	Conclusions	126
Chapter 7	Chemical States and Electronic Properties of the Interface Between Aluminium and a Photoluminescent Conjugated Copolymer Containing Europium Complex	127
7.1	Introduction	128
7.2	Experimental	131
7.3	Results and Discussion	135
7.3.1	Evolution of the C 1s core-level spectra upon Al deposition	135
7.3.2	Interaction of Al with the heteratoms of PF6-Eu(dbm) ₂ phen	138
7.3.3	Evolution of the O 1s core-level spectra and migration of oxygen from the bulk to the intersurface	146
7.3.4	Evolution of the UPS spectra upon Al deposition	151
7.4	Conclusions	153
Chapter 8	Conclusions	154
Chapter 9	References	158

SUMMARY

The surface and interfacial interactions involving inorganic and organic semiconductors, such as GaAs, ZnO, Si and a conjugated photoluminescent copolymer containing europium complexes, were studied in the present work.

First of all, GaAs-poly(methyl methacrylate) (GaAs-PMMA) hybrids were successfully synthesized via (i) self-assembled of monolayers (SAMs) of 6-mercaptopropyl-1-hexanol on the fresh HCl-etched GaAs surfaces, (ii) immobilization of atom transfer radical polymerization (ATRP) initiators, and (iii) surface-initiated ATRP of MMA from the GaAs surfaces. The mercaptopropyl coupling agent passivated the GaAs surface by the formation of the Ga-S and As-S bonds, leading to the covalently bonded ATRP initiators on the GaAs surface. Well-defined PMMA brushes layers of controllable thickness were tethered on the GaAs surface. The chemical states of the passivated GaAs surface were not significantly affected by the ATRP process.

Zinc oxide (ZnO)-PMMA core-shell hybrid nanoparticles were prepared via surface-initiated ATRP of MMA from ATRP initiators immobilized on ZnO nanoparticles by acid-base interaction. The ZnO-PMMA hybrid nanoparticles so-prepared could be well-dispersed in THF. Significant enhancements were observed in UV-visible and fluorescence spectroscopies.

A self-assembled monolayer of ZnO colloidal quantum dots (QDs) on the 3-mercaptopropyltrimethoxysilane (MPTMS)-passivated GaAs surface was

demonstrated. Not only does MPTMS act as a coupling agent for the ZnO QDs, but also passivates the GaAs surface through the formation of covalent As-S and Ga-S bonds. Thus, the present study provides a simple approach to the self-assembly of semiconductor ZnO colloidal QDs on an oriented single crystal GaAs substrate with simultaneous passivation. The strategy based on the mercaptosilane coupling agent can be readily extended to the fabrication of micropatterned SAMs of colloidal QDs on GaAs substrates, for example, by microcontact printing.

To investigate interfaces of fluoropolymer/hydrogen terminated silicon (H-Si) and fluoropolymer/oxidized silicon (ox-Si), ultra-thin fluoropolymer films were plasma-deposited on the H-Si surfaces and ox-Si surfaces, using four fluoro-monomers, pentafluorostyrene (PFS), hexafluorobenzene (HFB), 1H,1H,2H-heptadecafluoro-1-decene (HDFD), and perfluoroheptane (PFH). The investigation revealed that the fluorine concentration, including the fluorine concentration at the interface (fluorine bonded to Si atoms) and the fluorine concentration of fluoropolymer films (fluorine bonded to C atoms), on the H-Si surfaces were significantly higher than those on the ox-Si surfaces for all fluoro-monomers. This difference was probably due to the reactive dangling bonds created by the homo-cleavage of the H-Si bonds on the H-Si surface via plasma-induced UV radiation. The X-ray photoelectron spectroscopy (XPS) results indicated the formation of the F-Si bonds and possible Si-C bonds on the H-Si surface. These bonds were probably formed through the interaction of the fluoro-monomer fragments or radicals with the dangling bonds during the plasma polymerization process, resulting in strong adhesion of the fluoropolymer films with

the H-Si surfaces. In addition, time-of-flight secondary ion mass spectrometry (ToF-SIMS) results suggested selective polymerization of the PFS monomer through the vinyl group.

Moreover, the chemical states and electronic properties of the interface between thermally evaporated aluminium and a photoluminescent conjugated copolymer containing 9,9'-dihexylfluorene and europium complex-chelated benzoate units in the main chain (PF6-Eu(dbm)₂phen) were studied *in situ* by XPS and ultraviolet photoelectron spectroscopy (UPS). The changes in C 1s, Eu 3d, N 1s, and Al 2p core-level lineshapes with progressive deposition of aluminium atoms were carefully monitored. Aluminium was found to interact with the conjugated backbone of the copolymer to form Al carbide, Al-O-C complex, and Al(III)-N chelate at the interface. In addition, the europium ions were reduced to the metallic state by the deposited aluminium atoms, which were oxidized and chelated by the 1,10-phenanthroline ligands (phen). The changes in chemical states at the interface suggest that the intramolecular energy transfer process in this copolymer had been affected. Moreover, aluminium also interacted with the bulk-adsorbed oxygen, which migrates to the surface in response to the deposition of aluminium atoms, to form a layer of metal oxides. On the other hand, the evolution of the UPS spectra suggested that the π -states of the conjugated system were affected and an unfavorable dipole layer was induced by the deposited aluminium atoms.

NOMENCLATURES

AFM	Atomic force microscopy
Alq ₃	tris-(8-hydroxyquinoline) aluminum
ATRP	Atom transfer radical polymerization
BE	Binding energy
EA	Electron affinity
FWHM	Full-width at half-maximum
FTIR	Fourier transform infrared
GPC	Gel permeation chromatograph
HEMA	hydroxyethyl methacrylate
H-Si surface	Hydrogen-terminated Silicon surface
HDFD	1H,1H,2H-heptadecafluoro-1-decene
HFB	Hexafluorobenzene
HOMO	Highest occupied molecular orbital
IP	Ionization potential
LUMO	Lowest unoccupied molecular orbital
Me ₆ tren	Tris(2-(dimethylamino)ethyl)amine
MMA	Methyl methacrylate
OLEDs	Organic light-emitting diodes
ox-Si	Oxidized Silicon surface
PFH	Perfluoroheptane
PFS	Pentafluorostyrene

Phen	1,10-Phenanthroline
PL	Photoluminescence
PLEDs	Polymer light-emitting diodes
PMMA	Poly(methyl methacrylate)
PPV	poly(p-phenylene vinylene)
QDs	Quantum dots
RF	Radio Frequency
R _a	Average surface roughness
scm	Standard cubic centimeter per min
SAMs	Self-assembled of monolayers
THF	Tetrahydrofuran
ToF-SIMS	Time-of-flight secondary ion mass spectrometry
XPS	X-ray photoelectron spectroscopy
UPS	Ultraviolet photoelectron spectroscopy
VL	Vacuum level

LIST OF FIGURES

- Figure 2.1 Schematic illustration of the process for the preparation of multilayer nanoporous fluoropolymer film.
- Figure 2.2 Schematic of an organic-metal interface energy diagram (a) without and (b) with an interface dipole and (c) UPS spectra of metal and organic.
- Figure 3.1 Schematic illustration of surface passivation, covalent immobilization of ATRP initiators on the GaAs surface, and surface-initiate ATRP to form the GaAs-PMMA hybrids.
- Figure 3.2 XPS Ga 3d and As 3d core-level spectra of the pristine GaAs(100) surface.
- Figure 3.3 XPS Ga 3d and As 3d core-level spectra the HCl-etched GaAs(100) surface.
- Figure 3.4 XPS Ga 3d and As 3d core-level spectra of the GaAs-R₁OH surface.
- Figure 3.5 XPS core-level spectra of the GaAs-R₁OH surface in the region of S 2p.
- Figure 3.6 XPS Br 3d core-level and wide scan spectra of GaAs-R₂Br surface.
- Figure 3.7 The relationship between the average degree of polymerization (DP) and the conversion of MMA monomer. Reaction condition: [MMA]:[CuBr]:[Cu(Br)₂]:[Me₆TREN]:[ethyl-2-bromo-2-methylpropionate] = 500:1:0.1:1.1:1, room temperature and under an argon atmosphere.
- Figure 3.8 Structure of tris(2-(dimethylamino)ethyl)amine (Me₆tren).
- Figure 3.9 XPS spectra of C 1s and wide scan of the GaAs-PMMA hybrids (Sample PMMA1, Table 3.2) surface.
- Figure 3.10 XPS Ga 3d and As 3d core-level spectra of the GaAs-PMMA hybrids interface (Sample PMMA1, Table 3.2).
- Figure 3.11 AFM images of (a) the HCl-etched GaAs surface and (b) the GaAs-PMMA hybrid (Sample GaAs-PMMA4, Table 3.2) surface.
- Figure 4.1 Schematic illustration of immobilization of ATRP initiators on the surface of ZnO nanoparticles and the surface-initiated ATRP to give rise to the ZnO-PMMA core-shell hybrids nanoparticles.

- Figure 4.2 XPS core-level and wide scan spectra of (a) pristine ZnO nanoparticles, (b) the ZnO-R₁Br nanoparticle, and (c) the ZnO-PMMA hybrid nanoparticles with ATRP time of 5 h. the inset in the (a) the Auger LMM spectra of pristine of ZnO nanoparticles.
- Figure 4.3 Representative FE-SEM images of (a) the pristine ZnO nanoparticles and (b) the ZnO-PMMA hybrid nanoparticles after ATRP for 5 h.
- Figure 4.4 Representative TEM images of the ZnO-PMMA hybrid nanoparticles after ATRP for (a) 5 h and (b) 16 h.
- Figure 4.5 UV-Visible absorption spectra of PMMA, pristine ZnO, ZnO-PMMA hybrid nanoparticle. Surface-initiated ATRP was performed for 5 h and 16 h.
- Figure 4.6 Figure 4.6 Fluorescence spectra of the pristine ZnO and ZnO-PMMA hybrid nanoparticles after surface-initiated ATRP for 5 h and 16 h. ($\lambda_{\text{ex}} = 375 \text{ nm}$)
- Figure 5.1 Schematic illustration of the self-assembled monolayers of ZnO colloidal QDs on a MPTMS-passivated GaAs(100) substrate.
- Figure 5.2 (a) TEM image of the as-synthesized ZnO colloidal QDs. The inset is the high-resolution TEM image showing the lattice fringes of single ZnO colloidal QDs. (b) Powder X-Ray diffraction spectrum of the as-synthesized ZnO colloidal QDs. (c) UV-visible absorption spectrum of the ZnO colloidal QDs dispersed in ethanol ($\lambda_{1/2}$ locates at 341 nm, corresponding to a band-gap of 3.63 eV; band-gap of bulk ZnO crystals is 3.37 eV). (d) Excitation (dash line) and emission (solid line) spectra of ZnO colloidal QDs dispersed in ethanol.
- Figure 5.3 XPS (a) wide scan, (b) As 3d core-level, and (c) Ga 3d core-level spectra of the MPTMS-passivated GaAs surface, and XPS (d) wide scan spectrum, (e) Zn 2p core-level spectrum, and (f) Zn (LMM) Auger line of ZnO colloidal QDs self-assembled on the MPTMS-passivated GaAs surface. The inset in (a) is the XPS spectrum in the BE region of Si 2p.
- Figure 5.4 AFM images of MPTMS-passivated GaAs surface (a) before and after self-assembly of (b) ZnO-PD, (c) ZnO-HA, and (d) ZnO-ODA colloidal QDs.
- Figure 6.1 XPS Si 2p core-level spectra of (a) the pristine ox-Si surface, (b) HF-etched (Si)100 surface, and (c) F 1s core-level spectrum of the HF-etched Si(100) surface.

- Figure 6.2 XPS wide scan and F 1s core-level spectra of (a) the ultra-thin pp-PFS/H-Si interface and the (b) ultra-thin pp-PFS/ox-Si interface.
- Figure 6.3 XPS wide scan and F 1s core-level spectra of (a) the ultra-thin pp-HFB/H-Si interface and the (b) ultra-thin pp-HFB/ox-Si interface.
- Figure 6.4 XPS wide scan and F 1s core-level spectra of (a) the ultra-thin pp-HDFD/H-Si interface and the (b) ultra-thin pp-HDFD/ox-Si interface.
- Figure 6.5 XPS wide scan and F 1s core-level spectra of (a) the ultra-thin pp-PFH/H-Si interface and the (b) ultra-thin pp-PFH/ox-Si interface.
- Figure 6.6 XPS Si 2p core-level spectra of (a) ultra-thin pp-PFS/H-Si interface, (b) ultra-thin pp-HFB/H-Si interface, (c) ultra-thin pp-HDFD/H-Si interface, and (d) ultra-thin pp-PFH/H-Si interface. The inset is the XPS Si 2p core-level of H-Si surface.
- Figure 6.7 XPS Si 2p core-level spectra of (a) pristine ox-Si surface, (b) ultra-thin pp-PFS/ox-Si interface, (c) ultra-thin pp-HFB/ox-Si interface, (d) ultra-thin pp-HDFD/ox-Si interface, and (e) ultra-thin pp-PFH/ox-Si interface.
- Figure 6.8 FTIR spectra of (a) the pp-PFS film and (b) the pp-HFB film.
- Figure 6.9 FTIR spectra of (a) the pp-HDFD film and (b) the pp-PFH film.
- Figure 6.10 Positive ion ToF-SIMS spectra of the pp-PFS film on the H-Si surface.
- Figure 6.11 Positive ion ToF-SIMS spectra of the pp-HDFD film on the H-Si surface.
- Figure 6.12 Typical AFM image of H-Si(100) surface.
- Figure 6.13 AFM images of the pp-PFS/H-Si surfaces with film thicknesses of (a) 2 nm and (b) 260 nm, and the pp-HFB/H-Si surfaces with film thicknesses of (c) 2 nm and (d) 530 nm.
- Figure 6.14 AFM images of the pp-HDFD/H-Si surfaces with film thicknesses of (a) 3.5 nm and (b) 460 nm, and pp-PFH/H-Si surfaces with film thicknesses of (c) 1.6nm and (d) 350 nm.
- Figure 6.15 XPS wide scan spectra of (a) the delaminated pp-PFS/H-Si(100) surface, (b) the delaminated Cu tape surface from the Cu tape/pp-PFS/H-Si(100) assembly, (c) the delaminated pp-HFB/H-Si(100) surface, (d) the delaminated Cu tape surface from the Cu tape/pp-HFB/H-Si(100) assembly, (e) the delaminated pp-HDFD/H-Si(100) surface, (f) the delaminated Cu tape surface from the Cu tape/pp-HDFD/H-Si(100) assembly, and (g) the delaminated pp-PFH/H-Si(100) surface, (h) the

delaminated Cu tape surface from the Cu tape/pp-PFH/H-Si(100) assembly.

- Figure 7.1 Chemical Structure PF6-Eu(dbm)₂phen and the emission spectrum of the PF6-Eu(dbm)₂phen film.
- Figure 7.2 (a-d) Evolution of the C 1s core-level spectra as a function of Al coverage ($\alpha = 90^\circ$).
- Figure 7.3 Evolution of the Eu 3d core-level spectra as a function of Al coverage ($\alpha = 90^\circ$).
- Figure 7.4 Evolution of the Al 2p core-level spectra as a function of Al coverage ($\alpha = 90^\circ$).
- Figure 7.5 Figure 7.5 Surface concentration of Al, expressed as the [Al]/[C] ratios, measured at take-off angles of $\alpha = 20^\circ$ and 90° , at different stages of the Al deposition.
- Figure 7.6 Evolution of the N 1s core-level spectra as a function of Al coverage ($\alpha = 90^\circ$).
- Figure 7.7 Evolution of the O 1s spectra at the Al/PF6-Eu(dbm)₂phen interface with increasing Al coverage.
- Figure 7.8 Changes in surface concentration of oxygen as a function of Al coverage.
- Figure 7.9 The evolution of UPS spectra as a function of Al coverage: (a) the pristine polymer, (b) [Al]/[C] = 0.006, 0.3Å, (c) [Al]/[C] = 0.023, 1.3Å, (d) [Al]/[C] = 0.048, 2.7Å, and (e) [Al]/[C] = 0.1, 4.3Å.

LIST OF TABLES

- Table 1.1 Some important inorganic and organic semiconductors
- Table 3.1 XPS analysis of the As 3d, Ga 3d, S 2s, and C 1s core-level spectra.
- Table 3.2 Thickness and surface roughness of the PMMA films grafted on the GaAs(100) substrates
- Table 5.1 Surface morphology of the GaAs substrates
- Table 6.1 Structural assignments of the mass fragments in the ToF-SIMS spectra of the pp-PFS film.
- Table 6.2 Thicknesses, water contact angles, and composition of the plasma-deposited fluoropolymers on H-Si(100) surfaces.

LIST OF PUBLICATIONS

1. Cai, Q.J., G.D. Fu, F.R. Zhu, E.T. Kang, and K.G. Neoh, "GaAs-Polymer Hybrids Formed by Surface-Initiated Atom-Transfer Radical Polymerization of Methyl Methacrylate, *Angew. Chem. Int. Ed.*, 44, pp. 1104-1107. 2005.
2. Cai, Q.J., Q.D. Ling, S. Li, F.R. Zhu, W. Huang, E.T. Kang, and K.G. Neoh, Chemical States and Electronic Properties of the Interface Between Aluminium and a Photoluminescent Conjugated Copolymer Containing Europium Complex, *Appl. Surf. Sci.*, 222, pp. 399-408. 2004.
3. Ling, Q.D., Q.J. Cai, E.T. Kang, K.G. Neoh, F.R. Zhu, and W. Huang, Monochromatic Light-Emitting Copolymer of *N*-Vinylcarbazole and Eu-Complexed 4-Vinylbenzoate and Their Single Layer High Luminance PLEDs, *J. Mater. Chem.*, 14, pp. 2741-2748. 2004.
4. Xu, F.J., Q.J. Cai, Y.L. Li, E.T. Kang, and K.G. Neoh, Covalent Immobilization of Glucose Oxidase on Well-Defined Poly(glycidyl methacrylate)-Si(111) Hybrids from Surface-Initiated Atom-Transfer Radical Polymerization, *Biomacromolecules*, 6, pp. 1012-1020. 2005
5. Xu, F.J., Q.J. Cai, E.T. Kang, K.G. Neoh, Covalent Graft Polymerization and Block Copolymerization Initiated by the Chlorinated SiO₂ (SiO₂-Cl) Moieties of Glass and Oriented Single Crystal Silicon Surfaces, *Macromolecules*, 38, pp. 1051-1054. 2005.
6. Xu, F.J. and Q.J. Cai, E.T. Kang, and K.G. Neoh, Surface-Initiated Atom Transfer Radical Polymerization from Halogen-Terminated Si(111) (Si-X, X) Cl, Br) Surfaces for the Preparation of Well-Defined Polymer-Si hybrids *Langmuir*, 21, pp. 3221-3225. 2005.
7. Xu, F.J., Q.J. Cai, E.T. Kang, K.G. Neoh, and C.X. Zhu, Well-Defined Polymer-Germanium Hybrids via Surface-Initiated Atom Transfer Radical Polymerization on Hydrogen-Terminated Ge(100) Substrates, *Organometallics*, 24, pp. 1768-1771. 2005.

Chapter 1
Introduction

The surface and interface of semiconductors have been of interest to scientists for years and have played an important role in optoelectronics, electronics, sensors, energy conversion, and heterogeneous catalysis. Most of works on the surface and interface of semiconductors have been focused on inorganic semiconductors, since the hetero-junctions between inorganic semiconductors are very important to modern semiconductor devices, as well as to the growth and processing of semiconductors. Recently, the surface and interface involving inorganic semiconductors and organic materials have become attractive due to the fundamental interest and potential application of organic electronics. The semiconductor-organic hybrids have unique surface and interfacial properties and are promising materials for microelectronics, biotechnology and sensor technology.

Table 1.1 Some important inorganic and organic semiconductors

Inorganic Semiconductor	Group IV	Si and Ge
	Group III-V	GaAs, GaP, GaN, AlAs, AlP, InP, InAs,
	Group II-VI	ZnO, ZnS, ZnSe, CdS, CdSe, CdTe, CdS
Organic Semiconductor	aluminum tris(8-hydroxyquinoline) (Alq ₃), pentacene, poly(1,4-phenylene vinylene) (PPV) and derivatives, polythiophene (PT) and derivatives, poly(fluorene) and derivatives	

Some important inorganic semiconductors, and organic semiconductors are listed in Table 1.1. Although most research have been based on single crystal silicon (Si), other semiconductor-organic hybrids have been of increasing interest. Beside Si, gallium arsenide (GaAs), gallium nitrate (GaN), zinc oxide (ZnO), cadmium selenide (CdSe),

as well as organic semiconductors, are also technically important to the semiconductor industry and are strong candidates for fundamental research.

In this thesis, a series of surface and interfacial interactions and reactions involving inorganic and organic semiconductors will be investigated from physical and chemical points of view. The semiconductors studied have included GaAs, ZnO, Si and a photoluminescent conjugated copolymer containing rare earth complexes.

In Chapter 2, the synthesis of semiconductor-organic hybrids and interfacial properties between organic semiconductor and metals were comprehensively reviewed.

In Chapter 3, a semiconductor in Group III-V, GaAs (flat GaAs substrates), was used to prepare GaAs-polymer hybrids. The surface of GaAs was passivated by self-assembly of monolayers of an organic sulfur compound containing hydroxyl group in the end. The hydroxyl groups on the GaAs surface were further functionalized via immobilization of atom transfer radical polymerization (ATRP) initiators. Subsequently, surface-initiated atom transfer radical polymerization of methyl methacrylate (MMA) was conducted from the GaAs surface to prepare the GaAs-PMMA hybrid. The compositions of the GaAs surface, GaAs-PMMA hybrid surface, and GaAs-PMMA hybrid interface were investigated by XPS. The surface morphology was characterized by atom force microscopy (AFM).

Inorganic semiconductor nanoparticles have also attracted many interests due to their size-dependent electrical, optical, and magnetic properties (van, Dijken, 1998; Jun, 2000; Gangopadhyay, 1992). In Chapter 4, a semiconductor in Group II-VI, ZnO (nanoparticles), was used in this study. ZnO-polymer core-shell hybrid nanoparticles, with well-defined polymer shell or polymer brushes of about the same chain length in the shell, were prepared via surface-initiated ATRP of MMA from ATRP initiators immobilized on ZnO nanoparticles. The hybrid nanoparticles were well-dispersed and gave rise to enhanced UV-visible absorption and fluorescence. The chemical composition of the hybrid nanoparticles was investigated by XPS. The morphology and structure of the nanoparticles were determined by field emission scanning electron microscopy (FE-SEM) and transmission electron microscopy (TEM).

The integration of GaAs substrate and ZnO nanoparticles (ZnO quantum dots (QD)) was also attempted in this study. In Chapter 5, a self-assembled monolayer of ZnO colloidal QDs on the 3-mercaptopropyltrimethoxysilane (MPTMS)-passivated GaAs surface was demonstrated. Not only does MPTMS act as a coupling agent for the ZnO QDs, but also passivates the GaAs surface through the formation of covalent As-S and Ga-S bonds. Thus, the present study provides a simple approach to the self-assembly of semiconductor ZnO colloidal QDs on an oriented single crystal GaAs substrate with simultaneous passivation of the latter.

Most of Si-based semiconductor-organic hybrids were developed from the native oxide surface on the silicon substrate, such as the plasma polymerization and

deposition of polymer on the silicon wafer with native oxide layer on the top. In this study, another form of silicon surface viz., the hydrogen-terminated Si(100) (H-Si(100)) surface, was used to develop silicon-based semiconductor-polymer hybrids. In Chapter 6, ultra-thin fluoropolymer films (≤ 2 nm) were deposited directly on the hydrogen-terminated Si(100) (H-Si) and native oxides-covered Si(100) (ox-Si) surfaces by radio-frequency (rf) plasma polymerization of pentafluorostyrene (PFS), and hexafluorobenzene (HFB), 1H,1H,2H-heptadecafluoro-1-decene (HDFD), and perfluoroheptane (PFH). The chemical states at the fluoropolymer/Si interfaces were studied by XPS. In addition, thick fluoropolymer films (150-350 nm) were also deposited on the hydrogen-terminated surfaces by plasma polymerization of PFS, HFB, HDFD, and PFH. The chemical composition and structure of the fluoropolymer films were studied by XPS, time-of-flight secondary mass spectroscopy (ToF-SIMS), and Fourier transform infrared (FTIR) spectroscopy. The hydrophobicity of the fluoropolymer films was studied by water contact angle measurements. The surface topography of the films was also studied by AFM.

Organic semiconductors have attracted considerable interest due to their potential for low-cost and wide applications for semiconductor devices, as well as their compatibility with flexible electronics. The interfacial properties in organic semiconductors also play important roles in the device performance. In Chapter 7, the interface properties between a photoluminescent conjugated copolymer containing rare earth complexes and a metal were investigated. XPS and ultraviolet photoelectron spectroscopy (UPS) are used to study *in situ* the chemical states and electronic properties of the interface formed between aluminium, a widely used cathodic metal in

organic light-emitting diodes (OLEDs) due to its low work function, and the conjugated copolymer containing 9,9'-dihexylfluorene and europium complex-chelated benzoate units in the main chain (PF6-Eu(dbm)₂phen). The copolymer complex is a novel pure red-light emitter. Understanding the interface formation between a low work function electrode, such as aluminium, and PF6-Eu(dbm)₂phen will have direct relevance to the fabrication of high performance polymer light-emitting diodes (PLEDs).

Chapter 2
Literature Survey

2.1 Passivation of GaAs surface

Contrast to the Si-based devices, GaAs is one of the most important compound semiconductors having advantages in radiation resistance and power dissipation (Shur, 1990). However, high density states at surfaces result in pinned Fermi level at GaAs surface. These states lead to various adverse effects, such as high surface recombination velocity, in electronic properties and limit the performances for GaAs-based electronic and optoelectronic devices. Unlike the exceptional favorable properties of the Si/SiO₂ interface in the Si-based semiconductor technique, the chemistry between GaAs and its native oxide do not give rise to a chemically stable and defect free interface (Wieder, 1985). The native oxide formation at the GaAs surface is a common source of the large density of surface states leading to strong Fermi level pinning around the midgap. Moreover, both Ga₂O₃ and As₂O₃ are somewhat soluble in water depending on pH value.

In 1987, Sandroff et al. (Sandroff et al., 1987) reported a passivating scheme for compound semiconductor surfaces via a simple chemical treatment. Very efficient passivation of nonradiative recombination centers was achieved by the deposition of Na₂S · 9H₂O films onto the semiconductor surfaces. It showed that the chemical treatment of GaAs/AlGaAs heterostructure bipolar transistor (HBT) resulted in a significant improvement in the current gain of the device. In the photoluminescence (PL) experiments, a 250-fold increase in PL intensity was observed relative to the untreated GaAs surface at room temperature, indicating a decrease in electron-hole recombination. Because the presence of surface states is known to quench PL, PL

intensity enhancement is widely used to characterize the extent of passivation following treatment. PL enhancement is expected to occur as the result of both band unbending and reduction of surface trap density, and thereby reduction in the rate of surface nonradiative recombination (Chmiel et al., 1990; Kauffman et al., 1992).

Passivations of GaAs surface by sulfur-containing compound have attracted much attention. In addition to $\text{Na}_2\text{S} \cdot 9\text{H}_2\text{O}$, other inorganic ligands employed include $(\text{NH}_4)_2\text{S}$ (Carpenter et al., 1988; Kang et al., 2002), $(\text{NH}_4)_2\text{S}_x$ (Sa et al., 1998; Szuber et al., 2002), and S_2Cl_2 (Li et al., 1994). PL intensity was enhanced by a reduction in the surface recombination velocity. Chemical studies of the sulfur-passivated GaAs surface revealed that the formations of Ga-S and As-S bonds at surface play an important role in the reduction in the surface recombination velocity. Sandroff et al. initially reported a decrease in band bending for Na_2S and $(\text{NH}_4)_2\text{S}$ using Raman Technique, (Sandroff, 1989). However, through many studies using other direct techniques, such as surface conductivity technique and XPS, it became a general agreement that the sulfide-treated GaAs surface do not lead to unpinned Fermi level or increased band bending (Besser et al., 1988; Spindt et al., 1989). XPS studies have shown that only Ga-S bonds remained at the surface, after the annealing of sulfide-treated GaAs surface (at or above 360 °C) (Paget et al., 1996; Arens et al., 1996).

Although the passivation of GaAs surface via inorganic sulfide treatment is simple and effective method, the modified GaAs surfaces remain relatively stable with electronics benefits in air only for several days. XPS investigation showed the

passivating phases decomposed in the presence of oxygen and light, producing a surface composition, primarily of As_2O_3 (Sandroff et al., 1989). The GaAs/ As_xS_y interface evenly degraded, accompanied by the reemergence of a highly density of surface states. Oshima et al. (1993) investigated the initial oxidation features of $(\text{NH}_4)_2\text{S}_x$ -treated GaAs, correlating the PL degradation caused by oxidation with band bending and surface chemical bonding changes. Direct correlation between PL degradation and the Ga oxide formation resulting in dramatic upward band bending was observed.

The above mentioned problem of the GaAs surface has prevented the development of a simple and robust surface passivation scheme for this surface. Green and Spicer (Green et al., 1993) argued that the simple process used to passivate Si is the exception rather than the rule in semiconductor surface passivation, and suggested that a more elaborate scheme may be required for the passivation of GaAs surface with following functions:

- (1) prevent reactions between the atmosphere and GaAs for the lifetime of the device (chemical passivation),
- (2) eliminate and prevent interfacial state formation in the band gap (electronic passivation).
- (3) and possess a sufficient barrier such that electron will not be lost from the GaAs to the passivating layer.

Sheen et al. (1992) discovered of self-assembled monolayers (SAMs) of a class of alkanethiols directly onto the bare GaAs(100) surface for potential applications in molecular electronics. The monolayers of alkanethiols on GaAs(100) surface consisted of a stable, highly organized assembled of tilted, ordered alkyl chains, chemically bonded directly to the GaAs surface via metal-sulfur bonds. Combined with nanotransfer printing technique, SAMs of thiols was successfully used to fabricate molecular devices, Au/1,8-octanedithiol/GaAs junctions (Loo et al., 2003). The electrical transport in the devices occurring through the 1,8-octanedithiol molecules was investigated.

To overcome the poor oxidative of the Na₂S- and (NH₄)S-treated GaAs surface, which lead to rapid degradation of electrical properties, scientists has prompted interest in passivation of GaAs surface by organic sulfides (Adlkofer et al., 2003), especially long-chain thiols (Adlkofer et al., 2001). The hydrophobic alkyl chains are expected to act as a barrier, preventing oxygen and water from reaching and reacting with the GaAs surface. The duration of stability was improved to be a few weeks and months, when GaAs surface was passivated with organic sulfide (Hou et al., 1997; Dorsten et al., 1995).

Lunt et al. (1991) studied a broad range of organic thiols on GaAs surface. Systematically, these organic sulfide treatments resulted in increase in PL intensity. It was also observed that the efficacy of the organic sulfide treatment parallels trends in binding constants of sulfide ligands toward lewis acidic transition metal centers,

which suggest that specific coordination interactions at the surface are important. From time-resolved PL studies at high excitation intensities, organic sulfides were found to retard a substantial surface recombination velocity.

Rao et al. (1989) reported the passivation of GaAs surface by a thin film via plasma-deposition with thiophene. With this technique, uniform and thin films were deposited on GaAs surface using a pure and dry plasma-polymerization. It was found that the surface barrier of GaAs was lowered and the surface recombination velocity was reduced by the deposited polymers film via plasma polymerized of thiophene. It was believed that the covalent bonds between the plasma-deposited polymer film and GaAs surface play an important role.

Recently, Yang et al. (2003) reported an surface passivation of GaAs surface via plasma deposition of an S-containing polymer film from a linear and saturated S-containing monomer, bis(methylthio)methane (BMTH). The chemical states of the interface between the polymer film and GaAs surface were systematically studied by XPS and ToF-SIMS. The investigation showed that the sulfur atoms from the plasma polymerized BMTH film was covalently bonded to both Ga and As atoms of GaAs surface. A two-fold increase in PL intensity of the passivated GaAs surface was observed. Systematic studies the oxidation of the interface in a long term indicated the passivation of GaAs was stable for months under the atmospheric conditions.

2.2 Polymer brushes via surface-initiated polymerization

Modification of inorganic semiconductor surface by an organic film has attracted much attention in recent years. Modification of a surface of solid inorganic semiconductor material with an organic layer, especially a polymer layer, is often used to improve surface and interfacial properties, such as in biocompatibility (Niemeyer, 2001), wetting (Ingall et al., 1999), adhesion (Ejaz et al., 1998), or friction (Weck et al., 1999). Recently, surfaces at a molecular level attracted much interest, since this engineering technology gives rise to well-defined surface with improved surface and interfacial properties. In surface engineering, the generation of specific nanopatterns of chemical groups on a semiconductor substrate offers the ability to direct important interfacial phenomena, such as fluid flow (Kataoka et al., 1999) and adhesion (Fujihira et al., 2001). The nanopatterns may also detect molecular recognition events (Lahiri et al., 1999), carry out signal transduction (Kricka et al., 2001), and direct chemical transformations (Krishnan et al., 2001).

There are generally two strategies to grow an organic film on inorganic semiconductor substrates. One is “graft to” or “top-down” strategy (Bridger et al., 1980), which includes self-assembly of monolayer of organic molecules, spin coating, and absorption of preformed polymer chains on the semiconductor substrate. Another strategy is “graft from” or “bottom-up” (Huang et al., 1999; Buchmeiser et al., 2000; Shah et al., 2000; Jordan et al., 1999; de Boer et al., 2000). It is often performed by surface-initiated polymerization including the modification of inorganic solid surface with covalently bonded initiator groups and subsequent polymerization.

There are some inherent limitations in the “graft to” strategy. (a) It often yields nonuniform thin films and poor surface coverage due to the steric hindrance at the surface. (b) The interaction between the polymer and surface is usually not so strong because it is caused only by van der Waals force or hydrogen bonding. Therefore, desorption can occur upon exposure to a good solvent or the polymer can be replaced by other polymers or species present in the ambient, which compete for absorption sites at the surface.

With the “graft from” strategy, polymer layers are covalently bonded to inorganic semiconductor surface, leading to more stable interfacial and surface properties. This approach is expected to result in considerably higher final grafting densities. The grafting densities are not limited by a steric hindrance imposed by the already bonded chains, since the smaller monomer can readily access the initiator site or the propagating chain end, resulting in a uniform, steady increase in layer film. The molecular weight of the polymer brushes may linearly increase with time, giving rise to a steady growth of a uniform polymer layer on the surface. Block copolymer can be synthesized by reinitiating the polymerization in a different monomer solution. The process is compatible with a wide variety of monomers, such as acrylate, styrenes, acrylonitrile, and their derivatives. Due to their confinement, polymer brushes respond to an environmental stimulus such as solvent quality, ion strength, temperature, pressure, etc., along with a change of the surface properties. The preparation and sample handling in these processes are easy, which allow characterizing surfaces between two subsequent polymerizations. In order to realize the “graft from” strategy,

different living polymerization have been utilized to grow polymer layers onto the semiconductor surface.

To grow the polymer brushes from the surface of inorganic semiconductor substrates, different living polymerization, including radical (de Boer, 2000), cationic (Jordan et al., 1998; Zhao et al., 1999), anionic (Jordan et al., 1999), ring-opening (Husemann et al., 1999), nitroxide-mediated (Mansky et al., 1997; Buchmeiser et al., 2000), and atomic transfer radical polymerizations (Huang et al., 1999; Matyjaszewski et al., 1999; Shah et al., 2000; Ejaz et al., 1998), have been utilized in the research work. In the following, pioneering research works are shown in details.

To modify the surface properties of Si wafer, de Boer et al. (2000) used “living” free radical polymerization to tether a polymer layer on the Si wafer. The polymerization was initiated from a surface-grafted monolayer of an iniferter initiator. The surface properties became hydrophilicity or hydrophobicity depending on the species of monomers used. The linear increase of the thickness of the polymer layer with time was observed. Another representative surface modification is reported by Sidorenko, et al. (1999), they grafted a brushlike polymer coating layer composed of two different polymers, polystyrene and poly(vinylpyridine) on Si(100) crystals by radical polymerization of styrene and vinylpyridine. The yielding polymer coating turned out to be sensitive to the composition and environment.

In 1998, Jordan et al. (1998) reported the first living cationic ring-opening polymerization of 2-ethyl-2-oxazoline initiated from a self-assembled monolayer on a gold substrate. An amphiphilic brush-type layer was formed by functionalizing the polymer chain end with an alkyl moiety by means of termination reaction. The authors proposed application to the broad variety of 2-oxazoline monomers to form corresponding homopolymers, as well as block copolymer and supramolecular structure on solid substrates. Another pioneer work done by Zhao et al. (1999) is that a tether block copolymer of polystyrene-*block*-PMMA was synthesized on a silicate substrate by sequential carbocationic polymerization of styrene followed by atom-transfer radical polymerization of MMA.

Beside the cationic polymerization, Jordan et al. (1999) also used surface-initiated anionic polymerization to grow polymer brush from gold substrate. In this report, a monolayer of biphenyllithium moieties was self-assembled on the gold substrate to initiate the anionic polymerization of styrene. The result suggested that this technique could give rise to a smooth and homogeneous polymer surface throughout the entire substrate on the macroscopic and microscopic scale, indicated by a low index of surface roughness.

In 1999, IBM demonstrated a novel strategy to develop micro-scale patterns in microelectronics (Husemann et al., 1999). In this strategy, patterned polymer brushes were prepared by surface-initiated ring-opening polymerization of caprolactone from the functionalized area of the patterned SAM. This approach formed patterned

polymeric thin films without using expensive photolithography tools, and used SAMs technique in a way that was tolerant to the imperfections within the original monolayer structure.

In addition, they also utilized nitroxide-mediated polymerization to develop nano-scale patterns (Hermann et al., 1996). The work demonstrated a combination of a top-down contact-molding process and a bottom-up surface-initiated grafting strategy to form three-dimensional patterns, in which the chemistry and size of nano-scale patterns could be accurately tuned. The nitroxide-mediated polymerizations could be initiated from the patterned surface to yield the formation of well-defined polymer brushes consisting of polystyrene, MMA, or HEMA.

The nitroxide-mediated polymerization was also used to graft random copolymer brushes from Si wafer to control the polymer-surface interactions (Mansky et al., 1997). In their report, interfacial energies of the polymers at a solid surface can be manipulated by end-grafting statistical random copolymers on the surface, where the chemical composition of a copolymer can be controlled.

The above polymerization approaches have allowed us to modify the surfaces of inorganic substrates by growing polymer layers with a variety of functions, which may give rise to interesting surface and interfacial properties. However, the experimental conditions to carry out these polymerizations are stringent and high temperature is usually needed to facilitate the polymerization. Therefore, these

polymerization approaches may not be used to grow polymer layers from the surface of a compound semiconductor, such as, GaAs, because the atoms on the surface may be easily oxidized and lead to reduced performance in the device.

Recently, a new “living” radical polymerization, atom-transfer radical polymerization (ATRP), was developed and utilized to grow polymer chains on various inorganic solid surfaces, including silicate, carbon, gold, et al., as well as other organic substrates (Pyun et al., 2003). An attractive feature of ATRP is the ability to grow chains from multifunctional cores, or surface simultaneously. ATRP systems could facilely functionalize target substrates using commercially available α -haloesters, or benzyl halides. ATRP initiator groups have been successfully coated onto both organic and inorganic materials, with either flat or curved surfaces. From this approach, polymer brushes of varying compositions and dimensions have been prepared by surface-initiated growth from macroscopic wafers or particles, micro-sized colloids, and polymer backbones. In addition, ATRP may be carried out at room temperature with the careful selection of a polymerization system.

The main challenge in ATRP from flat substrates with very low concentrations of initiating groups stems from the fact that the concentration of persistent radical (deactivator) may be too low to reversibly trap the propagating radicals after halogen atoms transfer to the transition metal catalyst, leading to uncontrolled chain growth. This challenge could be effectively addressed through the addition of a persistent

radical (deactivator), or “sacrificial initiators”, at the beginning of the polymerization (Pyun et al., 2003).

As predicted from the persistent radical effect (Fischer, 2002; Yoshikawa, 2002), the addition of radical-deactivating complexes (Cu(II) halides or Fe(III) halides) at the beginning of the polymerization facilitates exchange reactions between active radicals and dormant halides. The ATRP of styrene and methyl acrylate in the presence of Cu(II) complexes resulted in a progressive increase in the brush film thickness with time (Matyjaszewski et al., 1999). In these polymerizations, only surface-bound alkyl halides were employed as initiators and linear polymers were not formed in the solution. Identical surface-initiated ATRP conducted without the addition of deactivators resulted in the rapid polymerization and termination of tethered polymeric chains, where film thickness did not increase for the prolonged reaction time.

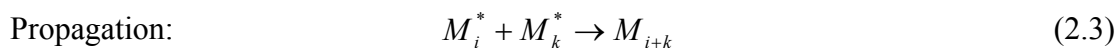
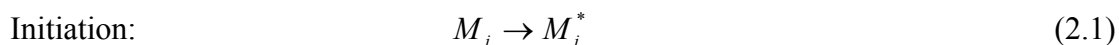
The addition of sacrificial initiators to ATRP mixtures with functional flat substrates serves a number of beneficial purposes in both synthesis and characterization of polymer brushes (Ejaz et al., 1998; Husseman et al., 1999). In system with added free initiator, sufficient concentrations of persistent radical (deactivator) are generated by the termination of radical formed in solution. Furthermore, the final degree of polymerization (DP) of the tethered chains on the surface can be dictated by the concentration of sacrificial initiators added at the initial stages of the polymerization. The determination of both monomer conversion and molar mass of polymers in the

system is also greatly facilitate as the analysis of free polymers formed in the solution can be conducted by standard characterization technique, such as ^1H NMR spectroscopy, SEC, and GPC. It was suggested that the tethered polymer brushes on the surfaces possess similar molar masses and polydispersity to polymers formed from sacrificial initiators.

2.3 Fluoropolymer films deposited by plasma polymerization of fluoro-monomers

Poly(tetrafluoroethylene) (PTFE) and some of its derivatives have exhibited the lowest dielectric constants ranging between 1.9 and 2.1, suggesting promising potential for polymer materials having low dielectric constant for microelectronics. It is well known that fluoropolymers have low dielectric constant due to the small dipole and the low polarizability of the C-F bonds, as well as the large free volume of trifluoromethyl groups. However, it is difficult to allow the deposition of thin layer of PTFE materials due to their insolubility and infusible nature. As successful alternatives, plasma enhanced chemical vapor deposition (PECVD) and plasma polymerization techniques have been used to deposited fluoropolymer films.

The overall mechanisms of plasma polymerization can be represented by eqs. (2.1)-(2.4) (Yasuda et al., 1977):





Where i and k are numbers of repeating units (i.e., $i = k = 1$ for the monomer), and M^* is a reactive species which can be ions of charge, an excited molecules, or a free radical.

To deposit low dielectric constant, high thermal stability films, Han et al. (Han et al, 1998 and 2000) had deposited fluoropolymer films on Cu substrate via plasma polymerization and deposition from aromatic fluoro-monomers, perfluoroallyl benzene and Pentafluorostyrene. Monomer selection was based on the perfluorination and aromatic ring content of the monomers. The fluorination aspect provides low polarizability, thus resulting in low dielectric constants. An aromatic ring was selected to enhance the thermal stability of the resulting fluoropolymer films. In addition, the presence of the carbon-carbon double bonds (C=C) provides a free-radical attack point for facile plasma polymerization. With sequential change in the duty cycle of the pulsed discharge, progressive changes in the composition of the plasma-deposited fluoropolymer films were characterized by XPS and FTIR. In particular, an increased retention of the aromatic ring of the starting monomer in the resulting fluoropolymer films is obtained with decreasing plasma duty cycles during film formation, which could decrease the extent of the decomposition or fragmentation of the fluoro-monomers. Dielectric constant below 2.0 could be obtained in the fluoropolymer films from perfluoroallyl benzene monomers. Following thermal annealing at 350-400 °C under N₂, dramatic improvement in the thermal stability from 300 °C to 420 °C was

observed with only minor increase in the dielectric constants and minor decrease of stability in chemical compositions of the films.

Fluoropolymer films, plasma-polymerized with hexafluorobenzene (HFB) monomer have been also studied (Clark et al., 1982; Munro et al., 1993; Mackie et al., 1998; Yi et al., 2000; Yang et al., 2002). HFB monomer contains double bonds which can be easily dissociated in the plasma and result in a high deposition rate. The fluoropolymer films exhibit a dielectric constant as low as 2.0 and have high transparency in the visible range. XPS studies revealed that the chemical compositions in the fluoropolymer films mainly consist of the neutral carbon, C-CF, CF, CF-CF, CF₂, and CF₃ species. In addition, the fluoropolymer films retained some of the original aromatic structure, as evidenced by the π - π^* shake-up satellite feature in the C 1s core-level spectra. The ToF-SIMS analysis also suggested the aromatic rings were preserved to a large extent during the plasma polymerization process. Besides the aromatic rings, the fluoropolymer films were also composed of some cyclohexadiene and naphthalene, linked by short perfluoroalkene or perfluoroaliphatic chains, or directly bonded to one another.

Zhang et al. (2002) systematically investigated the effects of the carrier gas on the fluoropolymer films plasma-deposited from allypentafluorobenzene monomer. It was found that the surface hydrophobicity of the plasma-deposited films increased the order of O₂ < N₂ < H₂ < Ar, with the good agreement of the fact that the decrease of defluorination effect on the fluoropolymer film was also in the same order. XPS and

ToF-SIMS studies revealed that the fluorinated aromatic ring could be retained to a large extent under proper glow discharge conditions, such low input RF power and the use of non-reactive argon as the carrier gas. It also suggested that the preservation of the fluorinated species in the fluoropolymer films and the substantial increase in surface roughness could lead to an ultra-hydrophobic surface with large water contact angle.

Recently, Fu et al. (2004) reported a novel approach (shown in Figure 2.1) to fabricate nanostructure fluoropolymer composite films that have ultra-low dielectric constant value below 2.0. Initially, a dense uniform poly(tetrafluoroethylene) (PTFE) was deposited on H-Si surface by RF magnetron sputtering of a PTFE target. A nanoporous layer consisting of fluoropolymer nanospheres was then deposited in multiple steps by RF plasma polymerization of allylpentafluorobenzene (APFB) at high RF power. A top PTFE layer was subsequently deposited by sputtering once again to complete the sandwiched structure. The featuring high nanoporous structure was resulted from the agglomeration of the nanospheres in the pp-APFB layer, introducing the air gaps and resulting in ultra-low dielectric constant. The fluoropolymeric nanospheres were also demonstrated by Teare et al. (2002) by plasma polymerization and deposition of a linear fluoro-monomer, perfluorooctyl arylate. It was argued that large RF power creates high concentration of radicals, ions, and other reactive species, and decreases mean free paths of reactive species within the plasma, thus leading to the gas-phase reactions among the reactive species and rapid nucleation. With combination of chemical nature of the resulting fluoropolymer films

(CF_2 and CF_3 are main chemical components), the high surface roughness gave rise to ultra-hydrophobic surfaces. The depositions of ultra-hydrophobic films by plasma polymerization have been also reported for heptafluorobutyl acrylate (Chen et al., 1999), hexafluoroisopropyl acrylate, pentafluoropropyl acrylate, and ethyl heptafluorobutyrate (Coulson et al., 2000).

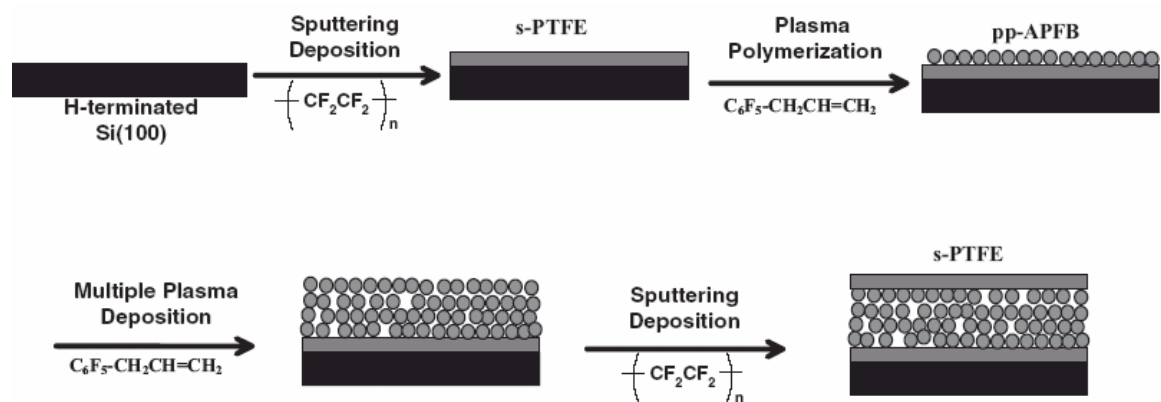


Figure 2.1 Schematic illustration of the process for the preparation of multilayer nanoporous fluoropolymer film (Fu et al., 2004).

2.4 Organic-metal interfaces in organic electroluminescence

In organic electroluminescence devices, both operating voltage and luminescence efficiency of the devices strongly depend on effective charge injection from the electrodes to the organic medium and charge transport in the organic materials (Baldo et al., 2001; Salneck et al., 2001; Hung et al., 2002; Fahlman et al., 2002). To achieve

the lowest possible voltage, it is necessary to have Ohmic interface between the organic layers and the charge-injecting contacts, and to maximize the drift mobility of both types of carriers. Furthermore, charge injection and charge transport also play an important role in optimizing the device efficiency. An unbalanced injection results in an excess of one carrier type that does not contribute to light emission and an enhanced non-radiative recombination because of the interactions of excitons with the charge carriers.

Injection of charge from most electrode materials requires overcoming a barrier at the organic-electrode interface. The nature of the interface is of paramount importance in determining device performance. Photoelectron spectroscopy has been extensively employed to study the electronic structure and chemistry at the organic-metal interfaces. Dipoles, chemical reactions, and atomic diffusion are commonly observed in the near interface region. As a consequence, the determination of the carrier injection barrier is not a simple matter if calculating the difference between the metal work function and the energy levels of the organic solid owing to the presence of interfacial dipole and chemical reactions.

At organic-metal interfaces, the hole and electron barriers (Φ_h and Φ_e) depend on the position the highest occupied molecular orbital (HOMO) and lowest unoccupied molecular orbital (LUMO) of the organic film with respect to the metal Fermi level (E_F). When assuming vacuum level (VL) alignment, Φ_h would be the difference between the ionization potential (IP) of the organic film and metal work function (Φ_M),

and Φ_e would be the difference between Φ_M and the electron affinity (EA) of the organic film. The value of IP and E_F can be separately determined for the metal and organic film by ultraviolet photoelectron spectroscopy (UPS), and value of EA is usually estimated from the value of IP and the HOMO/LUOMO gap obtained from optical measurements (Hung et al., 2002).

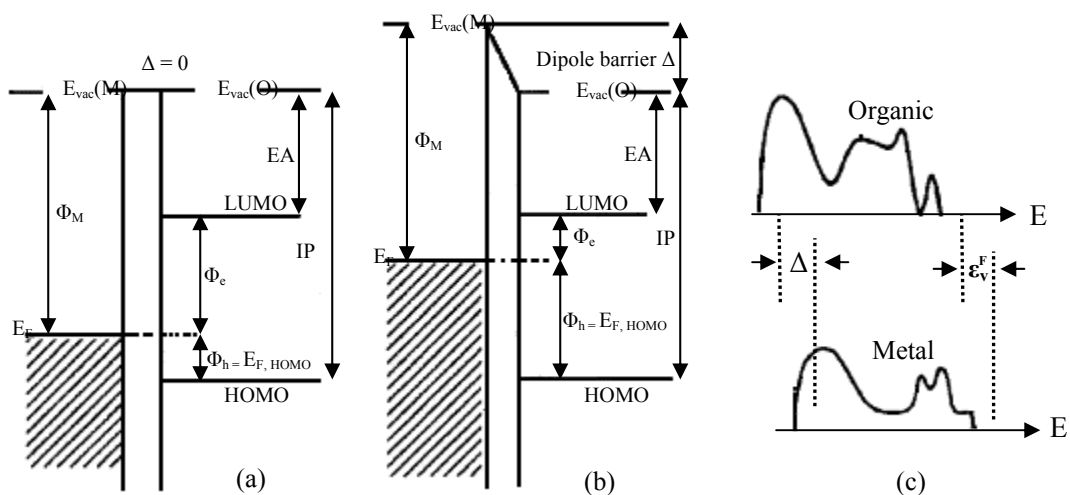


Figure 2.2 Schematic of an organic-metal interface energy diagram (a) without and (b) with an interface dipole and (c) UPS spectra of metal and organic (Ishii et al., 1999; Hung et al., 2002)

For almost all the organic-metal interfaces formed under ultrahigh vacuum conditions, a dipole layer is formed at the organic-metal interface, owing to various origins such as charge transfer across the interface, redistribution of electron cloud, interfacial chemical reaction, and other types of rearrangement of electronic charge (Ishii et al., 1999; Shen et al., 2000). With such interfacial dipole formation, there will be an

abrupt shift of the electrical potential across the dipole layer, giving rise to a shift Δ of the actual VL at the organic-metal interface. The value of Δ is determined by the magnitude of the dipole.

The schematic of an organic-metal energy diagram with and without interface dipole is illustrated in Figure 2.2. The electronic structure shown in figure 2.2(a) corresponds to the alignment of VL across the interface ($\Delta = 0$) and gives $\Phi_h = IP - \Phi_M$ and $\Phi_e = \Phi_M - EA$. In the finite case of Figure 2.2(b), Φ_h and Φ_e are given by $IP - \Phi_M + \Delta$ and $\Phi_M - EA - \Delta$, respectively. This modification of energy level is of critical importance for carrier injection in organic electroluminescence devices. The energy level alignment in Figure 2.2(b) corresponds to a positive charge on the organic side and a negative charge on the metal side at the organic-metal interface.

The interface dipole scenario was originally proposed by Ishii et al. (Ishii et al., 1997 and 1999) and has received extensive support from other research groups (Lee et al., 1998; Shen et al., 2001; Yan et al., 2001; Crispin et al., 2002). The energy level at organic-metal interfaces is determined in ultrahigh vacuum by UPS. The metals of interest are evaporated on silicon, and then the organic-metal interfaces are formed by incremental molecular beam evaporation of organics. Figure 2.2 (c) represents the UPS spectra of the metal and organic. For metals, the right-hand cutoff shows the Fermi edge and left-hand cutoff corresponds to the VL. By depositing increasing amount of organic materials, the emission from the metal becomes suppressed and the spectrum is changed to that of the organic materials. The right-hand cutoff now

corresponds to the HOMO of the organic materials. The shift from the Fermi edge of the metal gives the relative position of the HOMO from the Fermi level of the metal ($E_{F,HOMO}$ in Figure 2.2 (b)). The shift of the left-hand cutoff corresponds to the lowering VL by the deposition of the ultra-thin organic film. Experiments by a number of research groups indicate that dipoles are found at all organic-metal interfaces, while the dependence of the interface dipole magnitude on the metal work function varies from organic to organic (Hill et al., 1998; Hung et al., 2002; Crispin et al., 2002).

The use of a low-work function metal (K, Na, Li, Mg and Ca) cathode is highly desirable for forming an effective electron-injecting contact. However, these metals are poorly suited because of their high chemical reactivity. The study of such an interface between these metals and the organic film Alq₃ revealed strong interactions (Choong et al., 1998; Johansson et al., 1999; Gao et al., 1999). Mason et al. (2001) compiled data generated in different research groups and made a comparison and interpretation. According to the measurement by UPS for five metals (K, Na, Li, Mg and Ca) on Alq₃ under ultrahigh vacuum, the original HOMO level of Alq₃ is shifted to higher binding energy, and a new gap state is formed in the forbidden gap at an energy of ~1.6 eV above the shifted HOMO level. Combined with theoretical calculation, the results indicate the reaction of the metals with Alq₃ to form Alq₃⁻ anions, also resulting in the splitting of the N 1s spectra.

The results indicate that the alkali and alkaline earth metals are too reactive for use in device fabrication. From the standpoint of commercial device fabrication, there would be significant advantage to utilize a pure Al cathode. In addition, UPS studies of Alq₃ deposited on Al show a very small barrier to electron injection. However, Al makes a fairly poor cathode in Alq₃-based devices when compared to the commonly used MgAg cathode. In an effort to understand the relatively poor electron injection in Al/tris-(8-hydroxyquinoline) aluminum (Alq₃)-based devices, Le et al. (2000) have studied the interface formation produced from Al deposition onto Alq₃. All core levels of oxygen, nitrogen and carbon in XPS analysis showed significant broadening and shifting to higher binding energy with increasing aluminum deposition. A detailed analysis suggested that aluminum reacts preferentially with the quinolate oxygen, and then with nitrogen. The experimental results are consistent with their quantum chemical calculation using density-functional theory (DFT). In UPS analysis, deposition of an aluminum layer as thin as 0.02 nm induced a significant change in the valence spectrum of Alq₃ and formed new states, which extended into the energy gap. The features of the Alq₃ structure have virtually vanished after deposition of 0.07 nm aluminum. Both the XPS and UPS are consistent with a destructive reaction between Al and Alq₃, which is expected to cause poor device performance.

Deep Al penetration into Alq₃ has also been revealed by Rutherford backscattering (RBS) measurements on a sample consisting of a graphite substrate, an Al intermediate layer (3 nm), and an Alq₃ surface layer (35 nm) (Huang et al., 1998). RBS profiling revealed Al atoms in the surface region with an amount of $\sim 1.6 \times 10^{15}$

per cm^2 (or ~ 0.25 nm). Photoluminescence measurements indicated that the Al penetration had a strong correlation with Alq_3 photoluminescence quenching.

For the aluminum on poly(p-phenylene vinylene) (PPV) interface (Salaneck et al., 1996), XPS studies revealed that the aluminum forms covalent bonds primarily with the vinyl groups, disrupting the conjugation and making the polymer insulating. Since the aluminum atoms diffuse roughly 3 nm into the film, the 'real' interface is a 3 nm insulating aluminum-PPV layer sandwiched between the metallic aluminum and the conducting polymer film, which explains the poor electron injection. In order to improve electron injection, different cathode materials were used. Photoelectron spectroscopy combined with quantum chemical theory provided some of the guidelines. Low work function metals such as alkali metals should reduce the barrier for electron injection and hence improve device performance. Unfortunately, photoelectron spectroscopy studies on PPV showed that alkali metals such as sodium and rubidium dope the polymer and diffuse into the bulk of the film, causing the formation of polarons or bipolarons (Fahlman et al., 1993; Iucci et al., 1995). It was surprising that Ca-based devices showed improvement in device efficiency as compared to Al-based devices (Braun et al., 1991), because XPS studies of in-situ deposited calcium on a PPV-derivative resulted in doping of the polymer film, which is similar to that for alkali metals (Salaneck et al., 1996), should not give rise to good device performance. However, the interfacial chemistry is highly dependent on the presence of water or oxygen. When calcium was deposited onto oxidized PPV surfaces, a thin metal-oxide layer would be formed between the metallic Ca and PPV

surface and prevented the diffusion of Ca into the film and doped the polymer chains, leading to a Schottky-barrier type contact at the PPV-Ca interface (Ettedgui et al., 1996).

Chapter 3

GaAs-Polymer Hybrids via Surface-Initiated

Atom Transfer Radical Polymerization of Methyl Methacrylate

3.1 Introduction

Semiconductor-polymer hybrids prepared by incorporating polymer brushes on semiconductor substrates have attracted considerable attention in recent years. The hybrids have unique surface and interface properties (Mansky et al., 1997; Ejaz, et al., 1998; Huseman et al., 1999; Zhao et. al., 1999), and allow the fabrication of nanopatterns (Husemann, et al., 2000). Popular strategies for incorporating polymer brushes on substrates include (i) the “top-down” or “grafting-to” approach, in which macromolecules are tethered directly onto the surface of a substrate, and (ii) the “bottom-up” or “grafting-from” approach that attempts to grow polymer brushes from initiators anchored on a substrate surface. The latter approach can result in more densely packed polymer brushes. Ionic (anionic (Jordan et al., 1999), and cationic (Zhao et al., 1999)), ring-opening (Husemann et al., 2000), radical (de Boer et al., 2000), nitroxide-mediated radical (Mansky et al., 1997), and atom transfer radical (Ejaz et al., 1998; Huang et al., 1999) polymerizations have been used for surface graft polymerizations. Among these techniques, atom transfer radical polymerization (ATRP) allows the preparation of well-defined polymers and polymer architecture, and exhibits good tolerance for functional groups and impurities (Zhao et al., 1999).

Semiconductor-polymer hybrids prepared via surface-initiated polymerization on silicon substrates, carbon nanotube, and germanium nanoparticles have been reported. GaAs-polymer hybrids with well-ordered polymer brushes have potential applications in advanced GaAs-based semiconductor devices (Sze, 1981), chemical sensors (Seker et al., 2000), and biomaterials (Sackmann et al. and Tanaka et al., 2000). Recent

developments in the preparation of Au-polymer hybrids via surface-initiated ATRP and GaAs-organic hybrids from self-assembly of monolayers (SAMs) of alkane thiol on GaAs (Sheen et al., 1992) have inspired us to synthesize GaAs-polymer hybrids via ATRP. It is also hope that a dense, well-defined and covalently bonded polymer nanofilm will also help to stabilize the surface states associated with this compound semiconductor.

In this chapter, the surface of GaAs was passivated by self-assembly of monolayers of organic sulfur containing hydroxyl groups. The hydroxyl groups on the GaAs surface were further functionalized via immobilization of ATRP initiators. Subsequently, surface-initiated atom transfer radical polymerization of methyl methacrylate (MMA) was conducted from the GaAs surface to prepare GaAs-PMMA hybrid. The surface compositions of GaAs surface, GaAs-PMMA hybrid surface, and GaAs-PMMA hybrid interface were analyzed by X-ray photoelectron spectroscopy (XPS). The surface morphology was characterized by atom force microscopy (AFM).

3.2 Experimental

Materials. (100)-oriented GaAs single-crystal wafer, having a thickness of about 500 μm and a diameter of about 50 mm, were obtained from Wafer World Inc., Ft. Lauderdale, FL. The as-received wafers were polished on one side and doped with Si to a resistivity level of 0.09-0.026 $\text{ohm}\cdot\text{cm}$. The GaAs were sliced into strips of 3 cm \times 1 cm in area.

All the organic chemical reagents were obtained from Aldrich Chemical Co. of Milwaukee, WI. Methyl methacrylate (MMA) was distilled under reduced pressure and stored in an argon atmosphere at $-10\text{ }^{\circ}\text{C}$. Copper(I) bromide (CuBr) was stirred in glacial acid for 5 h, filtered, and washed with ethanol under argon atmosphere. The treated CuBr was dried under vacuum at 60°C overnight. Tetrahydrofuran (THF, Aldrich, 99%) was distilled after drying with sodium. Triethylamine was distilled after drying with calcium hydride.

Tris(2-(dimethylamino)ethyl)amine (Me_6tren) was prepared according to the method described in the literature (Queffelec et al., 2000). A mixture of formaldehyde and formic acid was stirred at 0°C for one hour. A solution of tris-(2-aminiethyl)amine and deionized water was added dropwise. The mixture was gently refluxed overnight at 100°C . After cooling down to room temperature, the volatile fractions were removed by rotary evaporation. The brown residue was treated with 10% sodium hydroxide. An oily layer formed was extracted into methylene chloride. The methylene chloride

extract was dried over potassium hydroxide overnight and evaporated to produce yellow oil (Me₆tren).

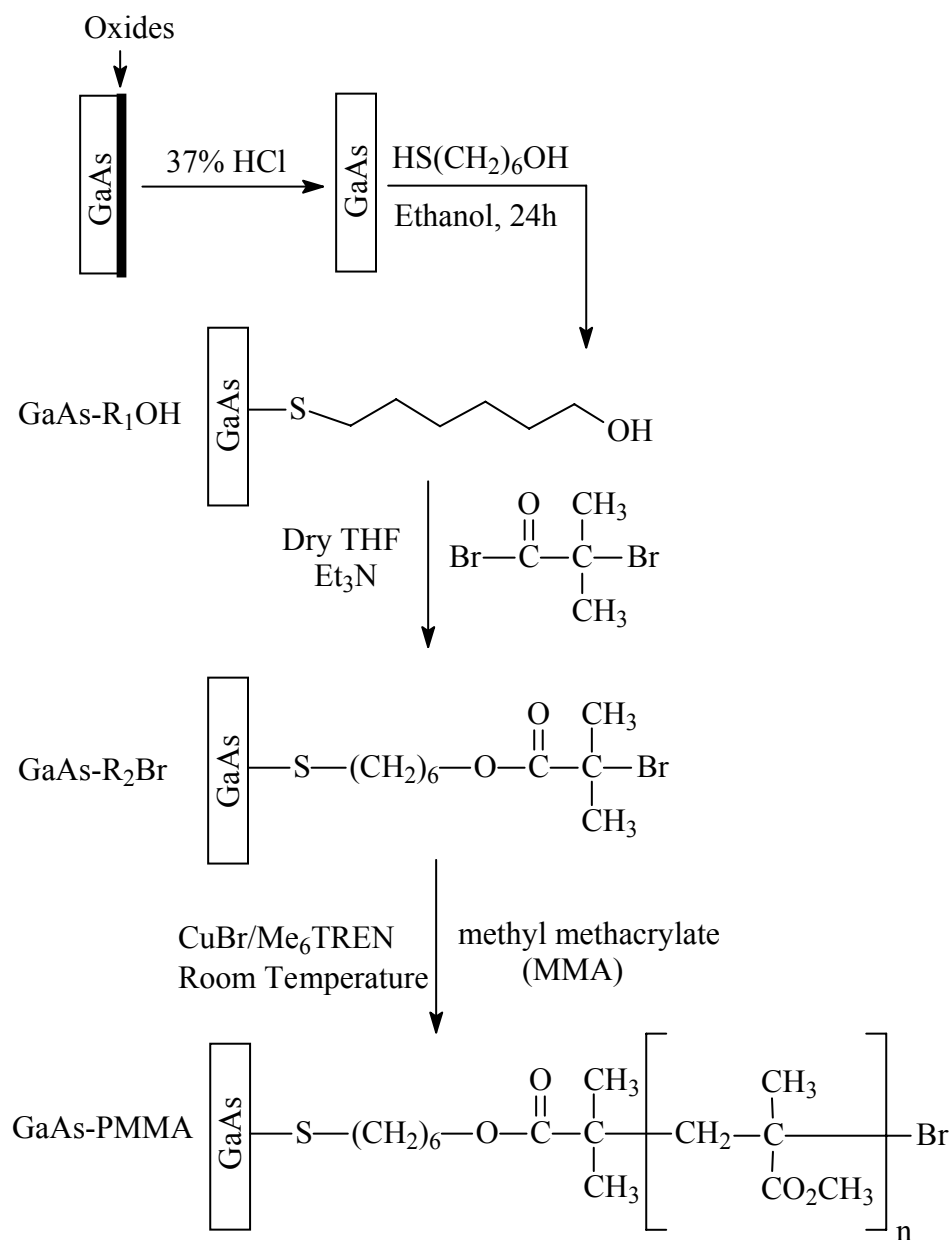


Figure 3.1 Schematic illustration of surface passivation, covalent immobilization of ATRP initiators on the GaAs surface, and surface-initiate ATRP to form the GaAs-PMMA hybrids.

The processes for fabricating GaAs-polymer hybrids with well-defined and covalently tethered polymer brushes, include passivation of GaAs surface with thiol, immobilization of initiators, and consequent surface-initiated atom transfer radical polymerization (ATRP) of methyl methacrylate (MMA) as shown in Scheme 3.1.

Passivation of GaAs(100) surface with self-assembled monolayers of 6-mercapto-1-hexanol. To remove the organic residues from the surface, the GaAs substrate was sonicated in acetone for 10 min, rinsed with ethanol, and then blow-dried with argon. The GaAs substrate was subsequently immersed into concentrated HCl (37 vol %) for two min to remove the native oxide layer on the surface (Adlkofer, 2001). To deposit the self-assembled monolayers (SAMs) of 6-mercapto-1-hexanol on the GaAs surface, the fresh HCl-etched GaAs substrate was immersed into 5 mM ethanol solution of 6-mercapto-1-hexanol, which had been subjected to 3 freeze-pump-thaw cycles to remove the dissolved oxygen, for 24 h at room temperature under an argon atmosphere. The resulting surface with terminated hydroxyl groups was referred to GaAs-R₁OH surface.

Immobilization of the ATRP initiators on GaAs(100) surface. To achieve near-quantitative initiator immobilization, the resulting GaAs-R₁OH substrate was immersed into 0.1 M THF solution of 2-bromoisobutyryl bromide, containing 0.1 M triethylamine, for 2 min under argon. Since 2-bromoisobutyryl bromide are moisture sensitive and a thiol SAMs could be unstable on the GaAs(100) surface in the presence of hydrobromic acid (HBr), the GaAs-R₁OH substrate was immersed into the

reaction medium in the presence of an organic base (triethylamine) for only 2 min. After the reaction, the so-modified substrate was rinse with ethanol. The resulting surface was referred to GaAs-R₂Br surface.

Surface-initiated ATRP of MMA. For the preparation of poly(methyl methacrylate) (PMMA) brushes on the GaAs-R₂Br surface, CuBr (14.3 mg, 0.1 mmol) and CuBr₂ (2.2 mg, 0.01 mmol) were added to 5.3 ml of MMA. The solution was subsequently subjected to three freeze-pump-thaw cycles to remove the dissolved oxygen. GaAs-R₂Br substrate and Me₆tren (26 μ l, 0.11 mmol) were then added to the solution. The reaction flask was sealed under an argon atmosphere for a predetermined period time. After the reaction, the GaAs substrate with surface-grafted MMA polymer (PMMA) (the GaAs-PMMA hybrid) was washed/extracted continuously for 8 h with an excess volume of THF (a good solvent for PMMA), to remove the physically adsorbed PMMA and other reactant residues.

Materials and Surface Characterization. The chemical composition of the GaAs surface and GaAs-PMMA hybrids interface was determined by X-ray photoelectron spectroscopy (XPS). To prepare the HCl-etched GaAs samples for XPS measurement, the fresh HCl-etched GaAs sample was cleaned and transferred into XPS chamber under nitrogen. The XPS measurements were performed on a Kratos AXIS HSi spectrometer using a monochromatic Al K α X-ray source (1486.6 eV photons) at a constant dwell time of 100 ms and a pass energy of 40 eV. The samples were mounted on the standard sample studs by means of double-sided adhesive tapes. The core-level

signals were obtained at a photoelectron take-off angle (α , measured with respect to the sample surface) of 90° . The X-ray source was run at a reduced power of 150 W (15 kV with an emission current of 10 mA) to minimize possible damage to the organic films. The pressure in the analysis chamber was maintained at 10^{-9} Torr or lower during each measurement. All binding energies (BE's) were referenced to the C 1s hydrocarbon peak at 284.6 eV. Surface elemental stoichiometries were determined from the spectral area ratios, after correcting with the experimentally determined sensitivity factors, and were reliable to within $\pm 10\%$. The elemental sensitivity factors were calibrated using stable binary compounds of well-established stoichiometries.

The topography of the HCl-etched and graft-polymerized GaAs surfaces was studied by atomic force microscopy (AFM), using a Nanoscope IIIa AFM from the Digital Instrument Inc. In each case, an area of $1 \times 1 \mu\text{m}$ square was scanned using the tapping mode. The drive frequency was 330 ± 50 kHz, and the voltage was between 3 and 4.0 V. The drive amplitude was about 300 mV, and the scan rate was 0.5 - 1.0 Hz. An arithmetic mean of the surface roughness (R_a) was calculated from the roughness profile determined by AFM.

Gel permeation chromatography (GPC) measurements were carried out using an HP 1100 HPLC equipped with a PLgel $5 \mu\text{m}$ MIXED-C column and a HP 1047A refractive index detector. THF was used as the mobile phase for PMMA.

The thickness of the polymer films grafted on the GaAs substrates was determined by ellipsometry. The measurements were carried out on a variable angle spectroscopic ellipsometer (model VASE, J. A. Woollam Inc., Lincoln, NE) at incident angles of 70° and 75° in the wavelength range 250-1000 nm. The refractive index of the dried films at all wavelengths was assumed to be 1.5. All measurements were conducted in the dry air at room temperature. For each sample, thickness measurements were made on at least three different surface locations.

Static water contact angles of the PMMA films grafted on the GaAs surfaces were measured by the sessile drop method at 25°C and 65% relative humidity using a contact angle goniometer (Model 100-00-(230)), manufactured by Rame-Hart, Inc., Mountain Lake, NJ, USA. The telescope with a magnification power of 23× was equipped with a protractor of 1° graduation. For each contact angle report, five readings from different parts of the PMMA film surface were averaged.

3.3 Results and Discussion.

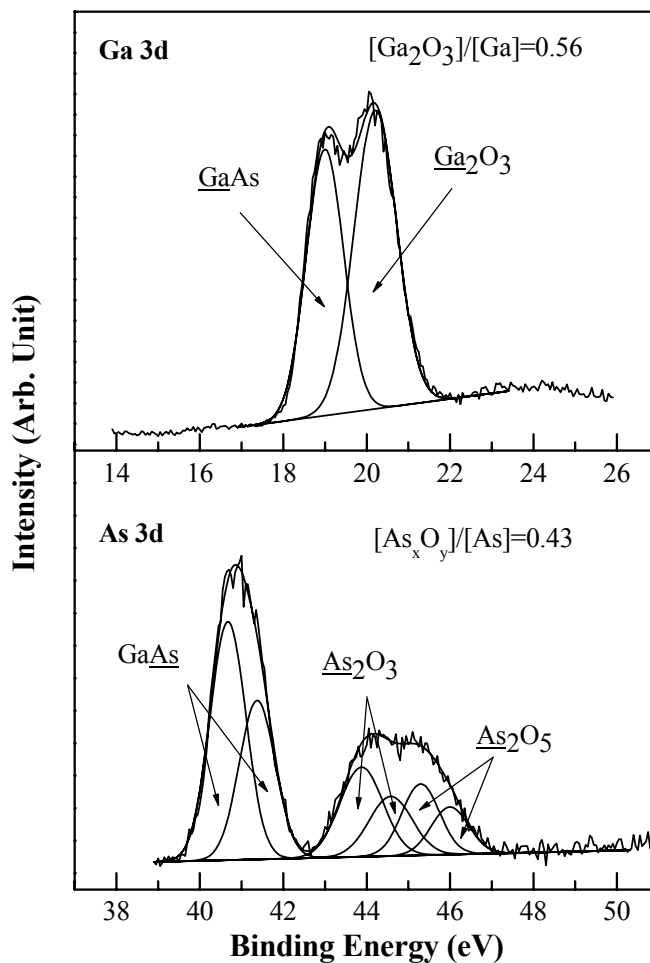


Figure 3.2 XPS Ga 3d and As 3d core-level spectra of the pristine GaAs(100) surface.

The pristine (as-received) GaAs(100) substrate surface is usually covered with an native oxide layer. Figure 3.2 show the Ga 3d and As 3d core-level spectra of pristine GaAs(100) surface. The Ga 3d core-level spectrum of pristine GaAs(100) surface consists of two peak components, having binding energies (BEs) at about 19.0 eV for the GaAs species and at about 20.4 eV for the Ga₂O₃ species (Sandroff et al., 1989). The As 3d core-level spectrum of the pristine GaAs(100) surface shows three spin-

orbit-doublets, having BEs at about 40.7 eV ($3d_{5/2}$) and 41.4 eV ($3d_{3/2}$) for the GaAs species, at about 44.0 eV and 44.7 eV ($3d_{3/2}$) for the As_2O_3 species, and at about 45.3 eV ($3d_{5/2}$) and 46.0 eV ($3d_{3/2}$) for the As_2O_5 species (Lunt et al., 1991 and Moulder et al., 1992). The concentration of the Ga oxide species on the GaAs surface is defined as the $[Ga_2O_3]/[Ga]$ ratio and is derived from the ratio of the sum of the Ga_2O_3 spectral component area to the Ga 3d spectral area. Similarly, the concentration of the As oxide species, including the As_2O_3 and As_2O_5 species, is defined as the $[As_xO_y]/[As]$. The Ga oxides and As oxides with concentrations as high as 0.56 and 0.43, respectively, is attributable to the native oxides on the pristine GaAs(100) surface. The XPS results indicate that the native oxide layer on the pristine GaAs(100) surface mainly consists of Ga_2O_3 , As_2O_3 , and As_2O_5 . However, the native oxides on GaAs is not chemical stable. Both Ga oxides and As oxides on the surface are somewhat soluble in water, and their solubilities are dependent on pH. In addition, the oxide layers on the GaAs surface led to a large density of extrinsic surface states, which result in Fermi level pinning around midgap and high electron-hole recombination velocity to reduce the GaAs-based device performance.

To remove the native oxide layers on the GaAs surface, various wet chemical etching processes had been applied to the GaAs surface (Seker et al., 2000). In this work, concentrated HCl (37%) was used to etch the native oxide layer, because this etch process is simple and may lead to a nearly stoichiometrically pure GaAs surface. The compositions of GaAs surfaces after each chemical treatment were characterized (XPS). Figure 3.3 shows the Ga 3d and As 3d core-level spectra of the GaAs surface

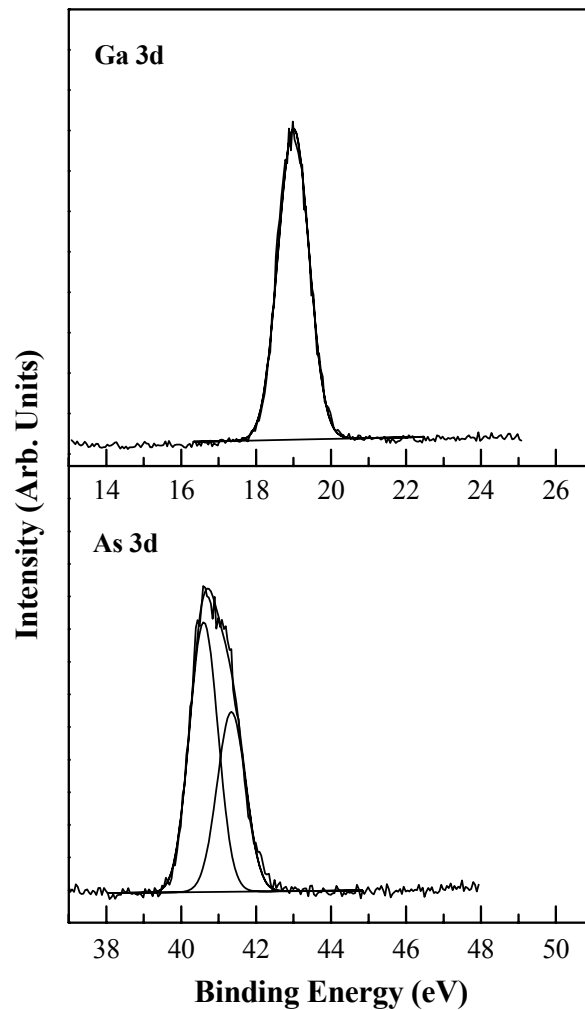


Figure 3.3 XPS Ga 3d and As 3d core-level spectra the HCl-etched GaAs(100) surface.

after concentrated HCl (37%) etching. The Ga 3d core-level spectra had a peak component at the binding energy of about 19 eV, which is associated with the GaAs species. The As 3d core-level spectrum consisted of a spin-orbit-split doublet, with binding energy at about 40.7 eV for As 3d_{5/2} component and 41.4 eV for As 3d_{3/2} component, which are attributable to the GaAs species. The As and Ga oxide species were absent in both spectra. The quantitative analysis by XPS reveals that the atomic

concentration ratio of [As]/[Ga] is about 1.05: 1. The XPS results indicate that the As oxides and Ga oxides have been completely removed by the treatment of concentrated HCl and suggest the reactive sites (dangling bonds associated with Ga and As on the GaAs(100) surface) have been created on the GaAs surface. The dangling bonds on the GaAs surface have the cation and anion dangling bond states, which might be associated with the Fermi level pinning on the GaAs semiconductor (Sankey et al., 1985).

Since the report (Sandroff et al., 1987) that a simple nonhydrate sodium sulfide ($\text{Na}_2\text{S}\cdot 9\text{H}_2\text{O}$) treatment of GaAs(100) surfaces led to a large increase in photoluminescence, indicating a decrease in indirect electron-hole recombination, there have been many reports on the sulfur passivation of GaAs surface. So far, there are mainly three sulfur passivation methods, via inorganic sulfur treatment, passivation by plasma deposition of s-containing polymer on GaAs surfaces (Rao et al, 1989; Yang et al., 2003), and self-assembled monolayers (SAMs) of thiol on GaAs surfaces (Sheen et al., 1992). It has been shown that the formation of As_2S_3 and Ga_2S_3 is the key factor in reducing the surface electron-hole recombination velocity (Sandroff et al., 1989). Among these methods, SAMs of thiol on GaAs surface lead to efficient passivation of GaAs surfaces and well-defined structure of organic monolayers on the GaAs surfaces. In the present work, 6-mercapto-1-hexanol containing HS and OH groups at both ends was used to passivate the GaAs(100) surface. After passivation, the OH group on the passivated GaAs surface could be further functionalization.

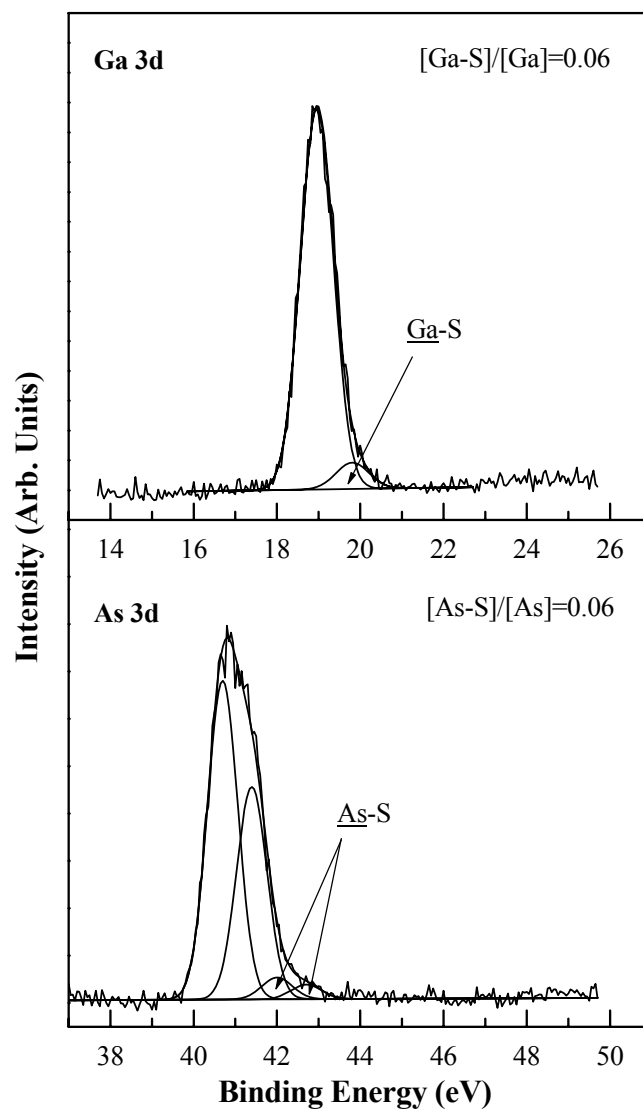


Figure 3.4 XPS Ga 3d and As 3d core-level spectra of the GaAs-R₁OH surface.

Figure 3.4 shows the Ga 3d and As 3d core-level spectra of the GaAs-R₁OH surface, which was created by immersing the HCl-etching GaAs substrate in a 5mM ethanol solution of 6-mercapto-1-hexanol for 24 h at room temperature. It was found that a new spin-orbit-split doublet at the BEs of about 42.0 eV (3d_{5/2}) and 42.7 eV (3d_{3/2}), attributable to the As-S species, and a new peak component at the binding energy of

about 19.7 eV, attributable to the Ga-S species, appeared in the As 3d and Ga 3d core-level spectra of the GaAs-R₁OH surface. The relative concentrations of the Ga sulfide species and As sulfide species, [Ga-S]/[Ga] and [As-S]/[As], have about the same value of 0.06. In addition, Figure 3.5 shows the curve-fitted spectrum in the BE region of S 2p. The peak components at the BE's of about 159.6 eV and 156.6 eV can be attributed to the Ga 3s core-level spectrum for the GaAs species and As plasmon loss, respectively. The spin-orbit splitting doublets in S 2p core-level spectrum, having BE's at about 162.0 eV (2p_{3/2}) and 163.2 eV (2p_{1/2}), can be assigned to the sulfide species at the interface (Moulder et al., 1992). These XPS results suggest that self-assembled monolayers of 6-mercapto-1-hexanol have been deposited on freshly HCl-etched GaAs surface via covalent As-S and Ga-S bonds.

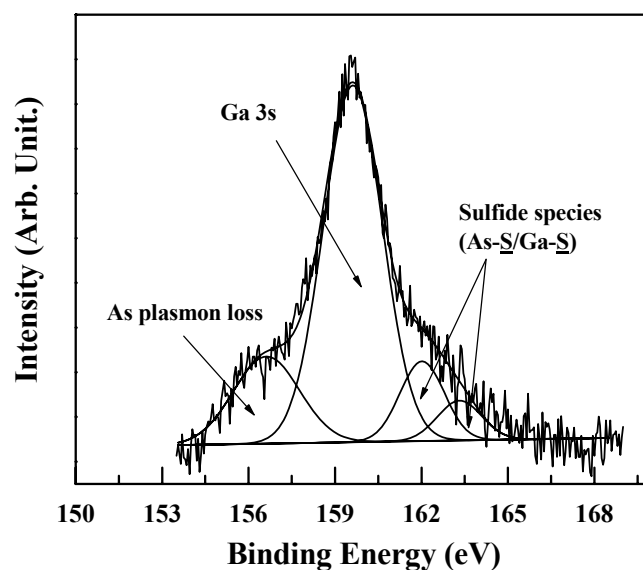


Fig. 3.5 XPS core-level spectra of the GaAs-R₁OH surface in the region of S 2p.

The immobilization of ATRP initiators was conducted by treating the GaAs-R₁OH substrate with a solution of 2-bromoisobutryl bromide in the presence of triethylamine. The role of the initiator in the metal-catalyzed surface-initiated ATRP is to form an initiating radical species via homolytic cleavage of its labile bonds, such as C-halogen by the metal catalysts. In most cases, the dissociated halogen or its equivalent is subsequently reattached to the propagating radical chain end to give a dormant species.

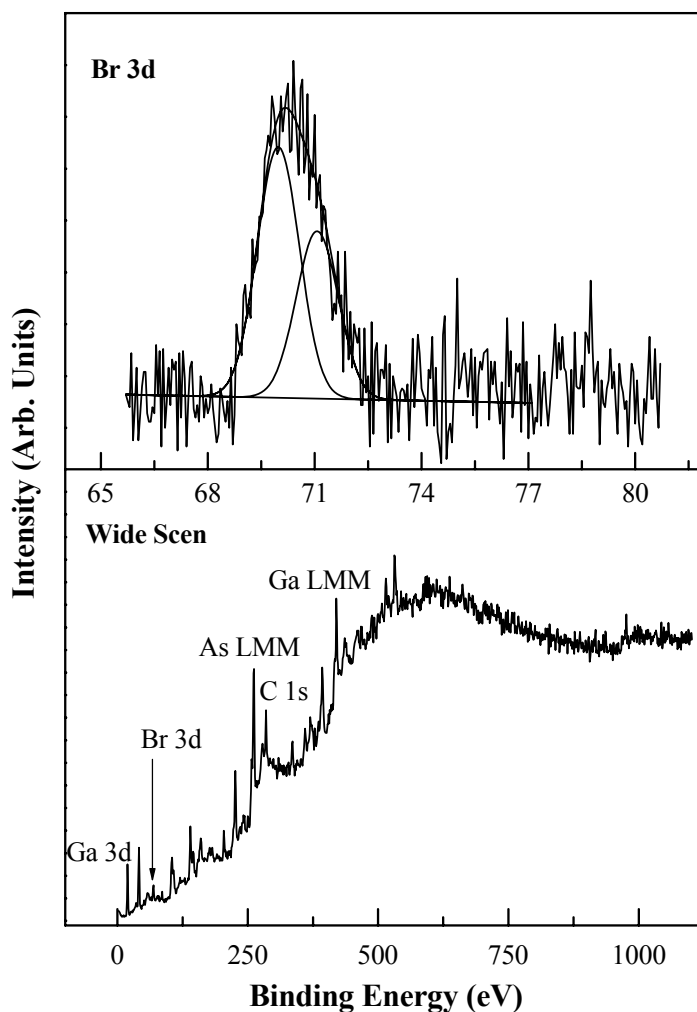


Figure 3.6 XPS Br 3d core-level and wide scan spectra of GaAs-R₂Br surface.

A variety of initiators, typical alkyl halides, haloalkanes, haloketones, haloamides, halonitriles, sulfonyl halides, and haloesters, have been used successfully in ATRP. Among these initiators, haloesters can be versatile for various monomers, including styrenes, methacrylates, acrylates, etc. by careful design of the structures (Kamigaito et al., 2001; Matyjaszewski et al., 2001).

Figure 3.6 shows the wide scan and Br 3d core-level spectra of the GaAs-R₂Br surface. The successful immobilization of the bromoester initiators on the GaAs surface is verified by the appearance of a Br 3d spin-orbit splitting doublet at the BE's of about 70 eV (3d_{5/2}) and 71 eV (3d_{3/2}) (Moulder et al., 1992). The BE assignments for the various elemental species and chemical states are provided in Table 3.1. The resulting GaAs-R₂Br substrate has a uniform film thickness of about 0.7 nm, as measured by ellipsometry at five different locations on the surface of a 3 cm² GaAs substrate. The surface roughness (R_a) of the GaAs-R₂Br substrate, as determined from the atomic force microscopy (AFM) image, remain practically unchanged from that of HCl-etched GaAs surface (Table 3.2). The density of the coupling agent-initiator species was estimated from the linear contribution of that of ethyl-2-bromo-2-methylpropionate (1.33 g/ml) and that of 1-butanethiol (0.84 g/ml). Thus, from the density (~1.1 g/ml) and the molecular weight (282 g/mol) of the coupling agent-initiator species, the surface graft density of the coupling agent-initiator is estimated to be about 1.6 units/nm², which is comparable to that of the SAMs of alkane thiol on GaAs surfaces reported previously (Sheen et al., 1992).

Table 3.1 XPS analysis of the As 3d, Ga 3d, S 2s, and C 1s core-level spectra.*

	Binding Rnergy (eV)	Assignment	FWHM (eV)
As 3d	40.7 (3d _{5/2}), 41.4 (3d _{3/2})	<u>GaAs</u>	0.86
	42.0 (3d _{5/2}), 42.7 (3d _{3/2})	<u>As-S</u>	0.86
	44.0 (3d _{5/2}), 44.7 (3d _{3/2})	<u>As₂O₃</u>	1.12
	45.3 (3d _{5/2}), 46.0 (3d _{3/2})	<u>As₂O₅</u>	1.03
Ga 3d	19	<u>GaAs</u>	0.93
	19.7	<u>Ga-S</u>	0.93
	20.4	<u>Ga₂O₃</u>	1.02
S 2p	162(2p _{3/2}), 163.2(2p _{1/2})	Sulfide	1.31
C 1s	284.6	<u>C-H</u>	1.29
	285.3	<u>C-COO</u>	1.29
	286.4	<u>C-O</u>	1.29
	288.6	<u>O=C-O</u>	1.00

The assignments were made with reference to Refs. (Moulder, 1992; Sandroff, 1989; Lunt, 1991; and Beamson, 1992).

Table 3.2 Thickness and surface roughness of the PMMA films grafted on the GaAs(100) substrates.^a

Sample	Reaction Time (h)	Thickness ^b (nm)	DP ^c	Surface Roughness ^d R _a (nm)
HCl-etched GaAs	—	—	—	0.56
GaAs-R ₂ Br	—	0.7	—	0.52
GaAs-PMMA1	4	9	120	0.43
GaAs-PMMA2	8	20	270	0.58
GaAs-PMMA3	12	24	320	0.53
GaAs-PMMA4	21	29	390	0.63

^a Reaction conditions for fabricating GaAs-PMMA hybrids:

[MMA]:[CuBr]:[Cu(Br)₂]:[Me₆TREN] = 500:1:0.1:1.1, room temperature and under an argon atmosphere.

^b The film thickness was measured by ellipsometry.

^c Average degree of polymerization (DP) was estimated based on the surface initiator density of about 1.6 units/nm², PMMA density of 1.1 g/cm³, MMA molecular weight of 100 g/mol, and the corresponding PMMA film thickness.

^d R_a was the arithmetic mean of surface roughness calculated from the roughness profile of the AFM image.

Surface-initiated ATRP of MMA from the GaAs-R₂Br surface was conducted in a continuously stirred MMA, containing CuBr, CuBr₂ and Me₆tren. The resulting GaAs-PMMA hybrid with a PMMA film thickness of about 29 nm, as measured by ellipsometry, has a water contact angle of about 69° (GaAs-PMMA4, Table 3.2). The contact angle is comparable to that of the PMMA homopolymer (~ 71°) (Eaton et al., 2000). As shown in the Table 3.2, the thickness of the grafted PMMA film in the resulting GaAs-PMMA hybrids increases with the increase in polymerization time, suggesting that the growth of the PMMA chains is consistent with a controlled process. The result was further supported by an approximately linear increase in the average degree of polymerization (DP) of PMMA homopolymer with the MMA monomer conversion (Figure 3.6) for concurrent polymerizations with the free initiator (ethyl-2-bromo-2-methylpropionate) in solution. Since the average cross-sectional area of PMMA chain prepared by surface-initiated ATRP is 1.8 – 2.0 nm² (Shah, 2000 and Kim, 2000) and the surface initiator density is about 1.6 unit/nm², the surface initiator efficiency of the present system is estimated to be about 30%. Together with a PMMA thickness of 29 nm (Sample GaAs-PMMA4, Table 1), PMMA density of 1.1 g/cm³ (Shah, 2000), and MMA molecular weight of 100 g/mol, the average DP of PMMA graft chain is estimated to be about 390. This value is also comparable to those obtained from homopolymerizations in solution (Figure 3.7).

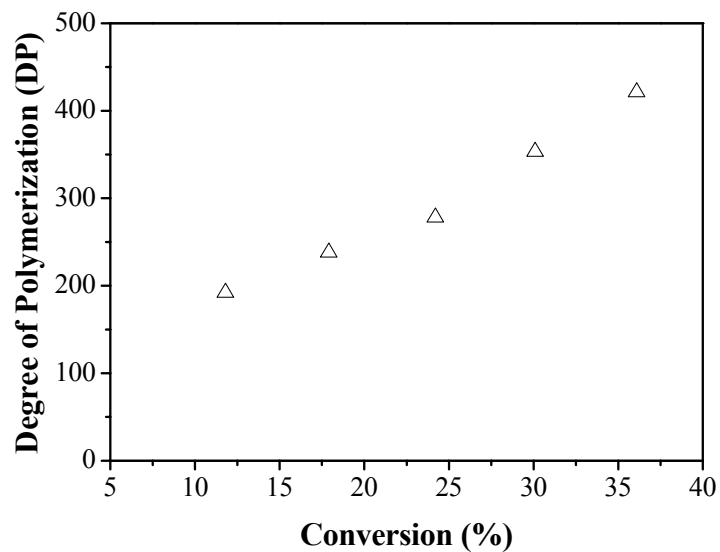


Figure 3.7 The relationship between the average degree of polymerization (DP) and the conversion of MMA monomer. Reaction condition: [MMA]:[CuBr]:[Cu(Br)₂]:[Me₆tren]:[ethyl-2-bromo-2-methylpropionate] = 500:1:0.1:1.1:1, room temperature and under an argon atmosphere.

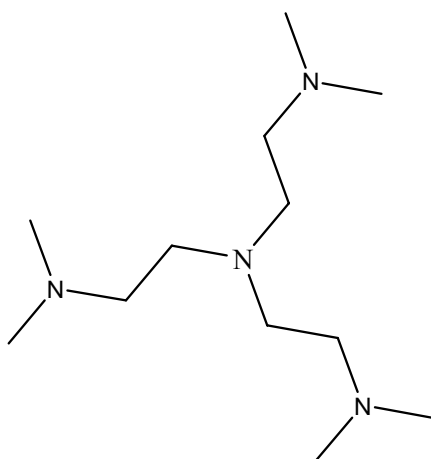


Figure 3.8 Structure of tris(2-(dimethylamino)ethyl)amine (Me₆tren).

The Cu/Me₆tren catalyst system was used for the surface-initiated ATRP process. In ATRP, the catalyst reactivity can be adjusted by changing the ligand, counterion, or transition metal. Of all the transition metals investigated, copper appears to be most promising in terms of price, reactivity, and versatility. The counterions used for ATRP can be acetates (Matyjaszewski et al., 1998), hexafluorophosphate (Davis et al., 1999), triflate (Woodworth et al., 1998), atomic oxygen (Percec et al., 1998), or halogen. Among the catalyst systems for ATRP, copper halides are among the most frequently utilized. To fine-tune the catalyst system based on copper halides, a variety of ligands, 2,2'-bipyridine, linear aliphatic amines and branched aliphatic amines ligands, have been developed to enhance either the solubility of the catalyst, adjust the redox potential of the copper for appropriate reactivity of the catalyst, or both. Recently, a new branched aliphatic amine, tris(2-(dimethylamino)ethyl)amine (Me₆tren, structure shown in Figure 3.8), has been used as ligand to improve the catalyst system for the ATRP of acrylates (Xia et al., 1998). This catalyst system allows well-controlled polymerization of acrylates at ambient temperature with very fast polymerization rates. For some polymerizations, termination might be enhanced at elevated temperature because of rapid initiation of polymerization. Thus, an ambient temperature could be an optimal condition for the surface-initiated ATRP process, in which the concentration of the initiators is rather low (Matyjaszewski et al., 1999), and can give rise to the larger thickness of the polymer brushes grafted from the substrate. Recently, a surface-initiated ATRP on gold substrate using the Cu/Me₆tren catalyst system at ambient temperature has been demonstrated (Kim et al., 2000).

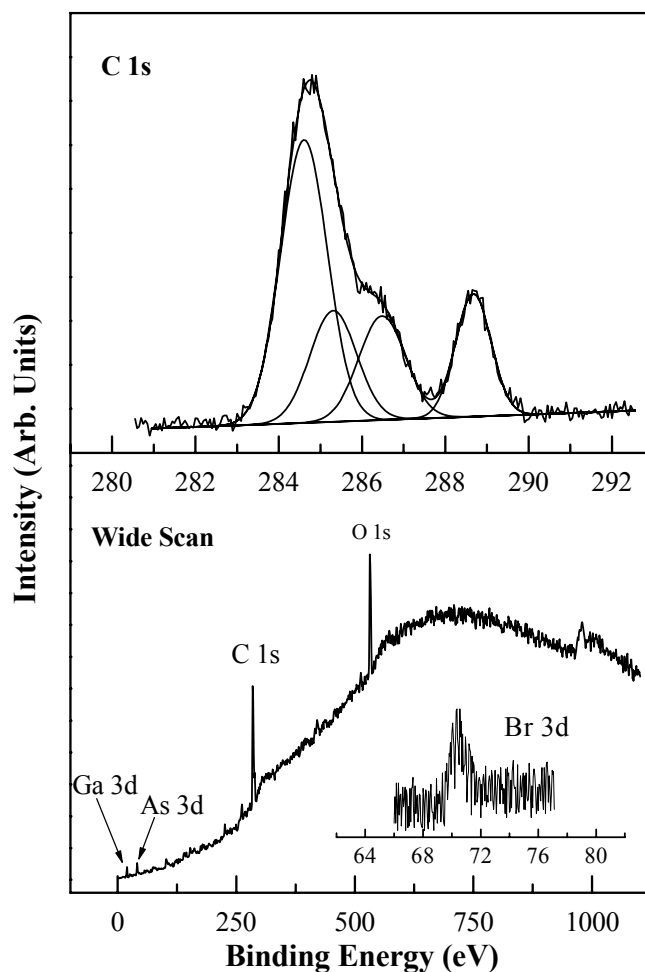


Figure 3.9 XPS spectra of C 1s and wide scan of the GaAs-PMMA hybrids (Sample PMMA1, Table 3.2) surface.

XPS was again used to characterize the PMMA polymer brushes grafted on the GaAs surface. Figure 3.9 shows the high-resolution C 1s core-level and wide scan spectra of the GaAs-PMMA1 (Table 1) sample surface. The C 1s core-level line shape is dominated by that of PMMA. The spectrum consists of four peak components with BE's at 284.6 eV for the aliphatic hydrocarbons ($\underline{\text{C}}\text{-C}$ and $\underline{\text{C}}\text{-H}$ species), 285.3 eV for the $\underline{\text{C}}\text{-COO}$ species, 286.4 eV for the $\underline{\text{C}}\text{-O}$ species, and 288.6 eV for the $\text{O}=\underline{\text{C}}\text{-O}$ species. The $[\text{C-H/C-C}]:[\text{C-COO}]:[\text{C-O}]:[\text{O}=\underline{\text{C}}\text{-O}]$ molar ratio, as determined from the

C 1s spectral component area ratio, is 2.8:1.2:1.1:1. This ratio deviates somewhat from the theoretical ratio of 2:1:1:1 for PMMA. The deviation from the ideal PMMA composition probably has resulted from the contribution of the underlying initiator and thiol coupling agent to the aliphatic hydrocarbon species, as the PMMA film thickness (~ 9 nm) is comparable to the sampling depth of the XPS technique (see below). With the increase in PMMA film thickness, the surface composition approaches that of the pure PMMA. The inset in Figure 3.9 shows the Br 3d core-level spectrum of the GaAs-PMMA1 (Table 3.2) sample surface. The persistence of the Br signal is consistent with the fact that the PMMA chain growth from the surface was a surface-initiated polymerization process with a living characteristic.

The chemical states of the GaAs-PMMA hybrid interface with a PMMA film thickness of about 9 nm (Sample GaAs-PMMA1, Table 3.2) were also investigated by XPS. Since the probing depth of the XPS technique for hydrocarbon polymers is ≤ 10 nm, the As 3d and Ga 3d signals of the hybrid should have originated mainly from the top-most surface of the GaAs substrate after the grafting of about 9 nm of PMMA. Only a trace amount of As oxide and no Ga oxide species were observed in the XPS spectra of the GaAs-PMMA interface (Figure 3.10), suggesting that the surface-initiated ATRP has minimal effect on the chemical states of GaAs surface and the surface-coupled 6-mercapto-1-hexanol has also served as a passivation layer for the GaAs surface.

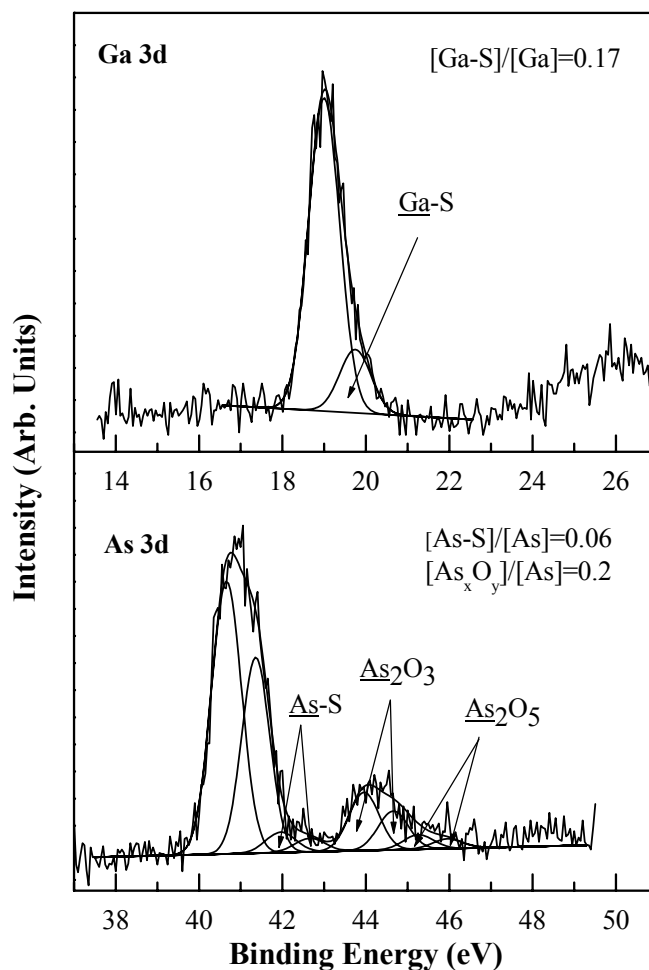


Figure 3.10 XPS Ga 3d and As 3d core-level spectra of the GaAs-PMMA hybrids interface (Sample PMMA1, Table 3.2) .

The concentrations of the gallium sulfide species, $[Ga-S]/[Ga]$ for the GaAs-PMMA surface have increase to 0.17 from the 0.06 for the GaAs- R_1OH surface in Figure 3.3, due to the fact that only the Ga 3d XPS signal originated from the top-most layer of the GaAs substrate is discernible after a PMMA film of 9 nm in thickness has been grafted from the substrate. However, the concentration of arsenic sulfide species, $[As-S]/[As]$, is only about 0.06, which is significantly lower than the concentration of the

gallium sulfide species of the GaAs-PMMA hybrid (Sample PMMA1, Table 3.2). the result suggests that the As-S bonds on the GaAs surface are somewhat unstable. This phenomenon is also consistent with those reported in the literature that Ga-S bonds on GaAs surface are thermodynamically more stable than the As-S bonds, as well as the fact that the Ga-S bonds dominate on the GaAs surface after the substrate has been annealed at temperatures above 400 °C (Seker et al., 2000).

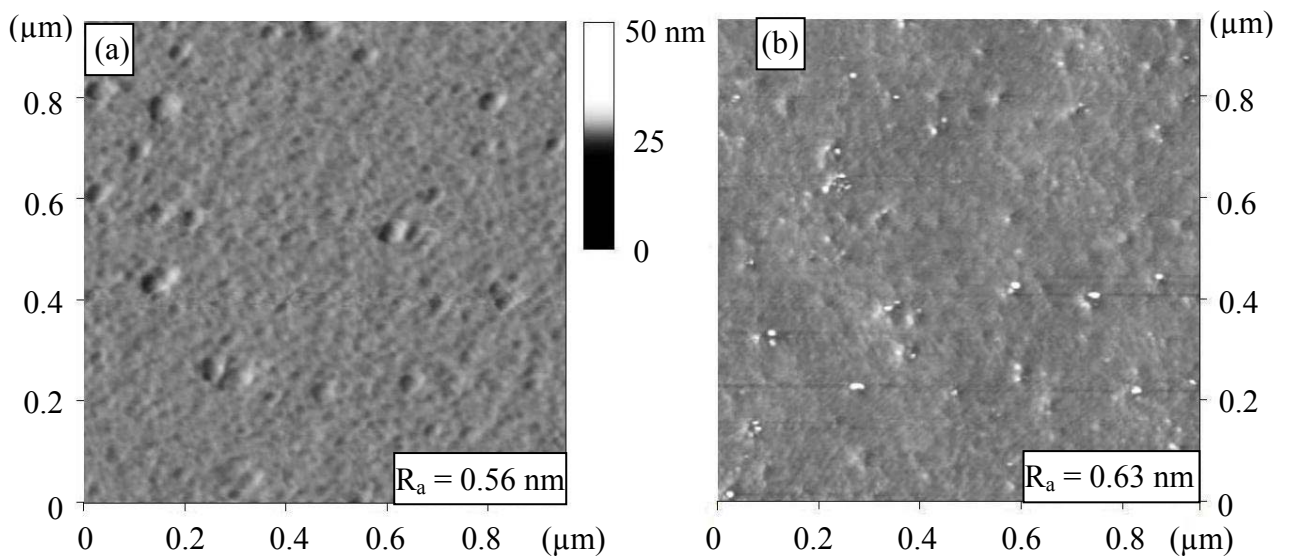


Figure 3.11 AFM images of (a) the HCl-etched GaAs surface and (b) the GaAs-PMMA hybrid (Sample GaAs-PMMA4, Table 3.2) surface.

The surface morphology of the GaAs-PMMA hybrid and the HCl-etched GaAs was studied by AFM. Figures 3.11(a) and 3.11(b) show the respective AFM images of the HCl-etched GaAs and the GaAs-PMMA hybrid (Sample GaAs-PMMA4, Table 1) surfaces. The surface roughness ($R_a \sim 0.63$ nm) of the GaAs-PMMA hybrid remains comparable to that of the original HCl-etched GaAs surface ($R_a \sim 0.56$ nm). The

nanoscopic uniformity of the GaAs-PMMA hybrid surface can be attributed to the well-defined PMMA brushes prepared from the surface-initiated ATRP.

The process of surface-initiated ATRP of MMA on GaAs-R₂Br surface was also verified by two parallel experiments. The experiments involved the immersion of (i) the GaAs-R₁OH substrate into the continuously stirred MMA monomer solution of CuBr (14.3 mg, 0.1 mmol), CuBr₂ (2.2 mg, 0.01 mmol), and Me₆TREN (26 μl, 0.11 mmol), and (ii) the GaAs-R₂Br substrate in the continuously stirred MMA monomer without CuBr, CuBr₂, and Me₆TREN for 12 h at room temperature. No change in thickness of the organic layer was detected by ellipsometry for samples from both experiments, consistent with the fact that surface-initiated ATRP of MMA occurred only in the presence of both the surface initiator and the Cu catalyst.

3.4 Conclusions

Surface-initiated ATRP on the functionalized GaAs single crystal surface has allowed the successful preparation of GaAs-PMMA hybrids at room temperature. The surface states of the GaAs substrate were not significantly affected by the ATRP process. Not only did the mercaptohexanol coupling agent give rise to the covalently bonded ATRP initiator, it also passivated the GaAs surface via the formation of the Ga-S and As-S covalent bonds. Thus, the present study provides a simple approach to the preparation of the GaAs-polymer hybrids with well-defined polymer brushes and preserved interfacial states.

Chapter 4

**ZnO-PMMA Core-Shell Hybrid Nanoparticles via
Surface-Initiated Atom Transfer Radical Polymerization
and Their Enhanced Optical Properties**

4.1 Introduction

Inorganic nanoparticles have attracted much interest due to their size-dependent electrical, optical, and magnetic properties (van, Dijken, 1998; Jun, 2000; Gangopadhyay, 1992). In order to take advantage of these properties on the macroscopic scale, the particles were usually incorporated into a matrix with specific processing properties, such as an organic polymer matrix, to form an inorganic-organic hybrid. Not only can this method allow a better dispersion of the particles in the matrix, it also protects the particles against the influence of the environment. Popular strategies for preparing inorganic-organic core-shell hybrid include “graft to” approach, in which the polymer chains were grafted onto the surface of the inorganic nanoparticles by chemisorption of the polymers with reactive groups (Benouada, 1988; Chhabra, 1995). The “graft from” approach attempts to grow polymer chains from initiators anchored on the surface of the inorganic particles. The latter approach, especially with the surface-initiated atom transfer radical polymerization (ATRP) technique, offers a versatile method for controlling the thickness and composition of the polymer shell in an inorganic-organic core-shell hybrid. Well-defined polymer shells grafted from silica (von Werne, 1999 and 2001; Pyun, 2001), Au (Nuss, 2001), Fe_2O_3 (Wang, 2003; Li, 2004), and MnFe_2O_4 (Vestal 2002) nanoparticles via surface-initiated ATRP have been reported recently.

As a wide band gap (3.37 eV) semiconductor with large exciton binding energy (60 meV), ZnO is one of the most promising materials for optoelectronic applications. ZnO has intrigued much research interest and various nanostructures of ZnO have

been successfully synthesized (Meulenkamp, 1998; Huang, 2001; Guo, 2002; Lao, 2003; Wang, 2004). Inorganic-organic hybrids based on ZnO nanoparticles have potential applications in hybrid solar cell (Beek, 2004), transparent UV-protection (Li, 2002), emission and display technology (Ghis, 1991), and as pharmaceutical and biomedical materials (Niemeyer, 2001). Recent developments in the preparation of inorganic-polymer hybrids from other inorganic nanoparticles have inspired us to synthesize ZnO-polymer core-shell hybrid nanoparticles via surface-initiated ATRP.

In this Chapter, ZnO-polymer core-shell hybrid nanoparticles, with well-defined polymer shell or polymer brushes of about the same chain length in the shell, were prepared via surface-initiated ATRP of methyl methacrylate (MMA) from ATRP initiators immobilized on ZnO nanoparticles. The hybrid nanoparticles were well-dispersed and gave rise to enhanced UV-visible absorption and fluorescence. The chemical composition of the hybrid nanoparticles was investigated by XPS. The morphology and structure of the nanoparticles were determined by field emission scanning electron microscopy (FE-SEM) and transmission electron microscopy (TEM).

4.2 Experimental

4.2.1 Materials

ZnO nanoparticles (mean particle size of 60 ± 10 nm and a surface area of 15-25 m²/g), 2-bromo-2-methylpropionic acid, methyl methacrylate (MMA), N,N,N',N'',N''-pentamethyldiethyltriamine (PMDETA), and copper(I) bromide (CuBr) were obtained from Aldrich Chemical Company, Milwaukee, WI. The MMA monomer was distilled under reduced pressure and stored in an argon atmosphere at -10 °C. For purification, CuBr was stirred in glacial acetic acid overnight, washed with ethanol, and dried under reduced pressure at 60 °C.

4.2.2 Immobilization of ATRP Initiator on ZnO Nanoparticle Surface

About 200 mg of ZnO nanoparticles were stirred overnight in 3 mM aqueous solution of 2-bromo-2-methylpropionic acid (R₁Br) initiator. The nanoparticles were collected by centrifugation and washed several times to remove the excess initiator. The surface-functionalized nanoparticles (ZnO-R₁Br nanoparticles) were dried under reduced pressure.

4.2.3 Surface-Initiated Atom Transfer Radical Polymerization from ZnO-R₁Br Nanoparticles

The ZnO-R₁Br nanoparticles were added into 5 ml MMA solution (MMA: 2.5 ml; acetonitrile: 1.25 ml; THF: 1.25 ml). After the mixture was purged with argon for 20 min, CuBr (16.7 mg, 0.117 mmol) and PMDETA (25 μl, 0.117 mmol) were added to the mixture. The final mixture was stirred and kept at 60°C for a pre-determined

period of time under an argon atmosphere. After the reaction, the mixture was washed with methanol to remove the Cu(I) catalyst. The surface-graft polymerized ZnO nanoparticles were collected by centrifugation and washed repeatedly with THF.

4.2.4 Characterization

(1) XPS Measurements. The chemical composition of the pristine and the functionalized ZnO nanoparticles was investigated by X-ray photoelectron spectroscopy (XPS). The XPS measurements were performed on a Krato AXIS HSi spectrometer using a monochromatic Al K α X-ray source (1486.71 eV photons). The samples were prepared by placing several drops of THF-nanoparticle mixture on 0.5×0.5 cm² Si(100) wafers. After the removal of the solvent, the Si wafers were mounted on the sample stubs by doubled-side adhesive tapes.

(2) FE-SEM and TEM Measurements. The morphology and structure of the pristine and the functionalized ZnO nanoparticles was determined by field emission scanning electron microscopy (FE-SEM) and transmission electron microscopy (TEM). FE-SEM measurements were made on a JEOL JSM-6700F SEM with an electron kinetic energy of 15 kV. The samples were prepared by placing a drop of THF-nanoparticle mixture on a 0.5×0.5 cm² Si(100) wafer. Investigation by transmission electron microscopy (TEM) was carried out on a JEOL JEM-2010 TEM with an electron kinetic energy of 200 kV. The samples for TEM measurement were prepared by placing a drop of THF-nanoparticle mixture on a carbon-coated 200-mesh copper grid.

(3) UV-visible and Fluorescence Measurements. The optical properties of the pristine and the functionalized ZnO nanoparticles were investigated by UV-visible and

fluorescence spectroscopies. UV-visible absorption spectroscopy measurements were carried out on a Shimadzu UV-3101 PC scanning spectrophotometer using THF as reference. The fluorescence spectra were obtained on a Shimadzu RF 5301PC luminescence spectrophotometer.

4.3 Results and Discussion

4.3.1 Synthesis and Characterization of ZnO-PMMA Hybrids

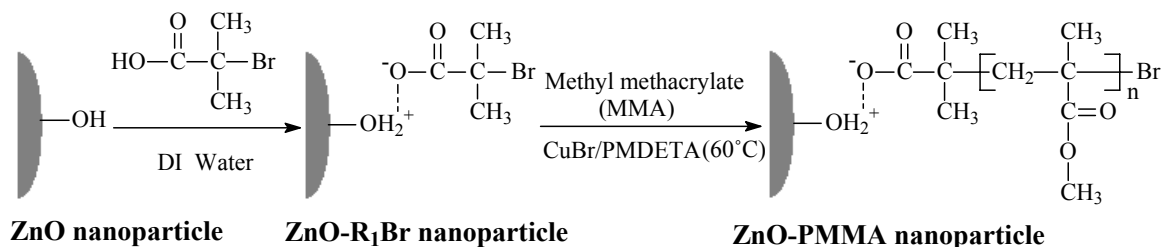


Figure 4.1 Schematic illustration of immobilization of ATRP initiators on the surface of ZnO nanoparticles and the surface-initiated ATRP to give rise to the ZnO-PMMA core-shell hybrids nanoparticles.

The strategy for preparing ZnO-PMMA hybrid nanoparticles via surface-initiated ATRP is shown in Figure 4.1. It consists of immobilization the ATRP initiators (2-bromo-2-methylpropionic acid) on ZnO nanoparticles to form the ZnO-R₁Br nanoparticles, and subsequent surface-initiated ATRP of MMA from the ZnO-R₁Br nanoparticle surface. Figure 4.2(a) shows the wide scan, Zn 2p core-level, and Zn Auger LMM spectra of the pristine ZnO nanoparticles. The Zn 2p core-level spectrum shows a spin-orbit-split doublet with binding energies (BE's) at about 1021.5 eV (2p_{3/2}) and 1044.5 eV (2p_{1/2}). In addition, the Zn (LMM) Auger has a kinetic energy of about 988.8 eV. These combined XPS results confirm the chemical state of ZnO (Moulder et al., 1992).

The ATRP initiator, 2-bromo-2-methylpropionic acid, was immobilized on the ZnO nanoparticle surface via acid-base interaction (Noguera, 1996). The immobilization of

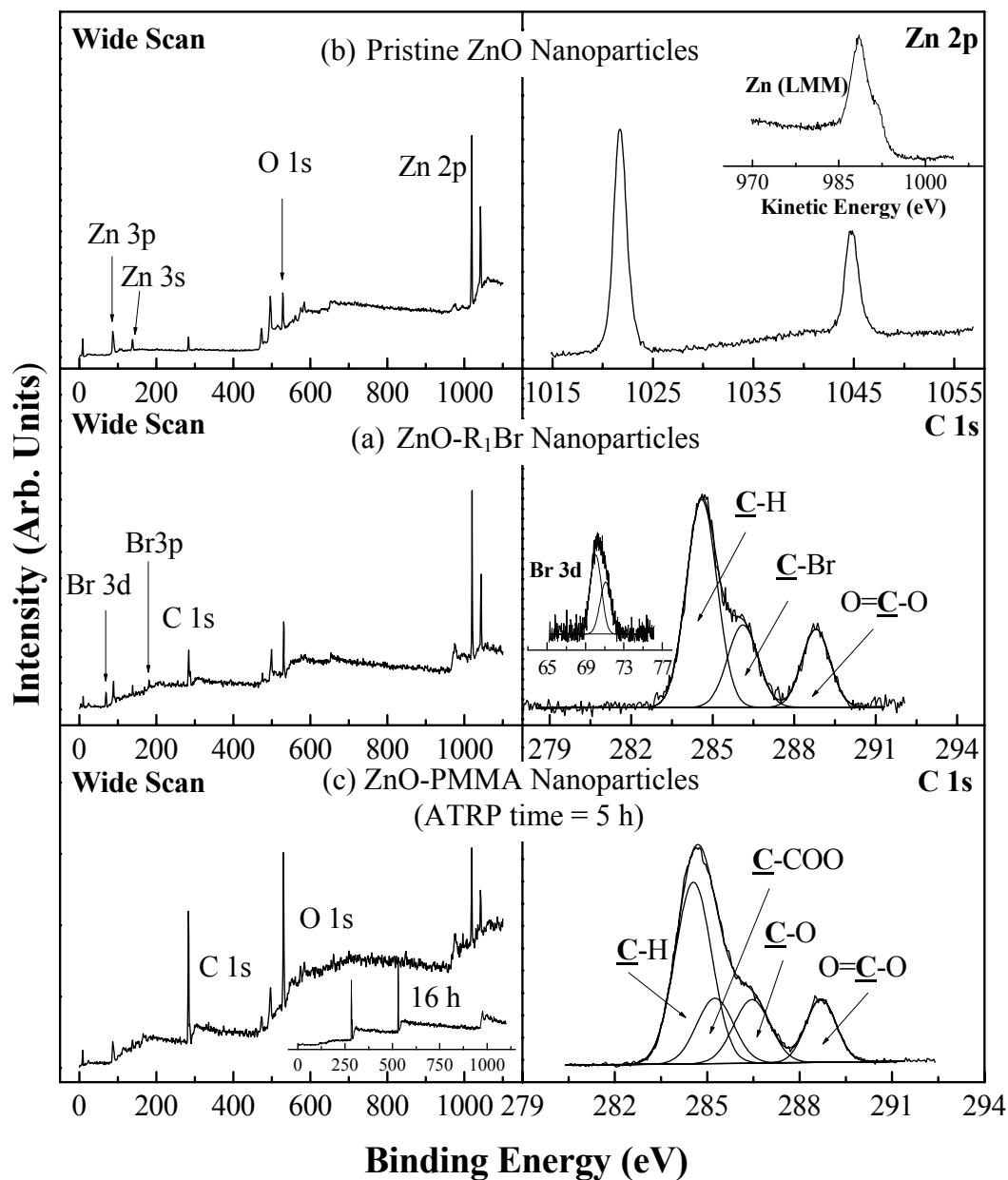


Figure 4.2 XPS core-level and wide scan spectra of (a) pristine ZnO nanoparticles, (b) the ZnO- R_1 Br nanoparticle, and (c) the ZnO-PMMA hybrid nanoparticles with ATRP time of 5 h. the insert in the (a) the Auger LMM spectra of pristine of ZnO nanoparticles

ATRP initiator, 3-chloropropionic acid, on the MnFeO_4 nanoparticles via acid-base interaction has been reported (Vestal et al., 2002). Under normal conditions of application, a metal oxide surface in contact with ambient atmosphere will give rise to the hydroxyl groups, which are strongly bonded to the surface (Noguera, 1996). Since ZnO (with the hydroxyl groups bonded to the surface) has a strong surface basicity (Parks, 1965), it will facilitate the coupling of 2-bromo-2-methylpropionic acid to a ZnO nanoparticle surface via acid-base interaction. However, a high concentration of 2-bromo-2-methylpropionic acid in an aqueous solution having a low pH value may destroy the ZnO nanoparticle. Thus, a 3 mM aqueous solution of 2-bromo-2-methylpropionic acid (pH value of 5-6) was used for the immobilization of the ATRP initiator on the ZnO nanoparticle surface. The successful immobilization of the ATRP initiators on the ZnO nanoparticle surface was confirmed by the appearance of a Br 3d spin-orbit-split doublet at the BE's of about 70 eV ($3d_{5/2}$) and 71 eV ($3d_{3/2}$) for the ZnO- R_1Br surface (the inset in Figure 4.1(b)). In addition, the C 1s core-level spectrum of the ZnO- R_1Br surface in Figure 4.2 (b) consists of three peak components with BEs at about 284.6 eV for the $\underline{\text{C}}\text{-H}$ species, 286.1 eV for the $\underline{\text{C}}\text{-Br}$ species, and 288.8 eV for the $\text{O}=\underline{\text{C}}\text{-C}$ species (Beamson, et al., 1993). The $[\text{C-H}]:[\text{C-Br}]:[\text{O}=\text{C-O}]$ molar ratio, as determined from the C 1s spectral peak component area ratio, is 2.6:1:0.9. This ratio deviates somewhat from the theoretical ratio of 2:1:1 for 2-bromo-2-methylpropionic acid. The deviation is probably due to hydrocarbon contamination, as the $[\text{C-Br}]:[\text{O}=\text{C-O}]$ molar ratio remains very close to the theoretical ratio.

The resulting ZnO-R₁Br nanoparticles were dispersed in 5 ml of MMA solution (MMA: 2.5 ml; acetonitrile: 1.25 ml; THF: 1.25 ml), containing CuBr and PMDETA, for the surface-initiated ATRP at 60°C. After the ATRP process, the ZnO nanoparticles with surface-grafted MMA polymer (PMMA shell), or the ZnO-PMMA hybrid nanoparticles, were dispersed in the THF. It was found that the time required for the ZnO-PMMA hybrid nanoparticles to precipitate increased with the ATRP time. This phenomenon is consistent with the presence of a thicker PMMA shell grafted on the ZnO nanoparticle surface with increasing ATRP time. After the surface-initiated ATRP of MMA on the ZnO-R₁Br nanoparticle surface for 5 h at 60°C, the resulting ZnO-PMMA hybrid nanoparticles, were recovered and analyzed by XPS. Figure 4.2(c) shows the wide scan and high-resolution C 1s core-level spectra of the ZnO-PMMA hybrid nanoparticles surface. A reduced Zn 2p signal and an enhanced C 1s signal are observed for the ZnO-PMMA hybrid nanoparticles. The Zn 2p signal became undetectable for the ZnO-PMMA hybrid nanoparticles from an ATRP time of 16 h (the inset in Figure 4.2(c)). Since XPS is a surface sensitive technique having a probing depth less than 10 nm for organic compounds (Briggs, 1998), the decrease in Zn 2p signal with increase in ATRP time is consistent with the presence of a thicker PMMA shell grafted from the ZnO nanoparticle surface. The C 1s core-level line shape of the ZnO-PMMA hybrid nanoparticles in Figure 4.2(c) is characteristic of that of PMMA (Beamsom, et al., 1993). The spectrum consists of four peak components with BE's at 284.6 eV for the aliphatic hydrocarbons (C-C and C-H species), 285.4 eV for the C-COO species, 286.4 eV for the C-O species, and 288.6 eV for the O=C-

O species. The [C-H/C-C]:[C-COO]:[C-O]:[O=C-O] molar ratio is 2.3:1:1:0.8, which is comparable to the theoretical ratio of 2:1:1:1 for PMMA.

4.3.2 Morphology and Structure of the Hybrid Nanoparticles

Much work has been done to control the aggregation of inorganic particles. One promising way to avoid the aggregation of nanoparticles is to surround them with an appropriate coating layer, consisting of organic molecules and polymers. Surface-initiated ATRP, by which polymer chains grow from the metal oxide surface, allows the control over molecular weight and gives a low polydispersity index (von Werne, 1999 and 2001; Pyun, 2001). Thus, the process may give rise to uniform shell thickness around the metal oxide core and result in a well-defined inorganic-organic core-shell structure. In order to investigate the aggregation states, the morphology and structure of the ZnO-PMMA hybrid nanoparticles were characterized by FE-SEM and TEM. Figures 3.3(a) and 3.3(b) show the representative FE-SEM images of the pristine ZnO nanoparticles and the ZnO-PMMA hybrid nanoparticles from an ATRP time of 5 h, respectively. As shown in Figure 3.3(a) the as-received pristine ZnO nanoparticles are prone to aggregation, whereas, the ZnO-PMMA hybrid nanoparticles can remain well-dispersed (Figure 3.3(b)). The few aggregates probably have resulted from the entanglement of PMMA chains during solvent evaporation, which may bridge the space between the ZnO nanoparticles (von Werne, 1999). This kind of aggregation became more prominent with higher concentration ZnO-PMMA suspension in THF used to prepare the FE-SEM samples. Figure 4.4 shows the representative TEM images of individual ZnO-PMMA core-shell hybrid nanoparticles

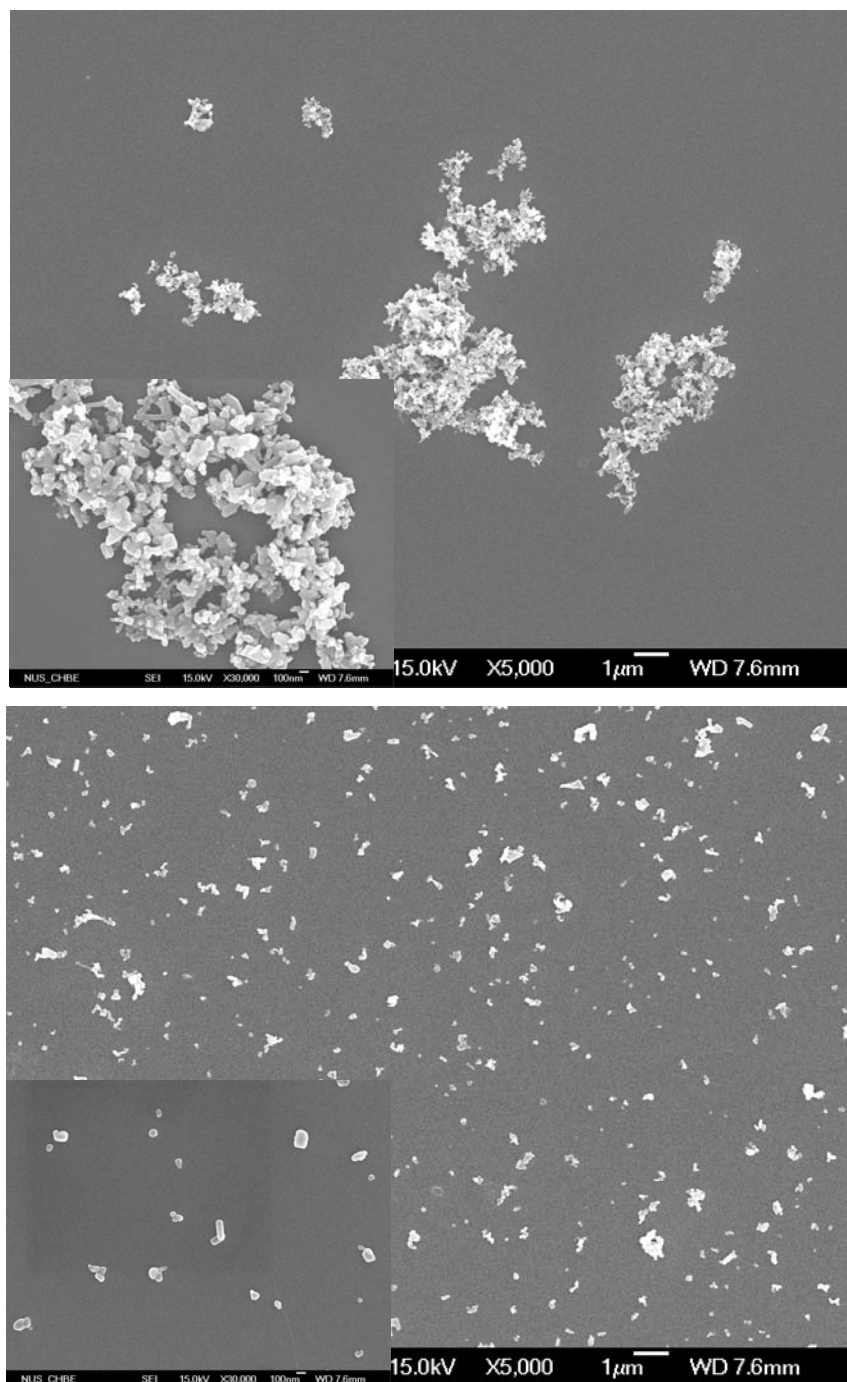


Figure 4.3 Representative FE-SEM images of (a) the pristine ZnO nanoparticles and (b) the ZnO-PMMA hybrid nanoparticles after ATRP for 5 h

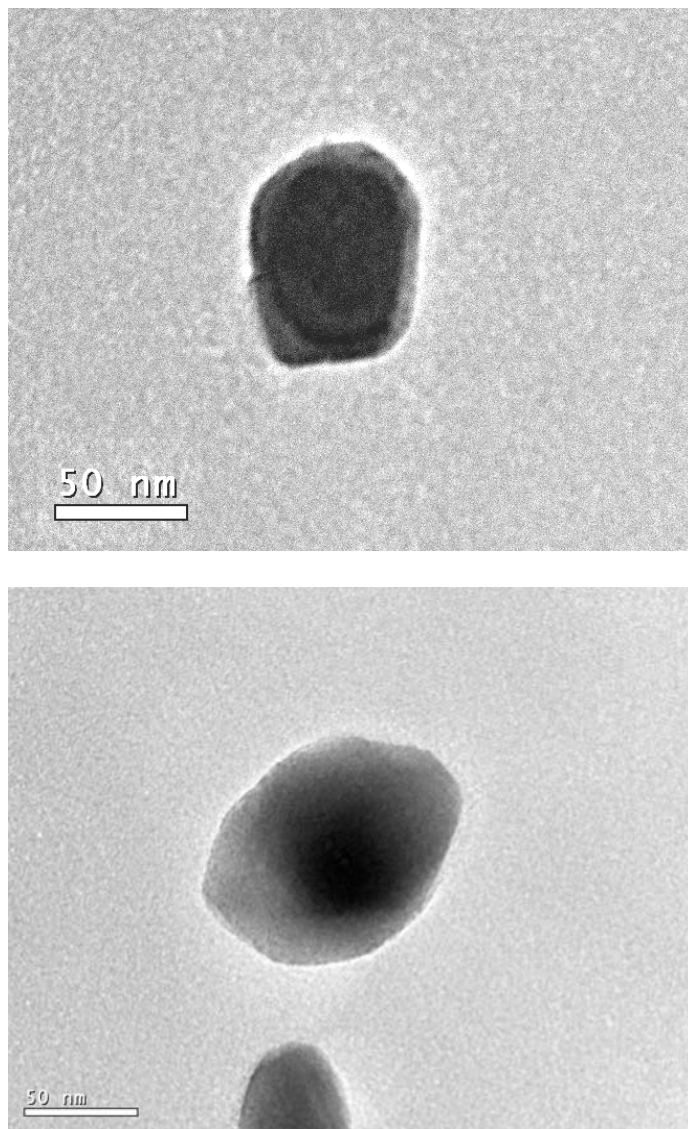


Figure 4.4 Representative TEM images of the ZnO-PMMA hybrid nanoparticles after ATRP for (a) 5 h and (b) 16 h

after ATRP for 5 h (part (a)) and 16 h (part (b)). The core-shell nanoparticle morphology in both images can be readily observed. The light contrast shell presumably is associated with PMMA, while the dark contrast core to ZnO. The PMMA shell around the ZnO nanoparticles probably has prevented the interaction among the ZnO nanoparticles, resulting in well-separated ZnO-PMMA hybrid

nanoparticles, as shown in Figure 4.3(b). As shown in the Figure 4.4(b), the interface between the PMMA shell and ZnO nanoparticle is not discernible for the hybrid nanoparticle obtained from the longer ATRP time of 16h. The phenomenon is probably due to the presence of a thicker polymer shell. The thicker PMMA shell observed for the hybrid nanoparticle with an ATRP time of 16 h is also consistent with the XPS result shown in the inset of Figure 4.2(c).

To obtain the highly dispersed ZnO nanoparticles, organic capping ligand (triethylphosphine oxide or TOPO) and poly(vinylpyrrolidone) (PVP) have been used to synthesize ZnO nanoparticle (Kim, 2003; Guo, 2000). It was believed that TOPO and PVP stabilized the surface of the ZnO nanoparticle and gave rise to highly dispersed nanoparticles. Commercial ZnO nanoparticles are most commonly prepared by a high temperature processes. The ZnO nanoparticles aggregate inevitably due to interactions among the nanoparticles. Not only can the present surface-initiated ATRP process gives rise to the well-dispersed ZnO-PMMA hybrid nanoparticles by shielding the interactions among the ZnO nanoparticles, the thickness of the PMMA shell on the ZnO-PMMA hybrid nanoparticles is well-defined and adjustable.

4.3.3 UV-visible Absorption and Photoluminescence Spectra of the ZnO-PMMA Hybrid Nanoparticles

Figure 4.5 shows the UV-visible absorption spectra of the PMMA, pristine ZnO, and ZnO-PMMA hybrid nanoparticles (with ATRP durations of 5 h and 16 h) in THF at room temperature. Significantly enhanced exciton absorption band at 375 nm,

corresponding to the electron transition from the top of the valence band to the exciton levels of ZnO, were observed for the organic-functionalized ZnO nanoparticles (Li, 2004). The improved excitonic absorption for the ZnO-PMMA hybrid nanoparticles is probably originate from the improved separation or dispersion of pristine ZnO nanoparticles by the capping PMMA layer on the surface, resulting in larger surface area of the pristine ZnO nanoparticle exposed to the incident light. The improved excitonic absorption property due to the improved separation of pristine ZnO nanoparticles is also consistent with the slight red shift of the excitonic absorption peak of ZnO nanoparticle aggregates (377 nm) (Sakohara, 1998). As PMMA have insignificant absorbance in this spectral region, no significant difference in the exciton

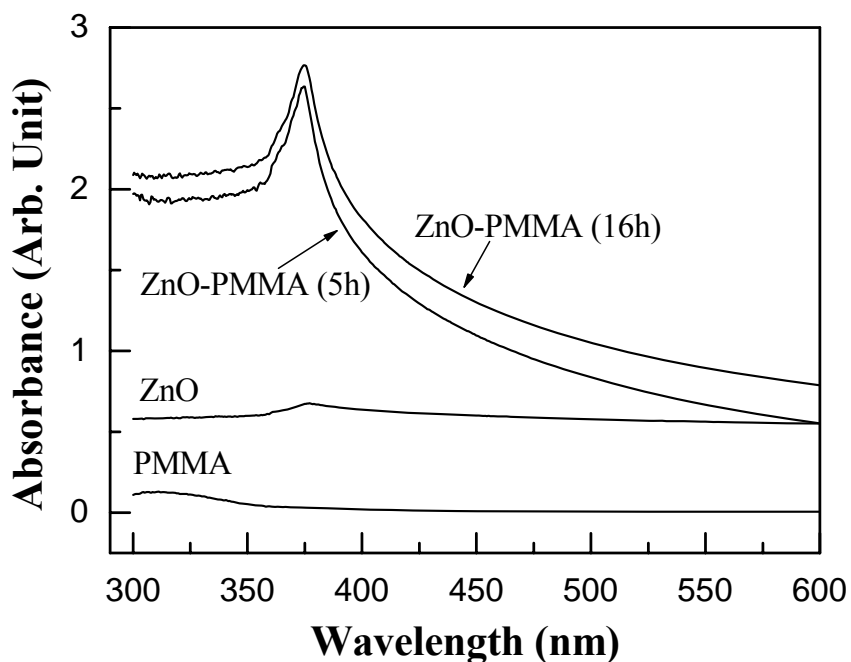


Figure 4.5 UV-Visible absorption spectra of PMMA, pristine ZnO, ZnO-PMMA hybrid nanoparticle. Surface-initiated ATRP was performed for 5 h and 16 h

absorption spectra is discernible for the ZnO-PMMA hybrid nanoparticles with different thickness of the PMMA shell. These results suggest that ZnO-PMMA hybrid nanoparticles can improve the UV absorption of the pristine ZnO nanoparticles.

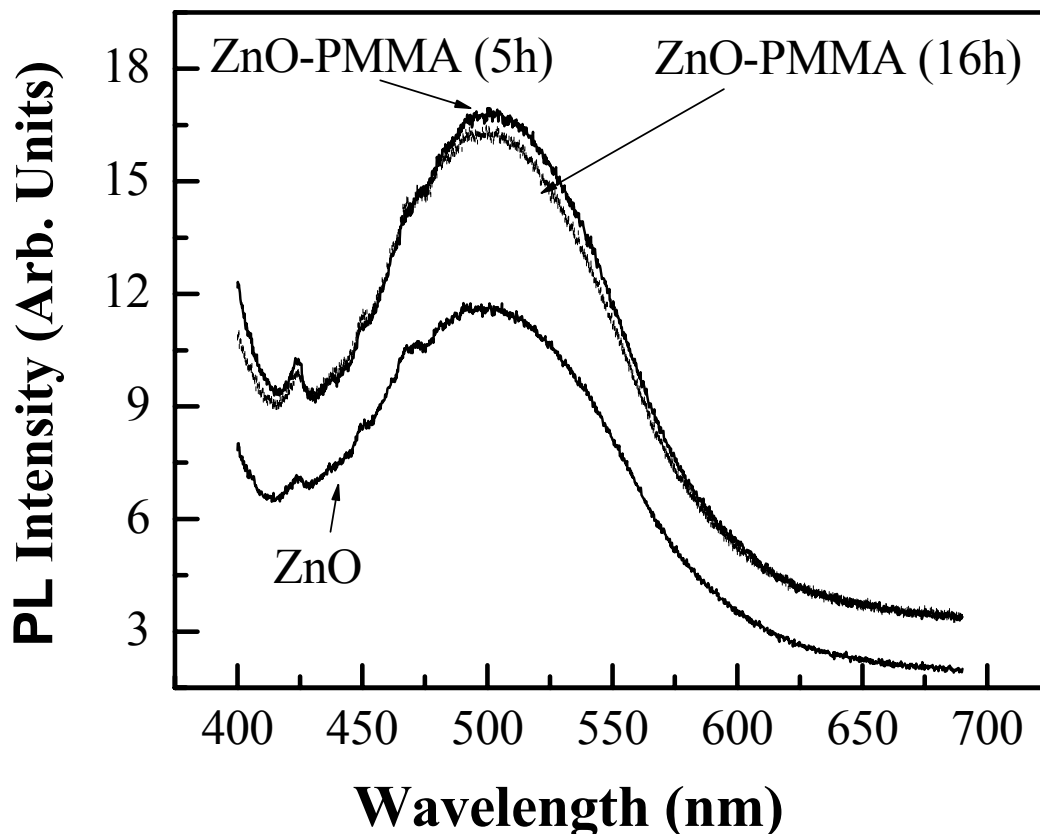


Figure 4.6 Fluorescence spectra of the pristine ZnO and ZnO-PMMA hybrid nanoparticles after surface-initiated ATRP for 5 h and 16 h. ($\lambda_{\text{ex}} = 375 \text{ nm}$)

Figure 4.6 shows the fluorescence spectra of the pristine ZnO and ZnO-PMMA hybrid nanoparticles excited at the wavelength of 375 nm from a Xe lamp. The fluorescence spectra are dominated by the emission band at about 500 nm, which is attributed to the singly ionized oxygen vacancy on the surface of ZnO nanoparticles and resulted from

the radiative recombination of the electrons in the singly occupied oxygen vacancy with the photogenerated holes in the valence bands (Vanheusden, 1996). The deviation in the emission band compared to those in other reports (Guo, 2000; Vanheusden, 1996) is probably due to the difference ZnO particle size. The intensity of the emission band at about 500 nm for the ZnO-PMMA hybrid nanoparticles after surface-initiated ATRP for 5 h and 16 h are significantly stronger than that of the pristine ZnO nanoparticles. This result is probably attributable again to the well-dispersed nature of the organic functionalized ZnO nanoparticles in THF, in which holes in the valence band could be more effectively photogenerated. This result is also consistent with that observed in the UV-visible absorption spectra. Pristine ZnO and ZnO-PMMA nanoparticles were also dispersed in other organic solvent (dimethylformamide (DMF) and dimethyl sulfoxide (DMSO)) for optical characterizations. Similar optical properties of improved UV absorption and Enhanced PL intensity was also observed for ZnO-PMMA nanoparticles, suggesting well-dispersion of ZnO-PMMA nanoparticles in DMF and DMSO.

Poly(vinylpyrrolidone) (PVP)-modified and highly dispersed ZnO nanoparticles have been synthesized and their optical properties have been investigated (Guo et al., 2000). It was found that the intensity of the green emission band at about 530 nm decreased due to surface modification of the ZnO nanoparticles by PVP. It was suggested that the elimination of the surface states of ZnO nanoparticles by PVP chelation during the preparation of PVP-modified ZnO nanoparticles have given rise to the decrease in the green emission intensity. In the present work, the pristine ZnO nanoparticles were

immobilized with ATRP initiators via acid-base interactions between the hydroxyl groups on the pristine ZnO nanoparticles and carboxyl groups of the ATRP initiators. The surface-initiated ATRP from the ATRP initiators was subsequently carried out to synthesize the ZnO-PMMA core-shell hybrid nanoparticles. Thus, the pristine surface states of ZnO nanoparticles were preserved to some extent and the intensity of the visible emission at about 500 nm was subsequently enhanced due to the well-dispersed nature of the ZnO nanoparticle functionalized by the present approaches.

4.4 Conclusions

ZnO-PMMA core-shell hybrid nanoparticles were successfully prepared via surface-initiated ATRP of methyl methacrylate (MMA) from ATRP initiators immobilized on ZnO nanoparticles by acid-base interaction. The chemical compositions of the nanoparticles were investigated by X-ray photoelectron spectroscopy (XPS). The morphology and structure of the nanoparticles were determined by field emission scanning electron microscope (FE-SEM) and transmission electron microscope (TEM). In addition, the optical properties of the nanoparticles were also studied by UV-visible and photoluminescence spectroscopies. The ZnO-PMMA hybrid nanoparticles so-prepared could be well-dispersed in THF. Significant enhancements in UV-visible absorption and fluorescence intensities were observed.

Chapter 5

Self-Assembled Monolayers of ZnO Colloidal Quantum Dots (QDs)

on 3-Mercaptopropyltrimethoxysilane-Passivated GaAs(100)

Surfaces

5.1 Introduction

Semiconductor quantum dots (QDs), exhibiting unique properties arising from three-dimensional (3D) quantum confinement, have emerged as potential materials for the fabrication of novel semiconductor devices and for biotechnology (Bimberg et al., 1999; Niemeyer, 2001; Katz and Willner, 2004). There are two widely investigated semiconductor QDs, one of them is the self-assembled semiconductor QDs from heteroepitaxial growth (Mo et al., 1990; Guha et al., 1990; Leonard et al., 1993; Carlsson et al., 1994; Moison et al., 1994; Heinrichsdorff et al., 1996; He et al., 2004; Rastelli et al., 2004) and the other is nanocrystal semiconductor QDs synthesized via wet-chemistry (Alivisatos, 1996; Peng et al., 1998; Rogach et al., 2002; Joo et al., 2003). For the heteroepitaxially-grown semiconductor QDs, their formation is driven by the strain energy from lattice mismatch (Stranski-Krastanow (SK) growth). The size and size distribution of the SK-grown semiconductor QDs are dictated by the strain parameters. The colloidal semiconductor QDs, on the other hand, are synthesized typically in organic solvents via colloidal chemistry. The size can be varied during synthesis to result in a wide range of tunable electronic energy levels.

Recently, the successful integration of colloidal semiconductor QDs into epitaxial nanostructures were demonstrated via a combination of wet-chemistry and molecular beam epitaxial (MBE) growth (Madhukar et al., 2005 and Woggon et al., 2005). The integrated colloidal semiconductor QDs have no epitaxial relationship to the substrate and thus do not rely on the strain induced by lattice-mismatch. In principle, these additional degrees of freedom in choosing the composition and size of colloidal

semiconductor QDs provide more options for the nanostructures of the semiconductor quantum devices. For the technical application of hybrid nanostructures, the organization of spatially and dimensionally well-ordered colloidal semiconductor QDs on substrates will be crucial.

In this Chapter, an alternative approach to the preparation of self-assembled monolayers (SAMs) of ZnO colloidal semiconductor QDs, which have potential applications in optoelectronics (Ohta et al., 2003 and 2004) and spintronics (Dietl, 2002 and Norton et al., 2004), on the technically important GaAs(100) single-crystal substrate was demonstrated.

5.2 Experimental

The oxide layer on GaAs(100) wafers were removed by treatment with concentrated HCl solution for two min. The GaAs substrates (1 cm × 3 cm) were subsequently passivated and functionalized by immersion in 5 mM degassed heptane solution of 3-mercaptopropyltrimethoxysilane (MPTMS) for 12 h at room temperature. The resulting substrates were washed with heptane and immersed into the diluted colloidal solutions of ZnO QDs for 3 h. The ZnO colloidal QDs were synthesized following the procedures described in the literature (Meulenkamp, 1998). The colloidal ZnO QDs were stabilized by pyridine, hexylamine, and octadecylamine, respectively. The colloidal solution of ZnO QDs was purified by several cycles of precipitating and redispersing. The pyridine-stabilized ZnO (ZnO-PD) QDs were dispersed in ethanol and the hexylamine- and octadecylamine-stabilized ZnO (ZnO-HA and ZnO-ODA) QDs were dispersed in heptane. One mL of purified colloidal solution, containing ~ 2 mg of the ZnO QDs, was diluted with 200 mL ethanol or heptane to produce a stable colloidal solution of ZnO QDs with little aggregation. The resulting colloidal solutions were aged for 24 h. The ZnO QDs were self-assembled on the functionalized GaAs substrates in the aged ZnO QDs solution for 3 h. The GaAs substrates functionalized with ZnO QDs were washed with ethanol and heptane, and dried under reduced pressure.

Characterization by transmission electron spectroscopy (TEM) was carried out by Philips CM300 TEM operating at 300 kV. The X-ray diffraction (XRD) pattern was recorded on a Bruker GADDS XRD with Cu K α radiation. UV-visible absorption

spectroscopy measurements were carried out on a Shimadzu UV-3101 PC scanning spectrophotometer. X-ray photoelectron spectroscopy (XPS) measurements were performed on a Krato AXIS HSi spectrometer using a monochromatized Al K α X-ray source. Fluorescence spectra were obtained on a Shimadzu RF 5301PC luminescence spectrophotometer. Atomic force microscopy (AFM) images were obtained on a Digital Instrument Nanoscope IIIa apparatus, using the tapping mode.

5.3 Results and discussion

The strategy is illustrated in Figure 5.1. The procedures consist of: (i) removal of the oxide layer on the GaAs substrate by concentrated HCl, (ii) simultaneous functionalization and passivation of the less stable GaAs surface by SAMs of 3-mercaptopropyltrimethoxysilane (MPTMS), and (iii) self-assembly of the as-synthesized ZnO colloidal QDs on the MPTMS-passivated GaAs surface via the well-established coupling reaction of the silane groups and ZnO QDs (Hung et al., 2005). The bifunctional ligand, MPTMS, is the key to successful self-assembly of ZnO colloidal QDs on the passivated GaAs substrates.

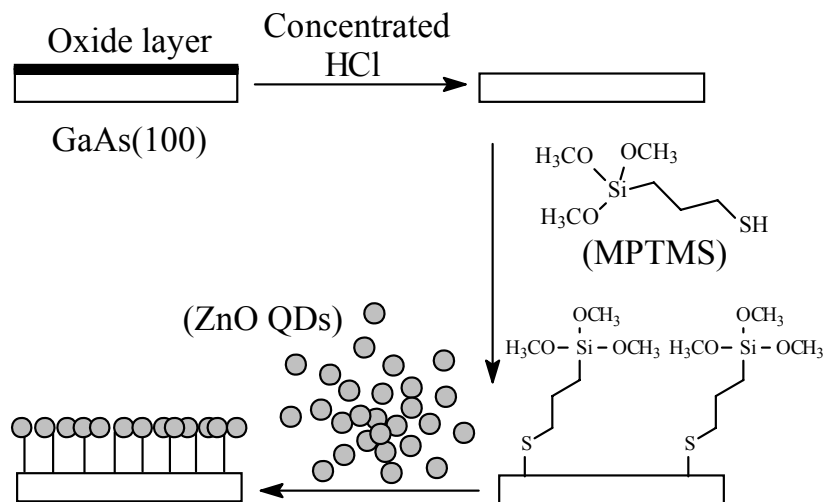


Figure 5.1 Schematic illustration of the self-assembled monolayers of ZnO colloidal QDs on a MPTMS-passivated GaAs(100) substrate.

ZnO colloidal QDs were synthesized following the procedure described in the literature (Meulenkamp, 1998) and were stabilized by pyridine (ZnO-PD), hexylamine (ZnO-HA), and octadecylamine (ZnO-ODA), respectively. Figure 5.2(a) shows a

high-resolution transmission electron microscopy (TEM) image of the as-synthesized ZnO-PD colloidal QDs. The QDs are quite uniform in both shape and size. The average size was about 3.2 nm. The inset in Figure 5.2(a) shows the high-resolution TEM image of the ZnO-PD colloidal QDs. Well defined lattice fringes from the QDs are discernible.

The X-ray diffraction (XRD) pattern of the colloidal QDs in Figure 5.2(b) shows an exact match to that of the hexagonal ZnO. The broadening of the diffraction peaks is due to the very small crystallite size. The average size of the ZnO colloidal QDs can also be estimated from Scherrer's equation (Koch et al., 1985). By calculating the broadening of the XRD diffraction peak at (110), the average crystallite size of the ZnO colloidal QDs was about 3.1 nm, which is very close to the average size of 3.2 nm estimated from the TEM image of the colloidal QDs in Figure 5.2(a).

The UV-visible absorption spectrum of the as-synthesized ZnO-PD colloidal QDs dispersed in ethanol is shown in Figure 5.2(c). The band-gap of the QDs can be determined by locating the wavelength at which the absorption is 50% of that at the excitonic peak, termed $\lambda_{1/2}$ (Meulenkamp, 1998). As shown, $\lambda_{1/2}$ is located at about 341 nm, corresponding to a band-gap of 3.63 eV. The band-gap is significantly wider than that (3.37 eV) of the bulk ZnO crystals, which is consistent with the quantum size effect of the ZnO colloidal QDs (Koch et al 1985 and Bahnemann et al., 1987). Figure 5.2(d) shows the excitation and emission spectra of the ZnO-PD colloidal QDs

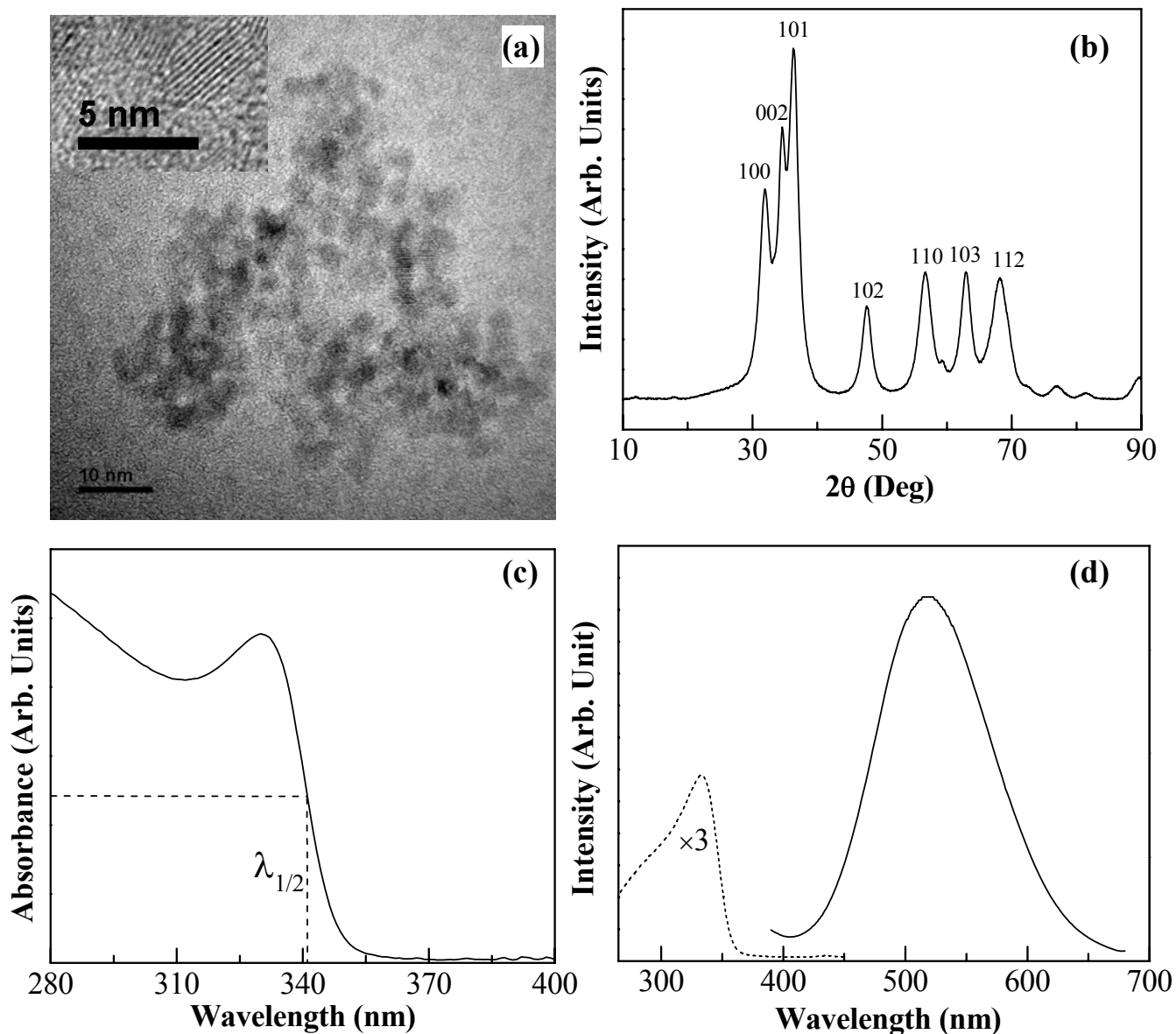


Figure 5.2 (a) TEM image of the as-synthesized ZnO colloidal QDs. The inset is the high-resolution TEM image showing the lattice fringes of single ZnO colloidal QDs. (b) Powder X-Ray diffraction spectrum of the as-synthesized ZnO colloidal QDs. (c) UV-visible absorption spectrum of the ZnO colloidal QDs dispersed in ethanol ($\lambda_{1/2}$ locates at 341 nm, corresponding to a band-gap of 3.63 eV; band-gap of bulk ZnO crystals is 3.37 eV). (d) Excitation (dash line) and emission (solid line) spectra of ZnO colloidal QDs dispersed in ethanol.

dispersed in ethanol. The excitation spectrum has a peak at about 331 nm, which is comparable to that of the excitonic peak. The emission spectrum is dominated by the emission band at about 519 nm (Hung et al., 2005).

Prior to self-assembly of the ZnO colloidal QDs on the GaAs(100) substrate, the GaAs(100) surface was functionalized by the silane end group of the passivating MPTMS. Figures 5.3(a-c) show the respective X-ray photoelectron spectroscopy (XPS) wide scan, As 3d, and Ga 3d spectra of the MPTMS-passivated GaAs surface. The As 3d core-level spectrum consists of two spin-orbit-split doublets. The major doublet has binding energies (BEs) at about 40.7 eV ($3d_{5/2}$) and 41.4 eV ($3d_{3/2}$), attributed to the GaAs species (Moulder et al., 1992). The minor doublet with BEs at about 42.0 eV ($3d_{5/2}$) and 42.7 eV ($3d_{3/2}$) is attributable to the As-S species on the GaAs surface (Spindt et al., 1989; Hou et al., 1997; Shaporenko et al., 2003; Cai et al., 2005). The Ga 3d core-level spectrum consists of two peak components at the BEs of 19.0 eV and 19.7 eV, attributable to the GaAs species and Ga-S species (Spindt et al., 1989; Hou et al., 1997; Shaporenko et al., 2003; Cai et al., 2005), respectively. The inset in Figure 5.3(a) shows the XPS spectrum in the Si 2p BE region. In spite of the partial overlap with the Ga 2p spin-orbit-split doublet, the Si 2p peak with a BE of about 101.9 eV and associated with the silane species (Moulder et al., 1992), is discernible. The O 1s peak at about 532.0 eV in the wide scan spectrum is associated predominantly with the methoxysilane of MPTMS, as no As oxides (BE > 44 eV) and Ga oxide (BE ~ 20.4 eV) (Moulder et al., 1992) species are discernible in the As 3d and Ga 3d core-level spectra of the passivated GaAs surface. The XPS results thus

indicate that the GaAs(100) surface has been passivated by MPTMS through covalent As-S and Ga-S bonds, while functionalized simultaneously by its silane group.

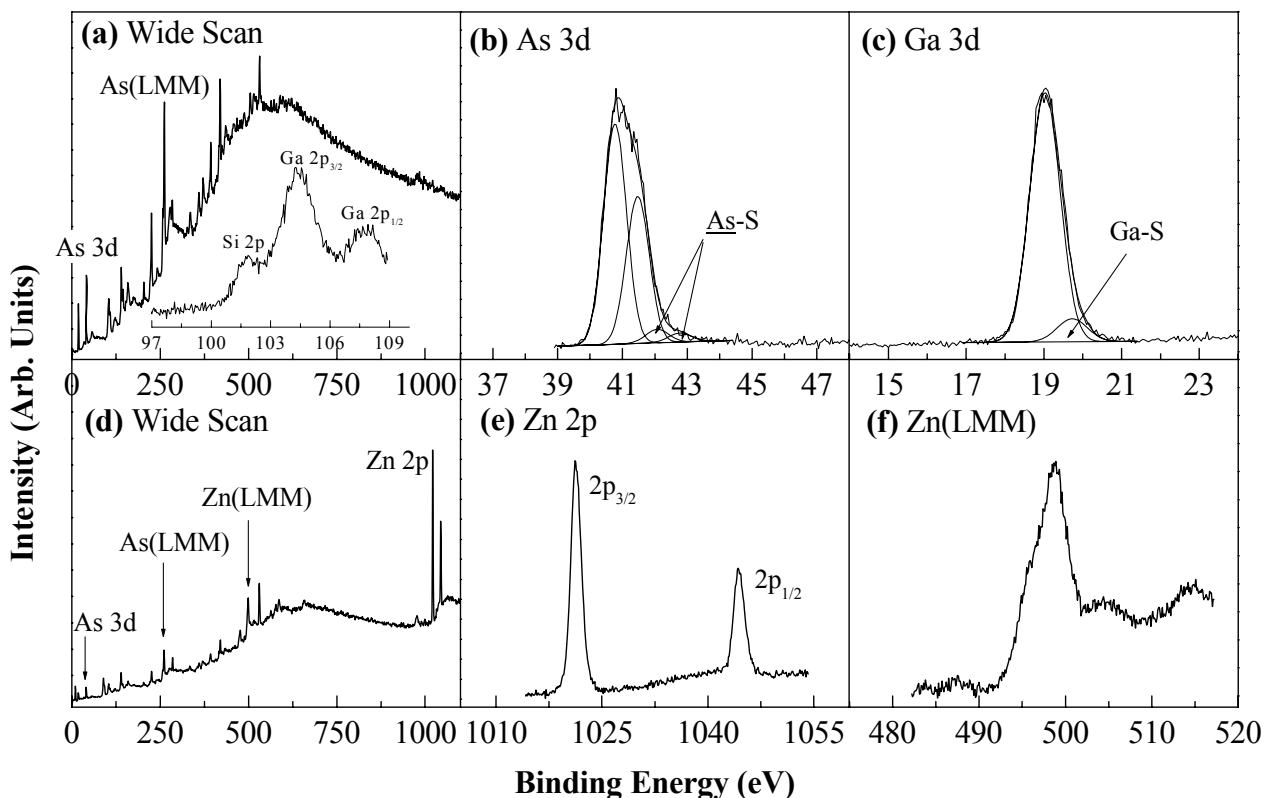


Figure 5.3 XPS (a) wide scan, (b) As 3d core-level, and (c) Ga 3d core-level spectra of the MPTMS-passivated GaAs surface, and XPS (d) wide scan spectrum, (e) Zn 2p core-level spectrum, and (f) Zn (LMM) Auger line of ZnO colloidal QDs self-assembled on the MPTMS-passivated GaAs surface. The inset in (a) is the XPS spectrum in the BE region of Si 2p.

Figures 5.3(d-f) show the respective wide scan, Zn 2p, and Zn(LMM) Auger spectra of the MPTMS-passivated GaAs surface with the SAMs of ZnO QDs. In comparison with the XPS wide scan spectrum in Figure 5.3(a), the XPS wide scan spectrum in Figure 5.3(d) reveals the appearance of distinct Zn 2p core-level and Zn(LMM) Auger signals. The Zn 2p core-level spectrum shows a spin-orbit-split doublet with BEs at about 1021.5 eV (2p_{3/2}) and 1044.5 eV (2p_{1/2}). In addition, the Zn (LMM) Auger line

has a BE of about 498.2 eV, with the corresponding kinetic energy of about 988.5 eV. These XPS results indicate that the chemical state of the colloidal QDs is ZnO (Moulder et al., 1992) and self-assembly of the QDs on the MPTMS-passivated GaAs surface has been achieved. Since the XPS probing depth for ZnO is less than 5 nm (Seah et al., 1979), the persistence of distinct Ga and As signals in Figure 5.3(d), together with the fact that the size of the ZnO QDs is about 3.2 nm, suggests that the self-assembled ZnO QDs on the GaAs(100) substrate probably exist as a monolayer.

Table 5.1 Surface morphology of the GaAs substrates

Surface	R _a (nm)	R _q (nm)	R _z (nm)
HCl-etched GaAs(100)	0.44	0.56	4.56
MPTMS-passivated GaAs	0.19	0.26	3.38
ZnO-PD colloidal QDs on MPTMS-Passivated GaAs	0.59	0.79	8.69
ZnO-HA colloidal QDs on MPTMS-Passivated GaAs	2.40	3.06	25.22
ZnO-ODA colloidal QDs on MPTMS-Passivated GaAs	5.34	6.77	45.60

R_a: Mean roughness; R_q: Root mean square roughness; R_z: Ten-point mean roughness.

The key role of MPTMS as a coupling agent for the ZnO QDs was verified by two parallel experiments. HCl-etched GaAs substrate and dodecanethiol-passivated GaAs substrates were dipped into the respective heptane solutions of ZnO-PD, ZnO-HA, and ZnO-ODA colloidal QDs for 3 h. No Zn 2p signal was detectable on both substrates. The result is consistent with the fact that the ZnO colloidal QDs self-

assembled on the MPTMS-passivated GaAs surface via coupling reaction with the silane end groups of MPTMS.

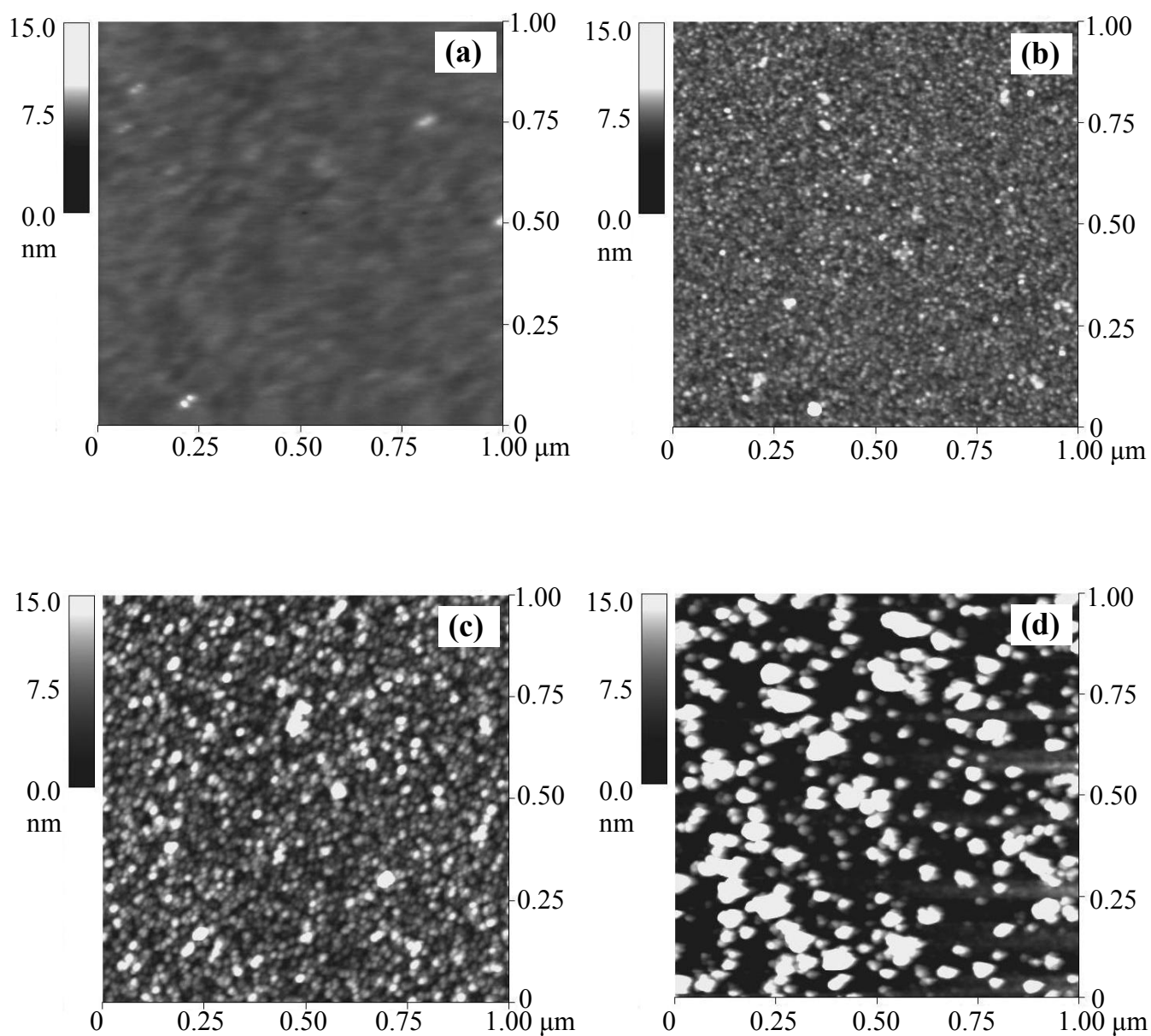


Figure 5.4 AFM images of MPTMS-passivated GaAs surface (a) before and after self-assembly of (b) ZnO-PD, (c) ZnO-HA, and (d) ZnO-ODA colloidal QDs.

The morphology of self-assembled ZnO-PD, ZnO-HA, and ZnO-ODA QDs on the MPTMS-passivated GaAs surface were investigated by atomic force microscopy

(AFM). The MPTMS-passivated GaAs surface (Figure 5.4(a)) appears to be very flat and homogenous, with surface roughness values less than those of the starting HCl-etched GaAs surface (Table 5.1). After the self-assembly of ZnO colloidal QDs, the surface roughness have increased substantially (Table 5.1). As shown in Figures 5.4(b-d), the bright spots were due to immobilization of ZnO QDs on GaAs surface (also could be referred as QDs). It was clear shown that, the bright spots are uniform on GaAs surface in the order of ZnO-PD > ZnO-HA > ZnO ODA, indicating the coverage of ZnO QDs on GaAs is in the order of ZnO-PD > ZnO-HA > ZnO-ODA. The alkyl chain length of the stabilizing ligands is in the order of ODA > HA > PD. Thus, the coverage of QDs on the MPTMS-passivated GaAs decreases with increasing alkyl chain length of the stabilizing ligands for the ZnO QDs. During the immobilization process for the QDs, the methoxysilane groups on the MPTMS-passivated GaAs surface will replace the weakly-bound stabilizing ligands on the surface of ZnO QDs. The coupling efficiency decreases as the molecular lengths of the ligands (hexylamine and octadecylamine) become longer than that of MPTMS. In addition, aggregation of QDs stabilized by long alkyl chains has occurred to a significant extent, as indicated by the substantial increase in QD size in Figure 5.4(c) and Figure 5.4(d). The AFM smearing problem on surfaces covered with particles (Schmitt et al., 1999), arising from the cone-shaped nature of the AFM tip, probably has also caused a slightly increase in the apparent lateral dimension of the nanoparticles.

5.4 Conclusions

In conclusion, a self-assembled monolayer of ZnO colloidal QDs on the MPTMS-passivated GaAs surface was demonstrated. Not only does MPTMS act as a coupling agent for the ZnO QDs, but also passivate the GaAs surface through the formation of covalent As-S and Ga-S bonds. Thus, the present study provides a simple approach to the self-assembly of semiconductor ZnO colloidal QDs on an oriented single crystal GaAs substrate with simultaneous passivation of the latter. The strategy developed in this work based on the mercaptosilane coupling agent can be readily extended to the fabrication of micropatterned SAMs of colloidal QDs on GaAs substrates, for example, by microcontact printing (Xia et al., 1998 and Husemann et al., 1999).

Chapter 6

Plasma Polymerization and Deposition of

Fluoropolymers on Hydrogen-Terminated Si(100) Surfaces

6.1 Introduction

In microelectronics, the signal delay caused by the interconnects becomes more important than that induced by the intrinsic gate-to-gate delay as the feature size of the integrated circuits decreases to below 0.18 μm (Maier, 2001). One method of lowering the interconnect delay is through the use of highly conductive metals and low capacitance dielectrics. Replacement of aluminium by copper gives rise to about 37% improvement in electrical conductivity. Silver exhibits higher electrical conductivity than copper. However, the difference is only 5% (Lide, 1999). Therefore, further advancement cannot be expected from metals. An alternative is to switch to insulating materials with dielectric constants lower than that of SiO_2 . Fluoropolymers are promising materials for interlayer dielectrics because of their low dielectric constants (low κ 's), low dissipation factors, and high thermal stability (Sacher, 1994). Unfortunately, most of the fluoropolymers suffer from limited processability (Endo et al, 1999). To overcome the processability problem, plasma enhanced chemical vapor deposition (PECVD) and plasma polymerization techniques have been used to prepare and deposit fluoropolymer films in the absence of a solvent [Clark et al., 1982; Coulson et al., 2000]. It is also a rapid, simple and low temperature process.

On the other hand, hydrogen-terminated single crystal silicon surface is a kinetically stable surface (Houston et al., 1995) that has been shown to react with terminal olefins and acetylenes to form densely packed and covalently attached monolayers through Si-C bonds. The surface reaction can be initiated by radical initiators (Linford et al., 1993 and 1995), thermal activation (Sung et al., 1997), or UV irradiation (Cicero et al.,

2000). Through the scission of the H-Si bonds, surface dangling bonds, which are reactive towards olefins and unsaturated organic species, are created on the silicon surface.

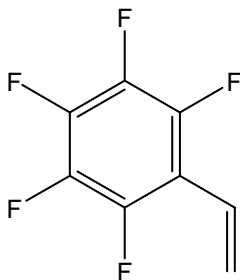
In this Chapter, ultra-thin fluoropolymer films (≤ 2 nm) were deposited directly on the hydrogen-terminated Si(100) (H-Si) and native oxides-covered Si(100) (ox-Si) surfaces by radio-frequency (rf) plasma polymerization of pentafluorostyrene (PFS), and hexafluorobenzene (HFB), 1H,1H,2H-heptadecafluoro-1-decene (HDFD), and perfluoroheptane (PFH). The chemical states at the fluoropolymer/Si interfaces were studied by XPS. In addition, thick fluoropolymer films (150-350 nm) were also deposited on the hydrogen-terminated surfaces by plasma polymerization of PFS, HFB, HDFD, and PFH. The chemical composition and structure of the fluoropolymer films were studied by XPS, time-of-flight secondary mass spectroscopy (ToF-SIMS), and Fourier transform infrared (FTIR) spectroscopy. The hydrophobicity of the fluoropolymer films was studied by water contact angle measurements. The surface topography of the films, on the other hand, was studied by AFM.

6.2 Experimental

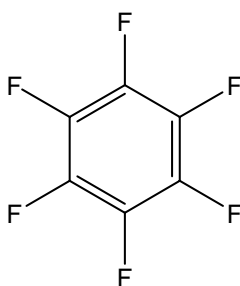
6.2.1 Materials (100)-oriented single-crystal silicon, or Si(100) wafers, having a thickness of about 0.7 mm and a diameter of 150 mm, were obtained from Unisil Co. of Santa Clara, CA. The as-received wafers were polished on one side and doped as n-type. The silicon wafers were sliced into rectangular strips of about 10 mm×20 mm. To remove the organic residues on the silicon substrate surface, the silicon strips were washed with the “piranha” solution, a mixture of 98 wt% concentrated sulfuric acid (70 vol%) and hydrogen peroxide (30 vol%) (wade et al, 1997) at 100°C for 30 min, followed by rinsing with copious amounts of doubly distill water. After the Si(100) strips were blown dry with argon atmosphere, they were further dried at 80°C in a vacuum oven for 1 h. The silicon substrates so-prepared were still covered with a layer of native oxides (ox-Si substrates). The clean ox-Si strips were subsequently immersed in 10 vol% hydrofluoric acid for 5 min to remove the oxide film. Prior to the immersion of the silicon strip, the hydrofluoric acid was sparged with argon atmosphere for 30 min through a Teflon[®] tube inserted into the solution. The hydrogen-terminated silicon (H-Si) surface was hydrophobic and thus emerged dry from hydrofluoric acid into air. The H-Si surface was not rinsed with any solvent to avoid oxidation or contamination by organics.

The four fluoro-monomers, pentafluorostyrene (PFS), hexafluorobenzene (HFB), 1H,1H,2H-heptadecafluoro-1-decene (HDFD), and perfluoroheptane (PFH), used for plasma polymerization were obtained from the Aldrich Chemical Co. of Milwaukee, WI. The monomers were subjected to several freeze-pump-thaw cycles to remove

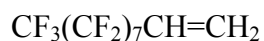
trapped atmospheric gases prior to plasma polymerization. The chemical structures of the four fluoro-monomers are shown below.



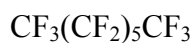
PFS



HFB



HDFD



PFS

6.2.2 Plasma Polymerization and Deposition

Plasma polymerization and deposition were carried out on the Plasmalab 80 Plus PECVD system manufactured by Oxford Instruments Plasma Technology of Yatton, UK. The RF generator was operated at a frequency of 13.56 MHz. The plasma deposition process was performed between two circular parallel plate electrodes of 24 cm in diameter and 6 cm in separation. The H-Si and ox-Si substrates were placed on

the ground electrode. The monomer was introduced into the glow discharge chamber by an argon-carrier gas. The gas mixture was allowed to flow evenly into the reactor from a distributor embedded in the upper electrode. In each case, the carrier gas stream was assumed to be saturated with the monomer, as dictated by the partial pressure of the monomer. To better preserve the molecular structure, the rf power for plasma polymerization under a predetermined system pressure was kept as lower as possible. For PFS and HDFD having the vinyl group, the glow discharge was ignited at an RF power of 15 W, a system pressure of 200 mTorr, and a gas flow rate of 30 standard cubic centimeter per min (sccm). For HFB and PFS, the glow discharge was ignited at the RF power of 50 W, a system pressure of 200 mTorr, and a gas flow rate of 30 sccm. With the controlled plasma power and duration time and system pressure, ultra-thin films were successfully deposited. The thicknesses of the films were measured by ellipsometry. The measurements were carried out on a variable angle spectroscopic ellipsometer (Model VASE, J. A. Woollam Inc., Lincoln, NE) at an incident angle of 65°, 70°, and 75°. Data were recorded and processed using the WVASE32 software package. All measurements were conducted in dry air at room temperature. Thickness values from at least 3 different surface locations of each sample were averaged. Fluoropolymer films were also deposited on KBr pellets for FTIR measurements.

6.2.3 Surface and Interface Characterization

X-ray photoelectron spectroscopy (XPS) was used to determine the chemical composition of the plasma-polymerized fluoropolymer/Si (pp-fluoropolymer/Si)

interfaces. The XPS measurements were carried out on the Kratos AXIS HSi spectrometer (Kratos Analytical Ltd., Manchester, England) with a monochromatic Al K α X-ray source (1486.6 eV photons) at a constant dwell time of 100 ms and a pass energy of 40 eV. The anode voltage and current were set at 15 kV and 10 mA, respectively. The samples were mounted on the sample stubs by double-sided adhesive tapes. A low-energy electron gun was used for charge neutralization on all the samples. The core-level signals were obtained at a photoelectron take-off angle (with respect to sample surface) of 90°. All binding energies (BE's) were referenced to the neutral hydrocarbon peak component at 284.6 eV. In curve fitting, the line width (full width at half-maximum or FWHM) for the Gaussian peaks was maintained constant for all components in a particular spectrum. Surface elemental stoichiometries were determined from peak-area ratios after correcting with the experimentally determined sensitivity factors, and were reliable to $\pm 10\%$. The elemental sensitivity factors were determined using stable binary compounds of well-established stoichiometries.

The topography of the plasma-polymerized fluoropolymer films on the H-Si substrates were characterized using a Nanoscope IIIa atomic force microscope (AFM) from the Digital Instrument Inc. In each case, an area of $1 \times 1 \mu\text{m}$ square was scanned using the tapping mode. The drive frequency was 330 ± 50 kHz, and the voltage was between 3 and 4 V. The drive amplitude was about 300 mV, and the scan rate was 1 Hz. A root mean square of the surface roughness (R_a) was calculated from the roughness profile determined by AFM.

The time-of-flight secondary ion mass spectrometry (ToF-SIMS) analyses were carried out on an ION-ToF SIMS IV instrument (ION-ToF, GmbH, Münster, Germany). The primary ion beam (10 keV Ar⁺) with a spot size of ~50 μm was adjusted on an area of 500 μm × 500 μm while keeping the total dose under 10¹³ ions/cm². The pressure in the analysis chamber was maintained at 1 × 10⁻⁹ Torr or lower during each measurement. To reduce the surface charging effect, an electron flood gun was used for the charge neutralization. The calibration of the mass spectra was based on the built-in mass library.

6.2.4 FTIR Measurements

The Fourier transform infrared (FTIR) spectra were recorded on a Bio-Rad FTIR, Model 400, spectrophotometer. Each spectrum was collected by cumulating 30 scans at a resolution of 8 wavenumbers.

6.2.5 Water Contact Angle Measurements

Static water contact angles of the ultra-thin and thick fluoropolymer films deposited on the H-Si surfaces were measured by the sessile drop method at 25°C and 65% relative humidity, using a contact angle goniometer (Model 100-00-(230), manufactured by Rame-Hart, Inc., Mountain Lake, NJ, USA). The telescope with a magnification power of 23× was equipped with a protractor of 1° graduation. Five readings from different locations on the fluoropolymer film surface were averaged.

6.3 Results and Discussion

6.3.1 Surface and Interfacial Characterization of Plasma-deposited Fluoropolymers on Silicon Surface by XPS

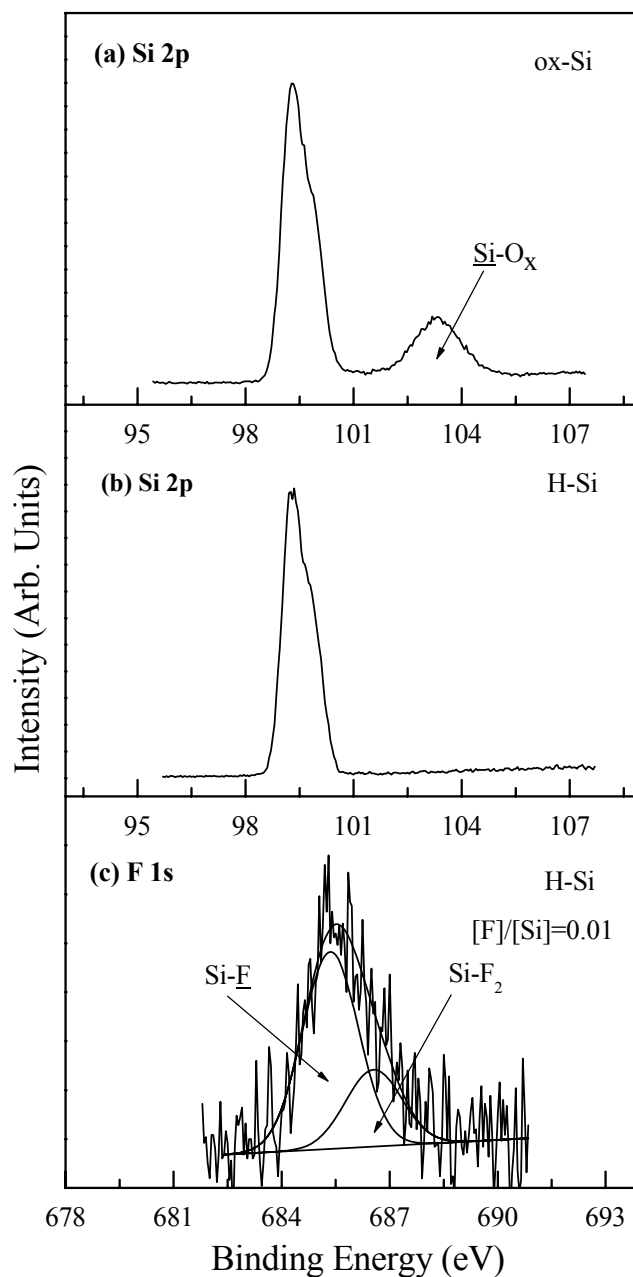


Figure 6.1 XPS Si 2p core-level spectra of (a) the pristine ox-Si surface, (b) HF-etched (Si)100 surface, and (c) F 1s core-level spectrum of the HF-etched Si(100) surface.

The chemical compositions of the ox-Si and H-Si surfaces before and after plasma deposition of the fluoropolymer films were determined by XPS. The plasma polymerized and deposited PFS, HFB, HDFD, and PFD films are referred as the pp-PFS, pp-HFB, pp-HDFD, and pp-PFH films, respectively. As shown in Figure 6.1(a), two peak component with binding energies (BE's) at about 99.3 and 103.3 eV, attributed to the $\underline{\text{Si}}\text{-Si}$ and $\underline{\text{Si}}\text{O}_x$ species, respectively (Moulder et al., 1992), are observed in the Si 2p core-level spectrum of the ox-Si surface. Etching of the ox-Si surface with dilute HF removes the native oxides layer and yields the H-Si surface (Higashi, 1990). The disappearance of the $\underline{\text{Si}}\text{O}_x$ species at the BE of 103.3 eV is consistent with the presence of a predominately hydrogen-terminated silicon surface after the HF etching (Figure 6.1(b)). In addition, etching of oxides-capped Si(100) wafers with dilute HF leaves behind a small amount of fluorine atoms bonded to silicon (Weinberger et al., 1986; Takahagi et al., 1988). Figure 6.1(c) shows the faint F 1s core-level signal of the H-Si surface. Two peak components, with BE's at 685.4 eV for the $\text{Si-}\underline{\text{F}}$ species (Little et al., 2000; Cao et al., 2002) and 686.6 eV for the $\text{Si-}\underline{\text{F}}_2$ species (Weinberger et al., 1986; Takahagi et al., 1988; Mitsuya et al., 1999) are discernable. The relative surface concentration of the fluorine atoms on the H-Si surface, defined as the $[\text{F}]/[\text{Si}]$ ratio, is about 0.01.

After the HF etching, the freshly etched Si(100) (H-Si surface) and the clean ox-Si substrate were sent into the plasma chamber for plasma polymerization and deposition of fluoropolymers. Figure 6.2 shows the respective wide scan and F 1s core-level spectra of the interfaces between the ultra-thin pp-PFS films and Si(100) surfaces

(both H-Si and ox-Si surfaces). For the F 1s core-level spectrum of the pp-PFS/H-Si interface shown in Figure 6.2(a), four peak components with BE's at about 685.4 eV for the Si-F species, at about 686.6 eV for the Si-F₂ species, at about 687.6 eV for the CF_x-C species, and at about 688.8 eV for the CF_x-CF_y species (beamson et al., 1993) are discernable. The [F]/[Si] ratio for the pp-PFS/H-Si interface is about 0.18. In addition, the surface concentration of the fluorine atoms which is bonded to the Si atoms ($([\text{Si-F}] + [\text{Si-F}_2])/[\text{Si}]$) is about 0.03, which is higher than that of the starting H-Si surface. These results suggest that fluorine ions, from defluorination of PFS monomer during the plasma polymerization, are bonded to Si atoms on the H-Si surface (Yang et al., 2002).

For the F 1s core-level spectrum of pp-PFS/ox-Si interface shown in Figure 6.2(b), on the other hand, the two peak components with BE's at about 687.7 and 686.6 eV are attributable to the CF_x-C species (Beamson et al, 1993) and the F-Si-O species ($[\text{F-Si-O}]/[\text{Si}] = 0.01$) (Ermolieff et al., 1991). The presence of the F-Si-O species suggests that the ox-Si surface was etched slightly by the F⁻ ions, created through defluorination of PFS during the plasma process (Ermolieff et al., 1991; Wright et al., 1989). However, the [F]/[Si] ratio is only about 0.02, significantly lower than that of the pp-PFS/H-Si interface.

As shown in Figure 6.2(a), the XPS signal originated from Si (Si 2p and Si 2s), C, and F (F 1s and F KLL Auger line) are discernible in the wide scan spectrum of pp-PFS/H-Si interface. However, the wide scan spectrum of pp-PFS/ox-Si interface

shows strong O signal (O 1s and O KLL Auger line) and the C 1s and F 1s signals are not discernible. These results are consistent with the fact that the [F]/[Si] ratio of pp-PFS/H-Si interface is significantly higher than that of pp-PFS/ox-Si interface.

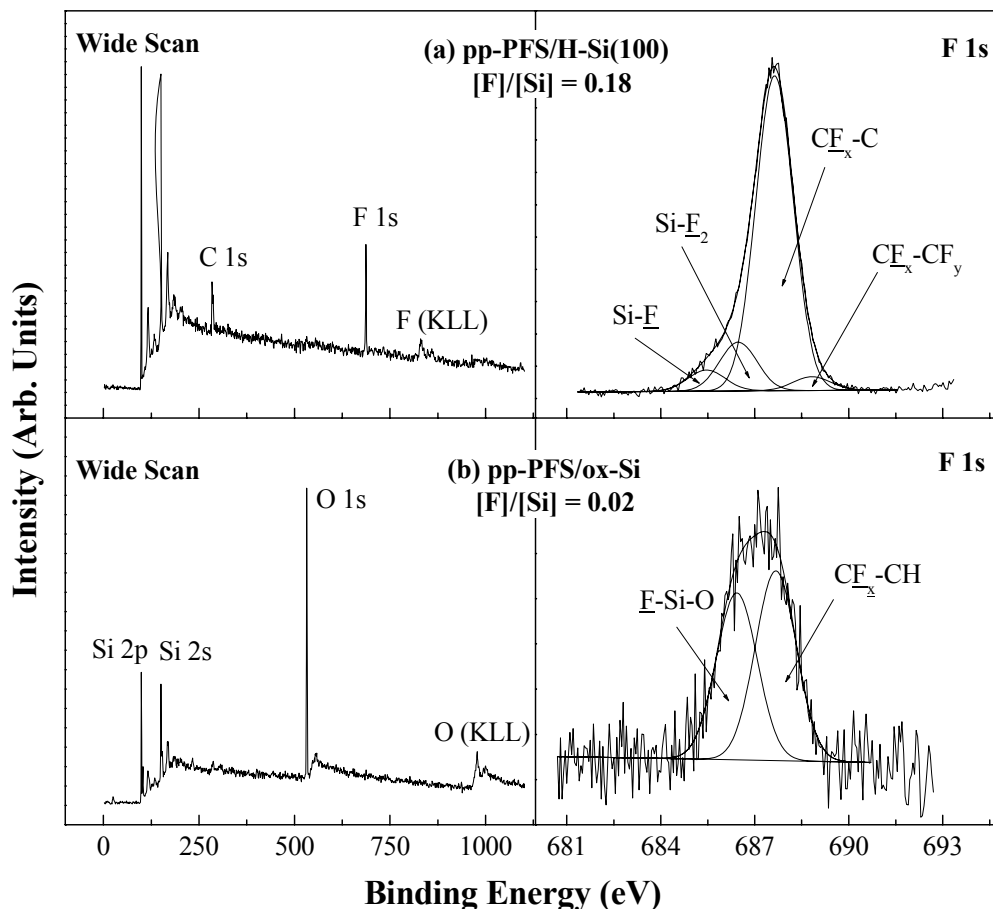


Figure 6.2 XPS wide scan and F 1s core-level spectra of (a) the ultra-thin pp-PFS/H-Si interface and the (b) ultra-thin pp-PFS/ox-Si interface.

Another aromatic fluoro-monomer, HFB, were also plasma polymerized and deposited on H-Si and ox-Si surfaces for further investigation of the interfaces between the fluoropolymer and Si surface. Compared to PFS, HFB does not have a vinyl group. Figure 6.3 shows the wide scan and F 1s core-level spectra of the interfaces of the pp-

HFB/H-Si (Figure 6.3(a)) and pp-HFB/ox-Si (Figure 6.3(b)). The XPS wide scan spectrum of pp-HFB/H-Si interface shows prominently the Si 2p, Si 2s, C 1s, and F 1s peaks. The F 1s core-level spectrum can be curve-fitted with four peak components with BE's at about 685.4 eV for the Si-F species, at 686.6 eV for the Si-F₂ species, at 687.6 eV for the C_{F_x}-C species, and at 688.8 eV for the C_{F_x}-CF_y. The [F]/[Si] and ([Si-F]+[Si-F₂])/[Si] ratios are about 0.34 and 0.07, respectively. The results suggest that the defluorination process has also occurred during the plasma polymerization and deposition of pp-HFB.

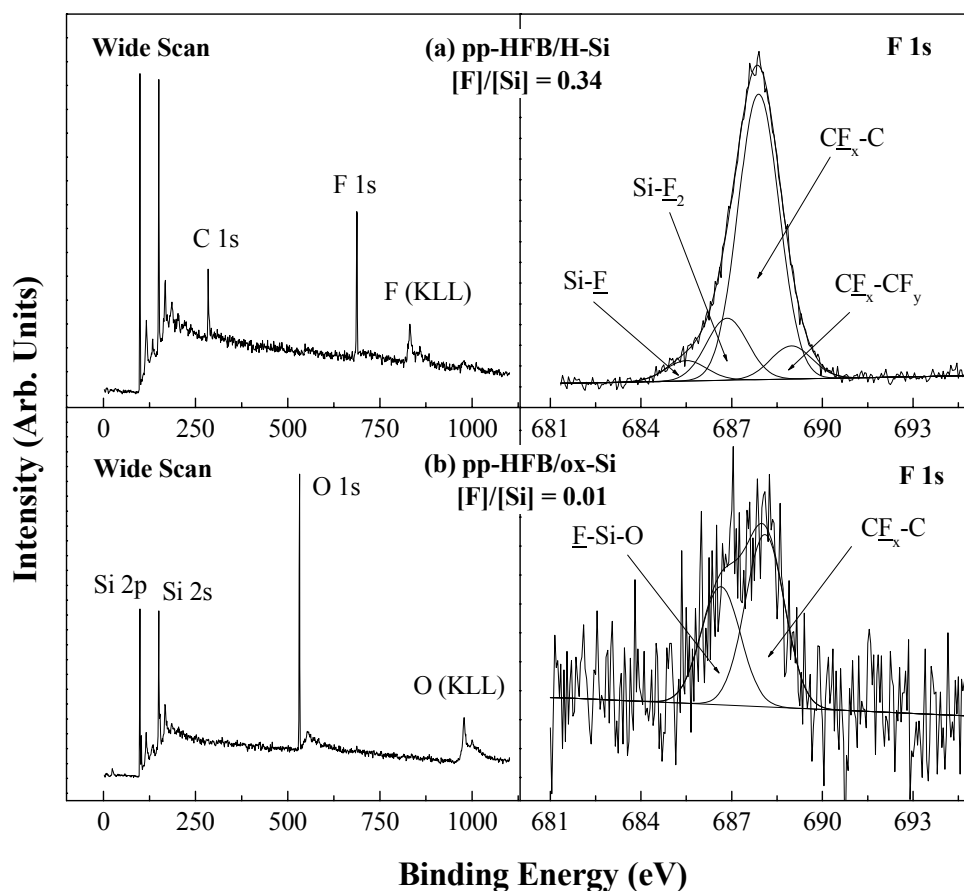


Figure 6.3 XPS wide scan and F 1s core-level spectra of (a) the ultra-thin pp-HFB/H-Si interface and the (b) ultra-thin pp-HFB/ox-Si interface.

However, a very weak F 1s signal was observed for the pp-HFB/ox-Si interface. The F 1s core-level spectrum was curve-fitted by two peak components attributable to the F-Si-O species and the CF_x-C species. The corresponding [F]/[Si] ratio was only 0.01.

In addition to the aromatic fluoro-monomers, linear fluoro-monomers, including HDFD and PFH, were also plasma polymerized and deposited on the H-Si and ox-Si surface for systematic investigation of the interfaces between the plasma-deposited fluoropolymers and Si surfaces (both H-Si and ox-Si surface). Figure 6.4 shows the XPS wide scan and F 1s core-level spectra of interfaces between the ultra-thin pp-HDFD fluoropolymer films and the Si surfaces (H-Si surface in Figure 6.4(a) and ox-Si surface in Figure 6.4(b)). Prominent Si 2p, Si 2s, C 1s, and F 1s signals were observed in the wide scan spectrum of the pp-HDFD/H-Si interface. The corresponding F 1s core-level spectrum obtained by narrow-scan consists of three peak components, with BE's at about 685.4 eV for the Si-F species, at about 686.6 eV for the Si-F₂ species, and 688.5 eV for the CF_x-CF_y species. The [F]/[Si] ratio is about 0.8, and ([Si-F]+[Si-F₂])/[Si] ratio is about 0.11.

Whereas, the F 1s core-level spectrum of pp-HDFD/ox-Si interface can be curve-fitted with two peak components, with BE's at about 686.6 eV for the F-Si-O species and 688.5 eV for the CF_x-CF_y species. The [F]/[Si] and [F-Si-O]/[Si] ratios are 0.3 and 0.06, respectively. Both ratios are also lower than those of the pp-HDFD/H-Si interface.

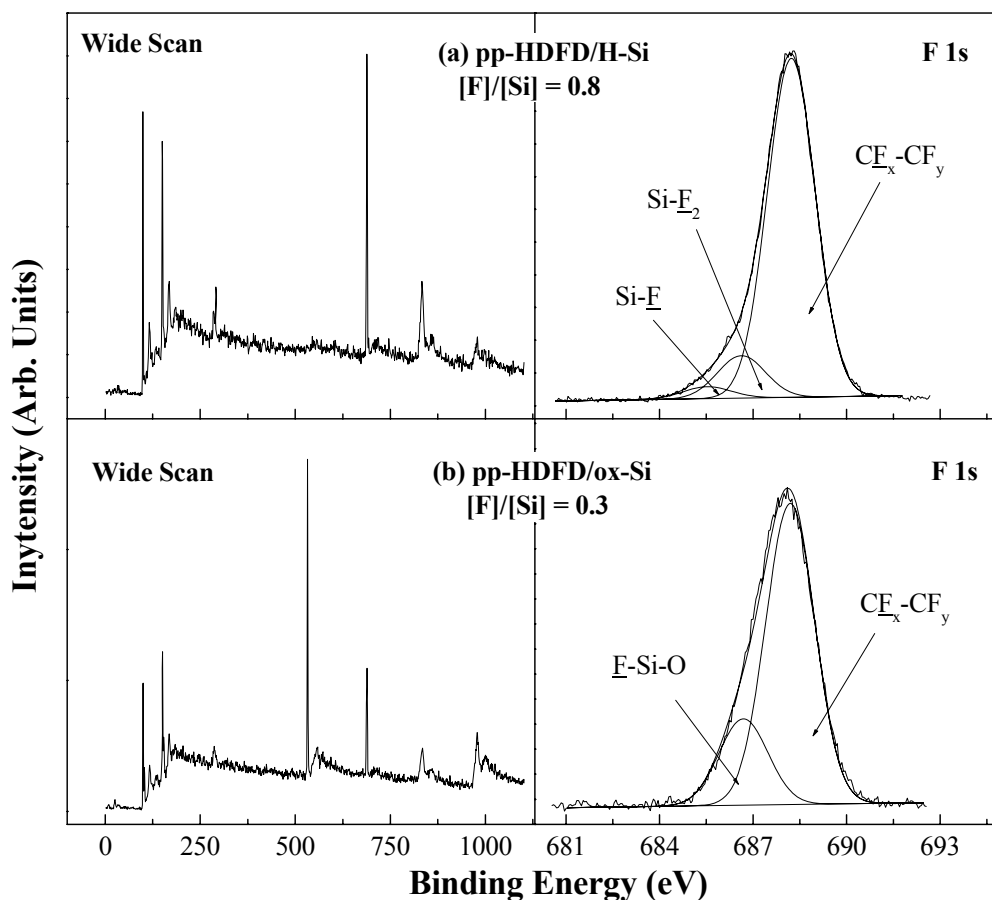


Figure 6.4 XPS wide scan and F 1s core-level spectra of (a) the ultra-thin pp-HDFD/H-Si interface and the (b) ultra-thin pp-HDFD/ox-Si interface.

Another linear and saturated fluoro-monomer, PFH, was also plasma polymerized and deposited on the Si surface. Figure 6.5 shows the wide scan and F 1s core-level spectra of the pp-PFH/H-Si (Figure 6.5(a)) and pp-PFH/ox-Si (Figure 6.5(b)) interfaces. As revealed by the curve-fitted F 1s core-level spectra, the chemical species involving fluorine atoms at the pp-PFH/H-Si interface are the same as those discerned for the pp-HDFD/H-Si interface, and the chemical species involving fluorine atoms at the pp-PFH/ox-Si interface are also the same as those for the pp-

HDFD/ox-Si interface. The $[F]/[Si]$ and $([F-Si]+[Si-F_2])/[Si]$ ratios for the pp-PFH/H-Si interface are 0.13 and 0.03, respectively. Whereas, $[Si]/[Si]$ and $[F-Si-O]/[Si]$ ratios for the pp-PFH/ox-Si interface are only 0.04 and 0.01, respectively.

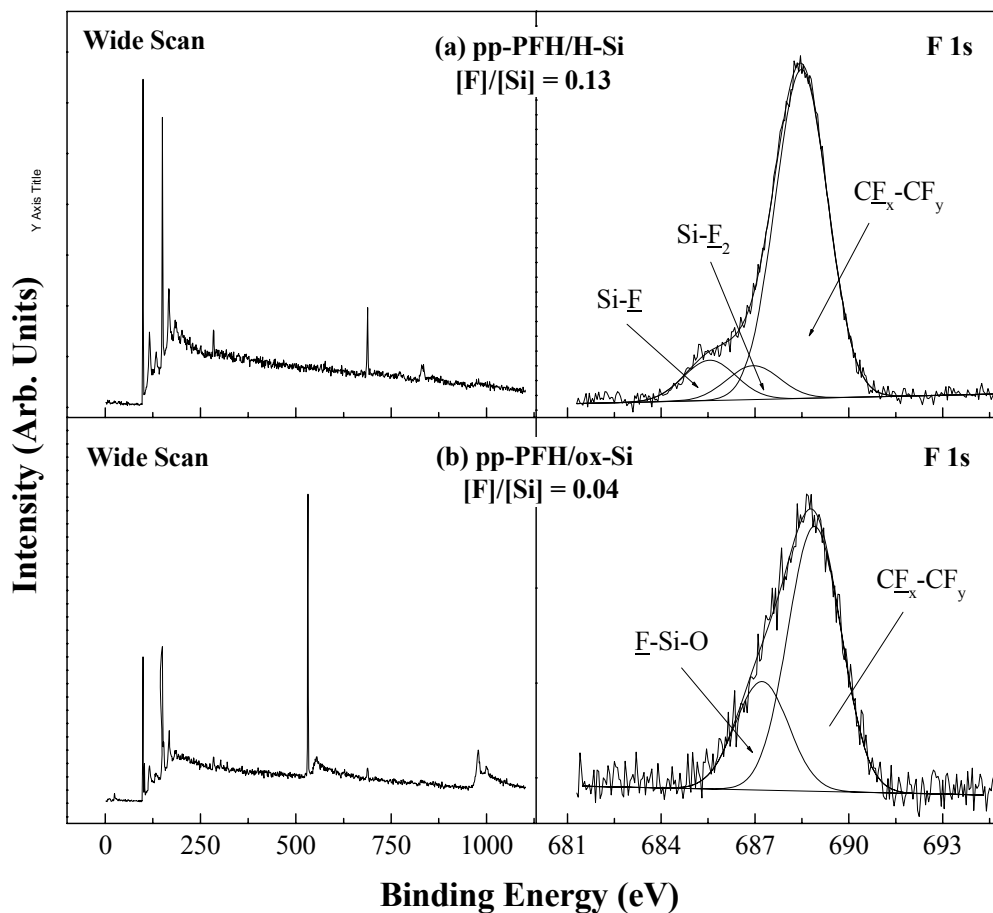


Figure 6.5 XPS wide scan and F 1s core-level spectra of (a) the ultra-thin pp-PFH/H-Si interface and the (b) ultra-thin pp-PFH/ox-Si interface.

As shown in Figure 6.2(a) and Figure 6.3(a), the F 1s core-level spectra of the pp-PFS/H-Si and pp-HFB/H-Si interfaces can be curve-fitted with four peak component and are dominated by the peak component with BE at about 687.7 eV for the CF_x-C

species. However, the F 1s core-level spectra of the pp-HDFD/H-Si and pp-PFH/H-Si interfaces shown in Figure 6.4(a) and 6.5(a), respectively, can only be curve-fitted with three peak components and are dominated by the peak component with BE at about 688.6 eV for the $\text{CF}_x\text{-CF}_y$ species. It is notable that PFS and HFB are aromatic fluoro-monomers, whereas, HDFD and PFH are linear fluoro-monomers. Thus, the peak component at about 687.7 eV for $\text{CF}_x\text{-C}$ species at the pp-PFS/H-Si and pp-HFB/H-Si interfaces is probably associated with the aromatic rings of the PFS and HFB, since the π electron cloud of the aromatic ring may shift to fluorine atoms and lead to the relatively lower BE, compared to the BE of the $\text{CF}_x\text{-CF}_y$ species formed by plasma polymerization and deposition of linear fluoro-monomer, HDFD and PFH, on the H-Si surface. The results also suggest that the aromatic ring of the PFS and HFB monomers could be preserved to a large extent during the plasma polymerization and deposition on H-Si surfaces presented here.

Figure 6.6 shows the Si 2p core-level spectra of the interfaces between the ultra-thin plasma-polymerized fluoropolymers and H-Si surfaces. The inset in Figure 6.6 shows the Si 2p core-level spectrum of the H-Si surface, which was curve-fitted with a spin-orbit-doublet with BEs at about 99.3 eV ($2p_{3/2}$) and 100 eV ($2p_{1/2}$) for the Si-Si species. After each ultra-thin fluoropolymer was plasma-deposited on the H-Si surface, an additional spin-orbit-doublet was observed at BEs of about 100 eV ($2p_{3/2}$) and 100.7 eV ($2p_{1/2}$) for the Si-C species (Flores et al., 2005 and Choi et al., 2005) (Figure 6.6(a-d)). The results suggest that Si-C bonds are formed at the interfaces between H-Si and ultra-thin films of pp-PFS, pp-HFB, pp-HDFD, and pp-PFH. Compared to the XPS Si

2p core-level spectrum of the ox-Si surface, However, no significant change of XPS Si 2p lineshape was observed for interfaces between the ox-Si surface and ultra-thin films of pp-PFS, pp-HFB, pp-HDFD, and pp-PFH (Figure 6.7(a-e)) after the plasma-deposition.

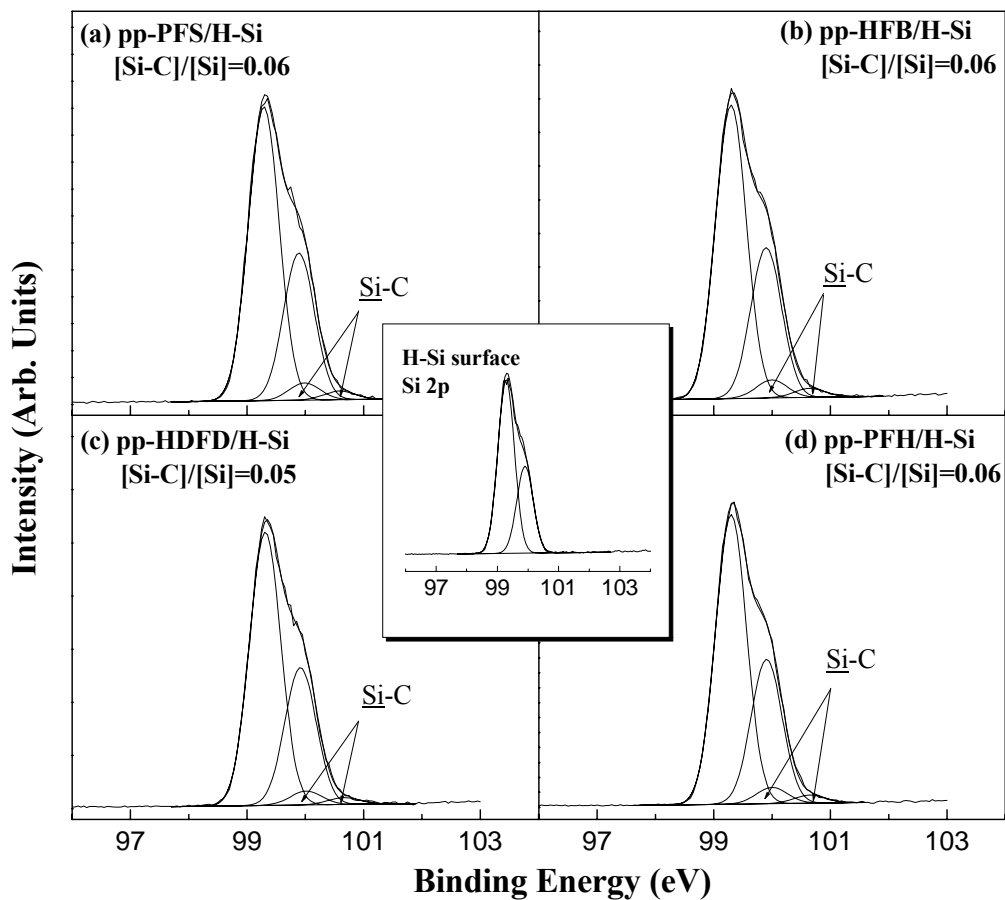


Figure 6.6 XPS Si 2p core-level spectra of (a) ultra-thin pp-PFS/H-Si interface, (b) ultra-thin pp-HFB/H-Si interface, (c) ultra-thin pp-HDFD/H-Si interface, and (d) ultra-thin pp-PFH/H-Si interface. The inset is the XPS Si 2p core-level of H-Si surface.

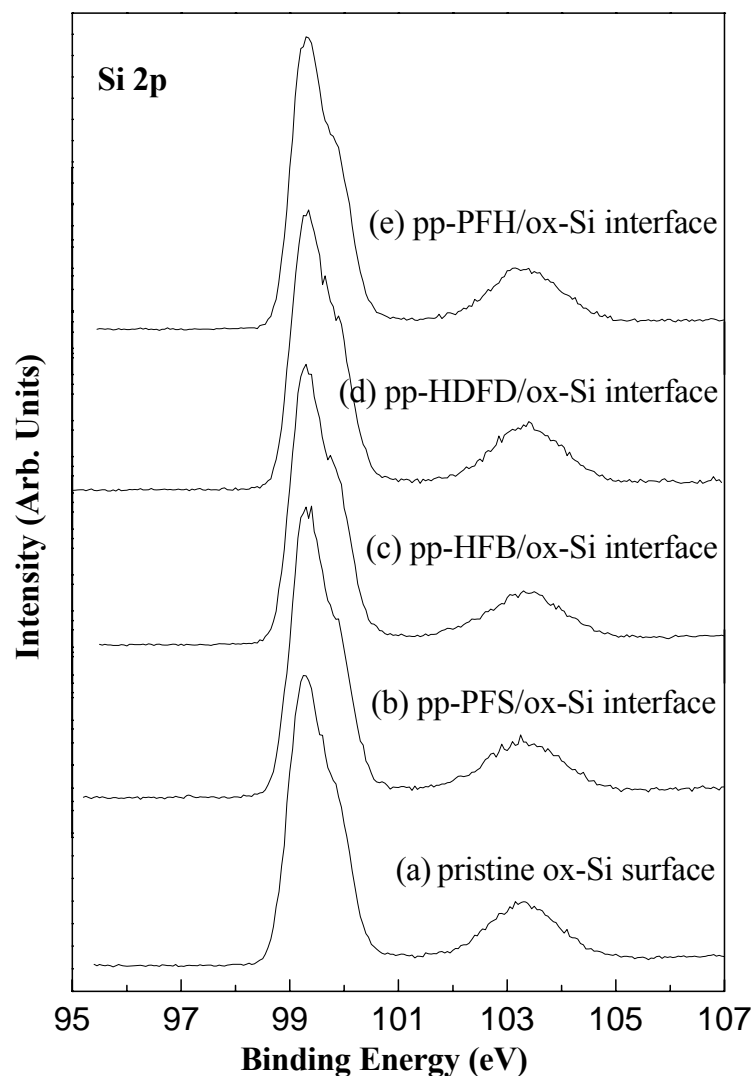


Figure 6.7 XPS Si 2p core-level spectra of (a) pristine ox-Si surface, (b) ultra-thin pp-PFS/ox-Si interface, (c) ultra-thin pp-HFB/ox-Si interface, (d) ultra-thin pp-HDFD/ox-Si interface, and (e) ultra-thin pp-PFH/ox-Si interface.

Etching of Si wafer by dilute aqueous HF solution generates a practically uniform H-Si surface (Higashi et al., 1990). However, these H-Si bonds on the Si surface are unstable to UV irradiation. Excitation of the H-Si bonds on the Si surface by UV light, such as that at 157 nm (Pusel et al., 1998; Vondrak et al., 1999), leads to the cleavage

of atomic hydrogen and formation the reactive sites (dangling bonds) on the surface. The photo-reactivity of the H-Si on the Si surface has been applied to covalently tether a monolayer layer of hydrocarbons through Si-C bonds on the Si surface by photo-induced reactions of unsaturated hydrocarbons with H-Si surface (Effenberger et al., 1998; Cicero et al., 2000).

In the present study, radicals were produced from fluoro-monomer during the plasma deposition process. In addition, H-Si bonds on the H-Si surfaces could be dissociated to generate the reactive sites (dangling bonds) on the Si surfaces by plasma-induced UV irradiation. Combined with the XPS results shown above, it was suggested that the radicals have higher reactivity on the original H-Si surface than that on the ox-Si surface during the plasma deposition, although ox-Si could be activated by electron and ion bombardment. The formation of the Si-C bonds at the interfaces between H-Si surface and plasma-polymerized fluoropolymer thin film could be attributed to the reaction between the reactive sites (dangling bonds) produced on the original H-Si surface by plasma-induced UV irradiation and radicals generated during the plasma deposition.

6.3.2 Chemical Structure of the Plasma-Deposited Fluoropolymer Films

The chemical structures of the fluoropolymer films deposited by plasma polymerization of the PFS, HFB, HDFD, and PFH monomers are investigated by FTIR spectroscopy and ToF-SIMS. The FTIR spectrum of the pp-PFS film is shown in Figure 6.8(a). The spectrum is dominated by the sharp and strong absorption bands

at 1500 and 971 cm^{-1} , associated with the fluorinated aromatic ring vibration and the CF phenyl ring stretching, respectively (Han et al., 1998). Thus, the presence of the fluorinated aromatic ring in the pp-PFS film is ascertained. In addition, the absorption band at 1650 cm^{-1} , assigned to the vinyl group, and the band in the region of 1100-1400 cm^{-1} , associated with the CF_x ($x = 1-3$) stretching mode (Yang et al, 2002) are also observed.

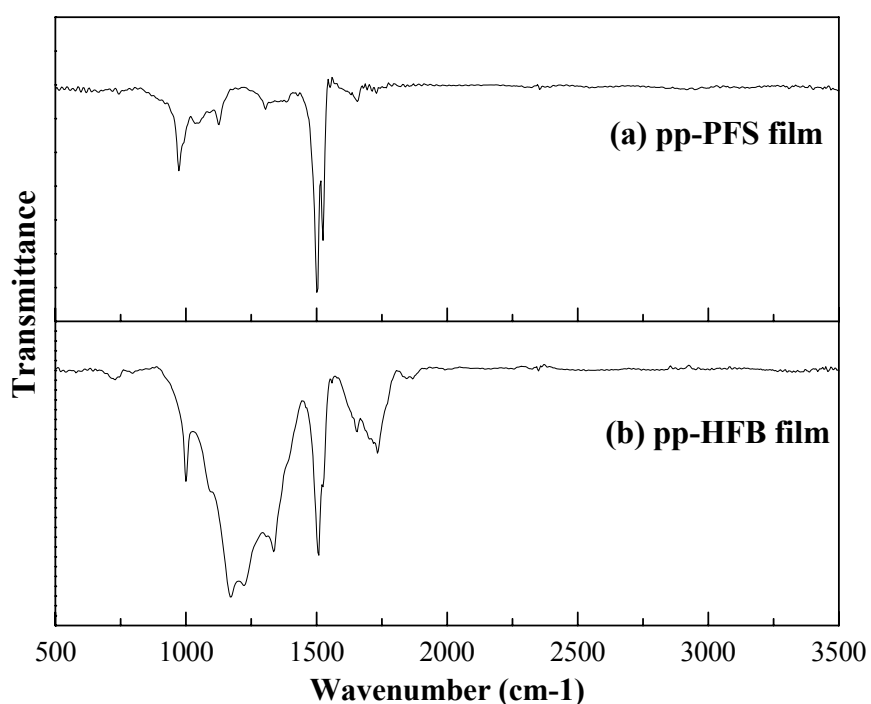


Figure 6.8 FTIR spectra of (a) the pp-PFS film and (b) the pp-HFB film

Figure 6.8(b) shows the FTIR spectrum of the pp-HFB film. The broad and strong band in the region of 1100-1400 cm^{-1} region is associated with the CF_x ($x = 1-3$) stretching, suggesting that extensive fragmentation has occurred during the plasma polymerization of HFB monomer. The presence of the absorption bands at 1507 and

998 cm^{-1} , arising from the fluorinated aromatic ring vibration and CF phenyl ring stretching, respectively, indicates the retention of a large proportion of the aromatic ring in the deposited film. Moreover, the bands at 1654 and 1730 cm^{-1} , corresponding to the C=C group and CF=CF stretching (Golub et al., 1998), are also observed.

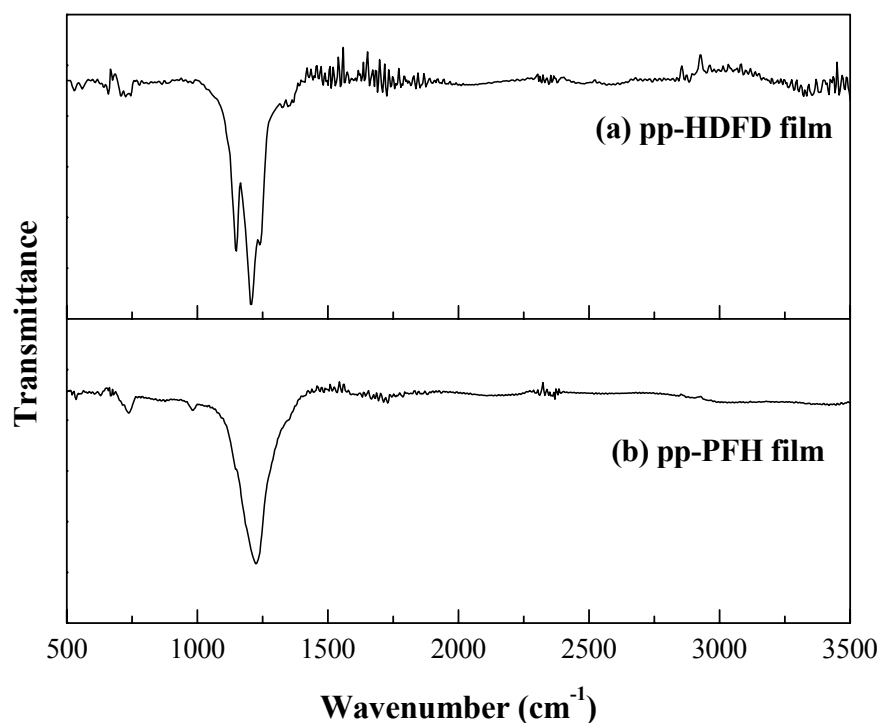


Figure 6.9 FTIR spectra of (a) the pp-HDFD film and (b) the pp-PFH film

The FTIR spectra of the pp-HDFD film and pp-PFH film are shown in Figure 6.9(a) and Figure 6.9(b), respectively. The pp-HDFD films shows characteristic absorption band of the CF_2 group at 658 cm^{-1} (CF_2 rocking), at 1149 cm^{-1} (asymmetric CF stretching) and at 1208 cm^{-1} (symmetric CF stretching). (Starkweather et al., 1985) A weak absorption band at about 740 cm^{-1} is assigned to CF_3 stretching deformation.

The spectra of pp-PFH film are dominated by the broad and strong CF₂ asymmetric stretching absorption band at 1226 cm⁻¹. The weak absorption bands at 737 and 983 cm⁻¹, associated with CF₂ and CF₃ groups, respectively, are also observed.

On the other hand, ToF-SIMS is also useful for the determination of the molecular structure of the polymers, such as the repeat units, the end groups and the oligomeric segments (Hanton et al., 2001; Briggs, 1998). Figure 6.10 shows the positive ion ToF-SIMS spectra of the pp-PFS film deposited on the H-Si surface. The assignments of the major mass fragments present in the spectra are given in Table 6.1. The peak of the highest intensity at $m/z = 195$ (C₄) indicates the dominance of the repeat unit of PFS in the pp-PFS film. The peak at $m/z = 361$ (C₈) suggests selective plasma polymerization through the vinyl groups. In addition, the presence of defluorination during the plasma polymerization, as suggested by the XPS results, is also indicated by the mass fragment at $m/z = 149$ (C₁) and $m/z = 161$ (C₂). Moreover, the peaks at $m/z = 205$ (C₅) and $m/z = 317$ (C₇) originated from the rearrangement and combination of fluorinated aromatic rings. The ToF-SIMS spectra of the pp-PFS film surface thus suggest that the fluorinated aromatic rings were preserved to a large extent and polymerization proceeded selectively through the vinyl groups. The positive ion ToF-SIMS spectrum of the pp-HFB film has been reported earlier (Yang, et al. 2002; Mackie et al., 1998). The TOF-SIMS results suggested that the aromatic rings were preserved to a large extent in the pp-HFB film during the plasma polymerization.

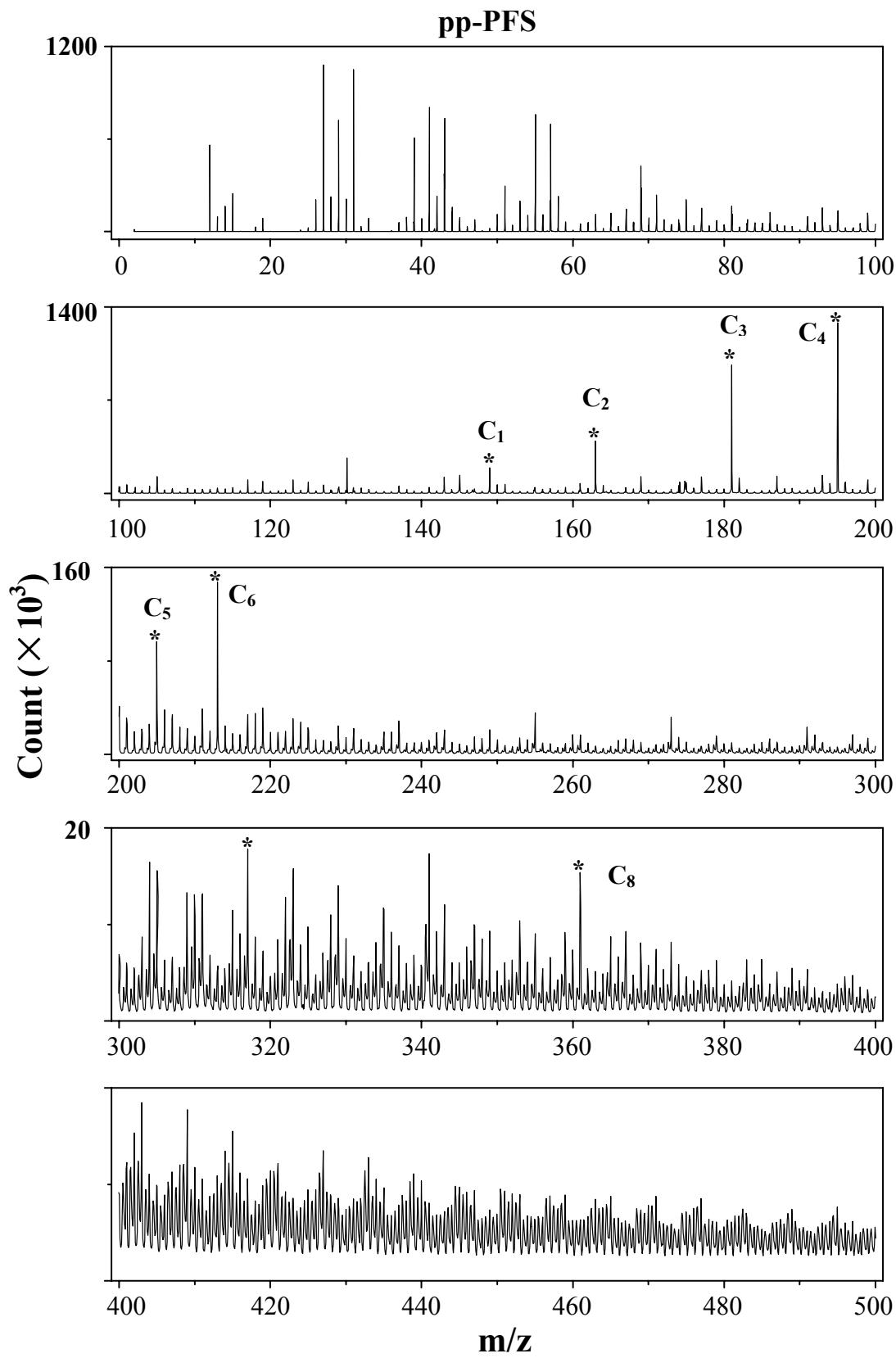
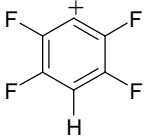
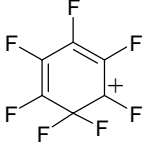
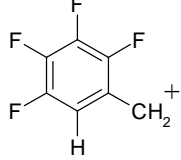
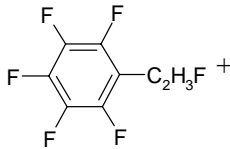
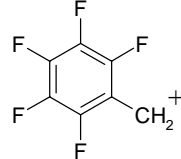
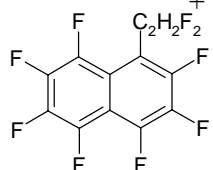
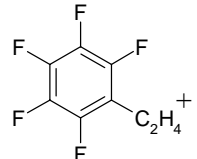
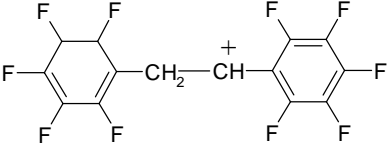


Figure 6.10 Positive ion ToF-SIMS spectra of the pp-PFS film on the H-Si surface

Table 6.1 Structural assignments of the mass fragments in the ToF-SIMS spectra of the pp-PFS film.

Peak (m/z)	assignment	Peak(m/z)	Assignment
C ₁ m/z = 149		C ₅ m/z = 205	
C ₂ m/z = 163		C ₆ m/z = 213	
C ₃ m/z = 181		C ₇ m/z = 317	
C ₄ m/z = 195		C ₈ m/z = 361	

The positive ion ToF-SIMS spectra of pp-HDFD and the assignments of some typical mass fragments are shown in Figure 6.11. The peaks at m/z of 853 and 871 in high mass region of the spectra are assigned to the mass fragments of $\text{CF}_3(\text{CF}_2)\text{-CH=C}^+$ - $(\text{CF}_2)\text{CF}_3$ and $\text{CF}_3(\text{CF}_2)\text{-CF=C}^+$ - $(\text{CF}_2)\text{CF}_3$, respectively. These fragments suggest the selective polymerization through vinyl groups and fluorinations of the vinyl groups during the plasma polymerization. The ToF-SIMS spectra of pp-HDFD film surface also readily indicated the preservation of the HDFD repeat units in the pp-HDFD film.

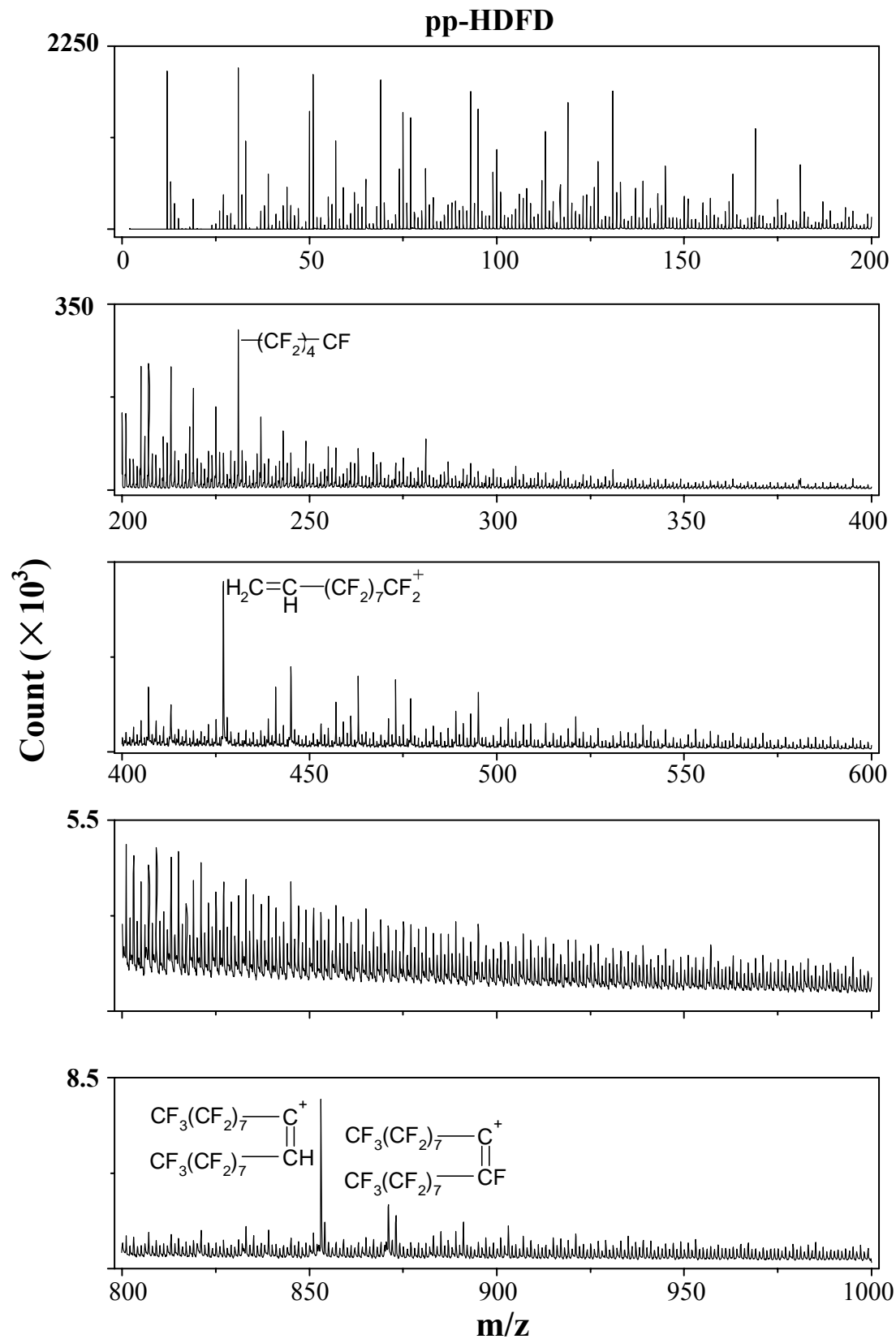


Figure 6.11 Positive ion ToF-SIMS spectra of the pp-HDFD film on the H-Si surface

The peaks with mass fragments at m/z of 445 and 427 are assigned to the $\text{CH}_2=\text{C}^+$ - $(\text{CF}_2)_7\text{CF}_3$ segments and $\text{CH}_2=\text{CH}-(\text{CF}_2)_7\text{CF}_2^+$, respectively. Other results of ToF-SIMS spectra of the pp-HDFD film, in addition to the positive ion ToF-SIMS spectra of pp-HFB and pp-PFH films, are same as the previous results (Yang et al., 2002; Zhang et al., 2002).

6.3.3 Surface Topography and Water Contact Angles of the Plasma-Deposited Fluoropolymer Films

Surface topography is of great importance to the application as dielectric materials. A uniform and defect-free surface is preferable in the planarization process. Figure 6.12 shows a typical AFM image of the H-Si surface. The H-Si surface is rather smooth and has a surface roughness (R_a) of about 0.21 nm.

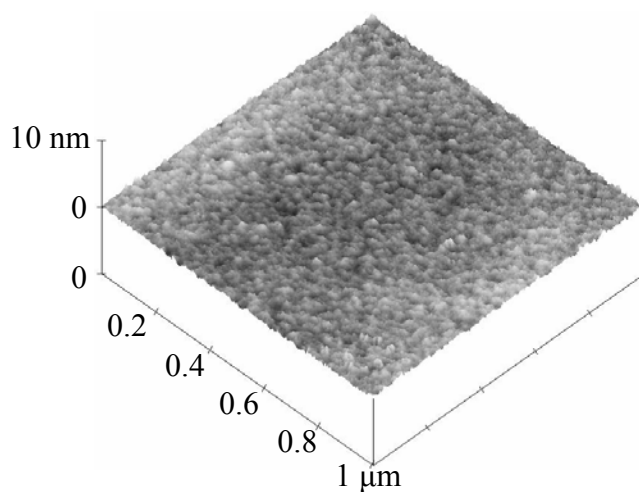


Figure 6.12 Typical AFM image of H-Si(100) surface

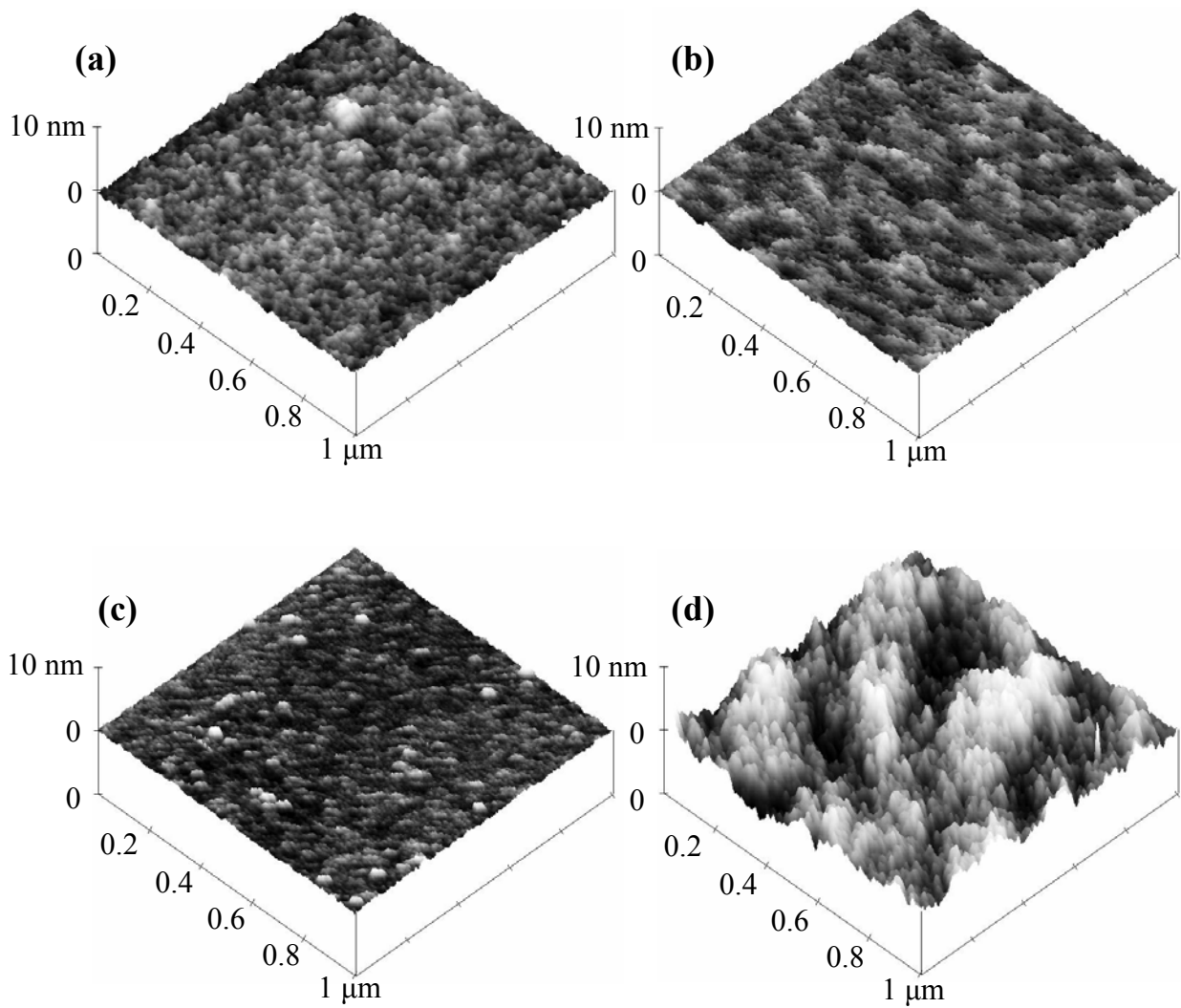


Figure 6.13 AFM images of the pp-PFS/H-Si surfaces with film thicknesses of (a) 2 nm and (b) 260 nm, and the pp-HFB/H-Si surfaces with film thicknesses of (c) 2 nm and (d) 530 nm.

Figure 6.13 shows the AFM images of the fluoropolymer films deposited on H-Si surfaces through plasma polymerization of the PFS and HFB monomers. After the deposition of the pp-PFS films (thickness ~ 2 nm in Figure 6.13(a) and ~ 260 nm Figure 6.13(b)) on H-Si surfaces, R_a values increase only marginally to 0.29 nm and

0.23 nm, indicating that the atomically smooth surface of H-Si is preserved after the deposition of the pp-PFS films. However, the surface of the thick pp-HFB film (~ 330 nm) shown in Figure 6.13(d) has an increased R_a value of 1.29 nm, despite of the fact that a rather smooth surface ($R_a = 0.19$ nm) is obtained for the pp-HFB film with a thickness of 2 nm (Figure 6.13(c)). These phenomena are probably associated with the higher rf power of 50 W applied to deposit the pp-HFB films. With the increase in rf power, the plasma polymerization transforms from an energy-deficient state to a more energetic state, leading to more excited species in the gas phase. As a result, polymerization occurs predominantly in the gas phase, yielding a deposited film with a rougher surface upon increasing the polymerization time (Teare et al., 2002; Inagaki et al., 1996).

Figure 6.14 shows the AFM images of ultra-thin and thick fluoropolymer film surfaces plasma deposited on H-Si surface from linear fluoro-monomers, HDFD and PFH. As shown by the surface roughness, all the surfaces are smooth and uniform in the nano-scale. The ultra-thin and thick pp-HDFD films deposited on H-Si surface have R_a values of 0.43 nm and 0.45 nm, respectively. The surface roughness only increase marginally, compared to original H-Si surface. In addition, AFM results suggest that the surface roughness of pp-HDFD films would not increase significantly as the film thickness of pp-HDFD increases. The ultra-thin and thick pp-PFH films plasma-deposited on the H-Si surfaces are also uniform in the nano-scale and have R_a values of 0.22 nm and 0.46 nm, respectively.

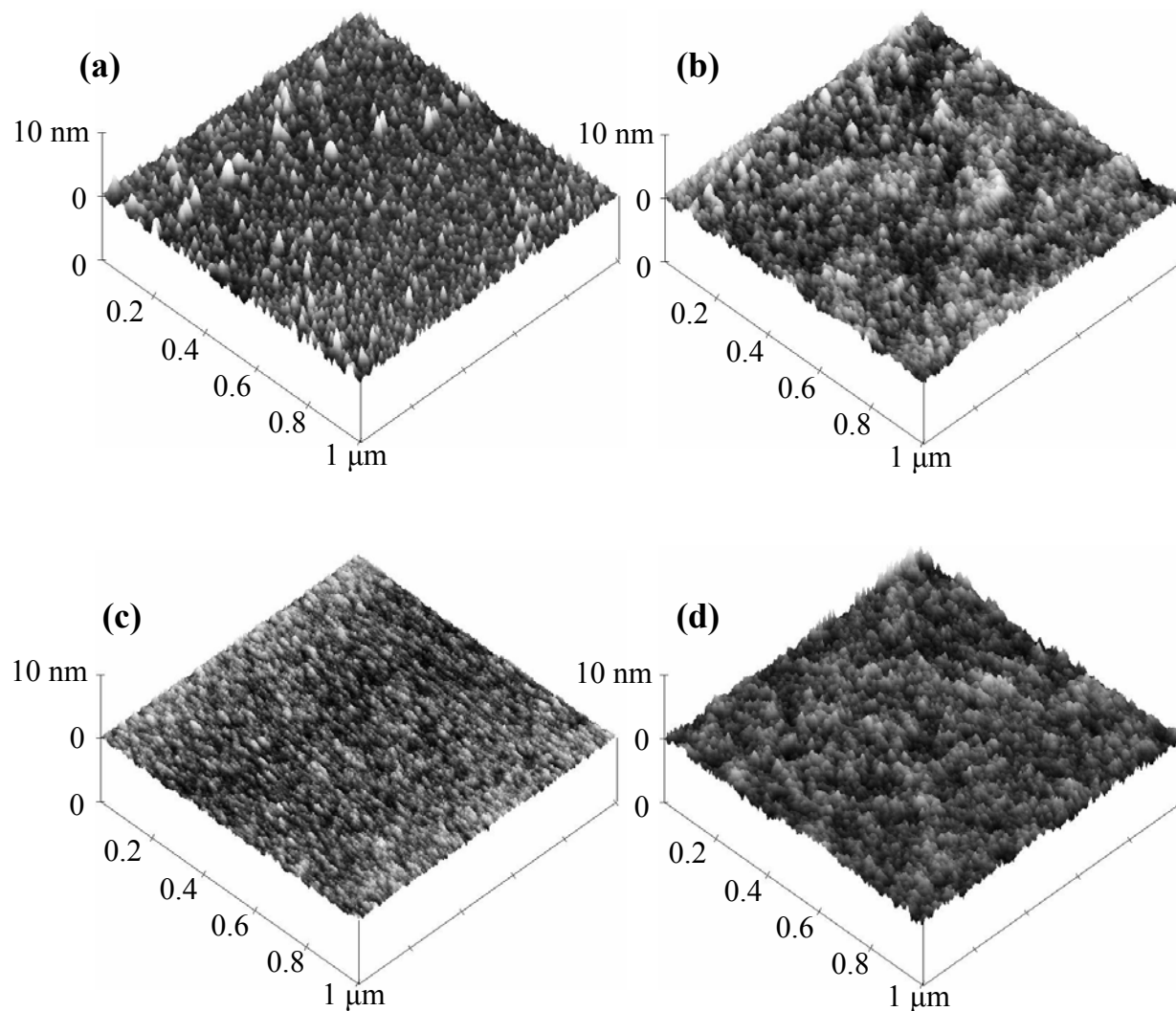


Figure 6.14 AFM images of the pp-HDFD/H-Si surfaces with film thicknesses of (a) 3.5 nm and (b) 460 nm, and pp-PFH/H-Si surfaces with film thicknesses of (c) 1.6nm and (d) 350 nm.

AFM analysis clearly shows that the plasma-deposited fluoropolymer films on H-Si surfaces are pinhole free and smooth in the nano-scale, except for the thick pp-HFB film on the H-Si surface which has an larger surface roughness ($R_a = 1.29$ nm) than all the other fluoropolymer films. The smoothness of the present polymer films is a remarkable contrast to the rough surface observed for the other high-power plasma-deposited fluoropolymer films (Yang et al., 2002; Zhang et al., 2002; Mackie et al.,

1998). A high plasma energy density will lead to the creation of a high concentration of condensable radicals, ion, and other species, as well as lowering the diffusion path lengths of these reactive species existing within the plasma (Yasuda, 1985). Under these conditions, gas-phase reactions between radical and other species are favored and rapid agglomeration is triggered, resulting in culmination of powder deposition onto the substrate surface. A low rf power was used for the plasma deposition of fluoropolymers on H-Si surfaces in the present work. The diffusion path length of radical and other species should be longer, lowering the probability for the reaction between radical and other species in the gas-phase. Under these conditions, direct deposition of radicals and other species on the Si surface would be favored and lead to the smooth fluoropolymer films on the H-Si surfaces.

Table 6.2 Thicknesses, water contact angles, and composition of the plasma-deposited fluoropolymers on H-Si(100) surfaces.

Sample	Thickness (nm)	Contact angle, θ (degree)	[F]/[Si] Ratio ^{c)}	[F]/[C] Ratio ^{c)}
pp-PFS ^{a)}	~ 2	~ 98	0.18	0.42
	~ 260	~ 105	—	0.62
pp-HFB ^{b)}	~ 2	~ 86	0.34	0.62
	~ 330	~ 95	—	1.07
pp-HDFD ^{a)}	~ 3.5	~ 99	0.80	1.25
	~ 460	~ 116	—	1.75
pp-PFH ^{b)}	~ 1.6	~ 95	0.13	0.30
	~ 350	~ 120	—	2.09

a) Plasma polymerization and deposition of PFS on H-Si surfaces (15 W, 200 mTorr, 30 sccm)

b) Plasma polymerization and deposition of HFB on H-Si surfaces (50 W, 200 m Torr, 30 sccm)

c) [F]/[Si] and [F]/[C] are atomic concentration ratios from XPS

The static water contact angles are listed in Table 6.2. For ultra-thin pp-PFS and pp-HFB films, the water contact angles are 98° and 86°, respectively. With the increase in thickness, (260 nm for the pp-PFS and 330 nm for the pp-HFB films), the water contact angle increase to 105° and 98°. At the same time, the corresponding [F]/[C] ratios of the pp-PFS and pp-HFB films also increase from 0.42 and 0.63 to 0.62 and 1.07, respectively. The increases in the [F]/[C] ratios and the surface roughness (for the pp-HFB film) probably have given rise to the increased water contact angles. In addition, the water contact angles of the thick pp-HDFD and pp-PFH films are higher than those of the thick pp-PFS and pp-HFB films. The phenomenon is probably due to the higher [F]/[C] ratios in the thick pp-HDFD and pp-PFH films.

6.3.4 Adhesion Characteristics of the Plasma-Deposited Fluoropolymer Films with the H-Si Surface.

The adhesive characteristic of the plasma-deposited fluoropolymer films with the H-Si surface were evaluated by the 180°-peel adhesion test. Copper foil adhesive tapes were applied to the thick pp-PFS (~ 260 nm), pp-HFB (~ 330 nm), pp-HDFD (~ 460 nm), and pp-PFH (~ 350nm) films deposited on the H-Si substrates, and subsequently peeled off on a tensile tester. Both the delaminated fluoropolymer surfaces and copper tape surfaces were analyzed by XPS. The copper tape/fluoropolymer laminates have 180°-peel adhesion strength of about 3.0-3.2 N/cm. The respective wide scan spectra of the delaminated fluoropolymer film and copper tape surfaces are shown in Figure 6.15. No Si 2p signal was discernable for the fluoropolymer films deposited on the delaminated H-Si surfaces. In addition, the F 1s signal is also absent in the wide scan

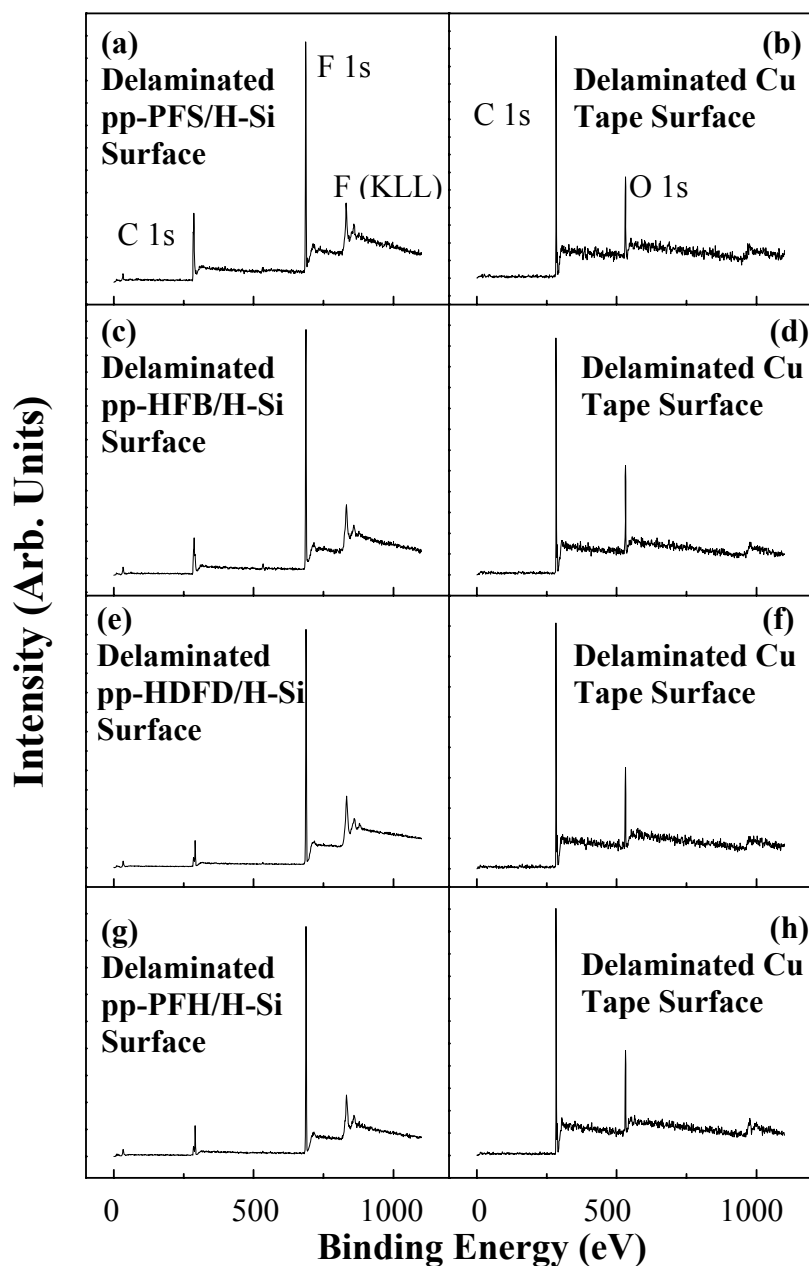


Figure 6.15 XPS wide scan spectra of (a) the delaminated pp-PFS/H-Si(100) surface, (b) the delaminated Cu tape surface from the Cu tape/pp-PFS/H-Si(100) assembly, (c) the delaminated pp-HFB/H-Si(100) surface, (d) the delaminated Cu tape surface from the Cu tape/pp-HFB/H-Si(100) assembly, (e) the delaminated pp-HDFD/H-Si(100) surface, (f) the delaminated Cu tape surface from the Cu tape/pp-HDFD/H-Si(100) assembly, and (g) the delaminated pp-PFH/H-Si(100) surface, (h) the delaminated Cu tape surface from the Cu tape/pp-PFH/H-Si(100) assembly

spectra of the copper tape surfaces delaminated from the different fluoropolymer surfaces. These observations readily suggest that all the copper tape/fluoropolymer film assemblies have delaminated by adhesion failure at the interfaces between the copper adhesive tape and the fluoropolymer film deposited on the H-Si surface. Thus, all the plasma-deposited fluoropolymer films are strongly bonded to the H-Si surfaces. Through UV cleavage of the H-Si bonds on the H-Si surface, dangling bonds were formed and reacted readily with the monomer fragments or radical during the plasma polymerization and deposition process. In addition, low rf power has been used for the plasma polymerization. The probable long diffusion path length also facilitates the radicals and other species to deposit directly on the Si surface and to covalently bond with the dangling bonds on the Si surface. All these factors have contributed to the strong adhesion between the plasma-deposited fluoropolymer and Si substrate.

6.4 Conclusions

Fluoropolymer films were deposited on the hydrogen-terminated (H-Si) and native oxide-covered silicon (ox-Si) surface by plasma polymerizations of pentafluorostyrene (PFS), hexafluorobenzene (HFB), heptafluoro-1-decene (HDFD), and perfluoroheptane (PFH). The chemical states at the fluoropolymer/H-Si and fluoropolymer/ox-Si interfaces were investigated by XPS. The XPS results revealed the formation of F-Si bonds and Si-C bonds at the interface, which were formed through the interaction of the activated molecular fragments or radicals with the dangling bonds on the silicon surfaces during the plasma polymerization process. Consequently, the plasma-deposited fluoropolymer films were strongly bonded to the H-Si surfaces. The preservation of the fluorinated aromatic rings in the pp-PFS and pp-HFB films were suggested by FTIR results. In addition, ToF-SIMS results suggested selective polymerization of the PFS monomer through the vinyl group. The plasma-deposited fluoropolymer films exhibited hydrophobic surfaces.

Chapter 7

Chemical States and Electronic Properties of the Interface Between Aluminium and a Photoluminescent Conjugated Copolymer Containing Europium Complex

7.1 Introduction

Conjugated polymers are promising materials for photonic applications due to their high fluorescence efficiencies, a wide range of emitting wavelengths, and mechanically flexibility (Hide et al., 1997). Since the fabrication of polymer light-emitting diodes (PLEDs) in 1990 (Burroughes et al., 1990), there has been extensive research on PLEDs and significant progress has been made (Brown et al., 1992; Cao et al., 1999). Although many conjugated polymers have high photoluminescence (PL) efficiencies (>50%), the electroluminescence (EL) efficiencies of the devices based on these polymers are usually low (<5%). This low EL efficiency is associated with the formation of triplet excitons in PLEDs. Theoretically, only 25% of the excitons in conjugated molecules have the singlet character. Thus, the quantum efficiency of a conjugated polymer can not exceed 25% (Baldo et al., 2000). In addition, obtaining pure color emission from conjugated polymers or small organic molecules is difficult because their emission spectra typically have a full width at half maximum (FWHM) of 50-200 nm (Hide et al., 1997), arising from the inhomogeneous broadening and the presence of vibronic progression. Recent study of EL from organic triplet excitons has opened the way to very high efficiency organic light emitting diodes (OLEDs) (Baldo et al., 1998; Kido et al., 2002). In addition to the well known porphyrin platinum and 2-phenypyridine derivatives of the iridium complexes (Baldo et al., 1998 and 1999), the rare earth complexes are expected to have high emission efficiency, along with a narrow emission spectrum. Nevertheless, most of the light emitting diodes (LEDs) based on rare earth complexes exhibit unfavorably high turn-on voltages (>20 V) (Kido et al., 2002). One factor influencing the turn-on voltage in organic LEDs is

associated with the carrier injection barrier at the interfaces (Baldo et al., 2001). Thus, elucidation of the chemical states and electronic properties of the metal/rare earth complex interface is important for understanding and improving the performance of organic LEDs.

ITO-organic and metal-organic interfaces still attract considerable attention because of the important role of the organic LEDs and thin film transistor. The performance of these devices is directly related to the energy barrier for carrier injection. The energy barrier is defined as the energy difference between the Fermi level of the metal and the highest occupied molecular orbital (HOMO) or the lowest unoccupied molecular orbital (LUMO) of the organic materials. For example, experimental and theoretical investigations of the interfaces between Alq₃ film and low work function metals (Mg, Al, Li, K and Ca) have revealed strong metal-molecule interactions, which affect the carrier injection process.

In this Chapter, XPS and ultraviolet photoelectron spectroscopy (UPS) are used to study *in situ* the chemical states and electronic properties of the interface between aluminium, a widely used cathodic metal in organic LEDs due to its low work function, and the conjugated copolymer (PF6-Eu(dbm)₂phen) containing 9,9'-dihexylfluorene and europium complex-chelated benzoate units in the main chain. The copolymer complex is a novel pure red-light emitter. Understanding the interface between a low work function electrode, such as aluminium, and conjugated copolymer

PF6-Eu(dbm)₂phen will have direct relevance to the fabrication of high performance PLEDs.

7.2 Experimental

7.2.1 Sample preparation

The synthetic route for the conjugated copolymer containing 9,9'-diethylhexylfluorene (PF6) and europium complex-chelated benzoate units in the main chain involved three steps: 1) a copolymer of 2,7-bis(trimethylene boronate)-9,9'-diethylhexylfluorene and methyl 3,5-dibromobenzoate was synthesized through using palladium catalyst (Suzuki coupling reaction) (Miyaura et al., 1995), 2) the copolymer was then hydrolyzed to provide the active carboxylic ligands in the main chain (Kaeriyama et al., 1995), and 3) the polymeric ligands, together with dibenzoylmethane (dbm) and 1,10-phenanthroline (phen), chelated the highly reactive europium triisopropoxide (Sinha, 1960) to form the desirable copolymer complex. The resulting copolymer complex, PF6-Eu(dbm)₂phen, is readily soluble in toluene, chloroform and THF, and can be cast into transparent films with high mechanical flexibility. The europium triisopropoxide (Sinha, 1960), palladium catalyst (Coulson et al., 1972), and other monomer were prepared according to procedures described in the literature (Zhan et al., 2001).

The copolymer had a number average molecular weight (M_n) of 41,100, with a polydispersity (M_w/M_n) of 2.58. The chemical structure and properties of the copolymer were characterized by FT-IR, ¹H NMR, ¹³C NMR, TGA, DSC and ToF-SIMS (Ling et al., 2003). The chemical structure of PF6-Eu(dbm)₂phen is shown in Figure 7.1. PF6-Eu(dbm)₂phen films of about 100 nm in thickness were spin-casted

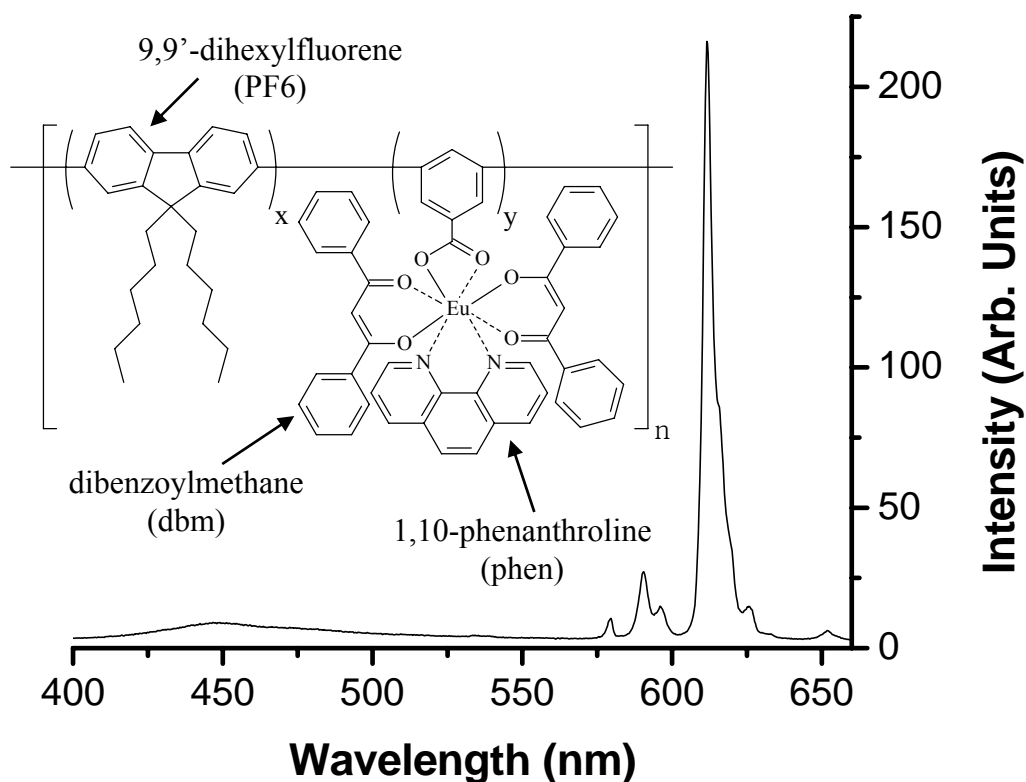
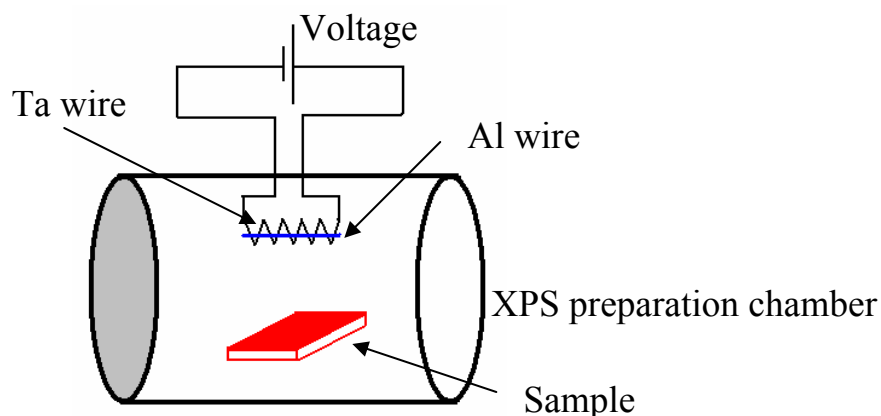


Figure 7.1 Chemical Structure PF6-Eu(dbm)₂phen and the emission spectrum of the PF6-Eu(dbm)₂phen film

from the toluene solution (10 mg/ml) on glass substrates. The solvent was removed by pumping under reduced pressure at room temperature for 48 h. Figure 7.1 also shows the photoluminescent spectrum of the copolymer film. Using an excitation wavelength of 350 nm, nearly monochromatic red emission spectrum, with a line width (full width at half maximum or FWHM) of 4 nm, was obtained. Effective intramolecular energy transfer from the fluorene to the Eu complex has given rise to the nearly monochromatic red emission in this soluble conjugated copolymer.

7.2.2 Metal evaporation



The thermal deposition of aluminium was performed using an evaporator installed inside the XPS preparation chamber, which was connected to the XPS analysis chamber via a gate valve. The evaporator filament was made of tantalum wire (99.9% purity, 0.25 mm in diameter), obtained from Goodfellow Inc., Cambridge, UK. High-purity Al wire segments (diameter = 0.25 mm, purity = 99.9%, also from Goodfellow Inc.), were attached to the filament for evaporation. Under the high-vacuum condition, the aluminium vapor was deposited *in situ* onto the surface of the PF6-Eu(dbm)₂phen film in the XPS preparation chamber in a stepwise manner, permitting the analysis without exposure to the atmosphere. The rate of deposition was controlled by the electrical current supply to the filament. Prior to evaporation, the aluminium and the filament were continuously outgassed by heating at 2.2 A. The evaporation of aluminium was then carried out at a current of 5.0 A. The amount of the metal deposited was controlled by the evaporation time. Each round of evaporation was carefully controlled in order to avoid over-exposure. The sample was transferred into the XPS analysis chamber for surface and interface analysis after every round of evaporation.

7.2.3 Surface and interface characterization

The XPS and UPS measurements were performed on a Kratos AXIS HSI spectrometer, using the monochromatized Al K α X-ray source (1486.7 eV) and the He I (21.2 eV) radiation, respectively. The X-ray source was run at a reduced power of 150 W (15 kV with an emission current of 10 mA) to minimize possible damage to the polymer films. The operating pressure in the analysis chamber was maintained at 8.0×10^{-9} Torr or lower during every measurement. The spectra at photoelectron take-off angles (α) of 20° and 90° were recorded after each round of evaporation. In peak synthesis, the linewidth of the Gaussian peaks were kept constant for all components in a particular spectrum. To compensate for surface charging effect, all binding energies (BE's) were referred to the neutral hydrocarbon C 1s peak at 284.6 eV. Surface elemental stoichiometries were determined from peak-area ratios after correcting with the experimentally determined sensitivity factors, and were reliable to within $\pm 10\%$. The sensitivity factors were calibrated using stable binary compounds of well-defined stoichiometries.

7.3 Results and Discussion

7.3.1 Evolution of the C 1s core-level spectra upon Al deposition

The evolution of the C 1s core-level spectra of the copolymer upon Al deposition, obtained at the photoelectron take-off angle (α) of 90° , is shown in Figure 7.2. For the pristine PF6-Eu(dbm)₂phen surface (Figure 7.2a), the C 1s spectrum consists of a main peak component at the binding energy (BE) of 284.6 eV and two minor ones at the BE's of 285.8 eV and 286.6 eV. The main C 1s peak component is assigned to the C-C and C-H species (including both the aliphatic carbon atoms of the side chain and the aromatic carbon atoms not bonded to the heteroatoms in the conjugated system) (Nguyen, 1993 and 1995). The peak component at 285.8 eV is assigned to carbon atoms bonded to the heteroatoms (O and N) in the conjugated system (Figure 7.1) (Beamson et al., 1992). The peak component at 286.6 eV, on the other hand, is assigned to the carbon atoms of the carboxylic group bonded to the europium ion. Compared to the BE of 289.2 eV for the carboxyl carbon atoms of poly(acrylic acid) (Zhan et al., 2001), the BE of 286.6 eV observed for the copolymer suggests electron transfer from Eu to oxygen atoms, leading to a lower electron withdrawing effect of the oxygen atoms on the carbon atom of the carboxylic group in the Eu-complex. The C 1s peak components for the pristine polymer surface have a FWHM of 1.1 eV.

The C 1s spectral lineshape of the PF6-Eu(dbm)₂phen surface changes progressively upon Al deposition. A tail appeared on the lower BE side of the main peak component. Upon further examination of the changes by peak synthesis, a new C 1s peak component at the BE of 283.4 eV is discernible (Figure 7.2(b)-7.2(d)). This low-BE

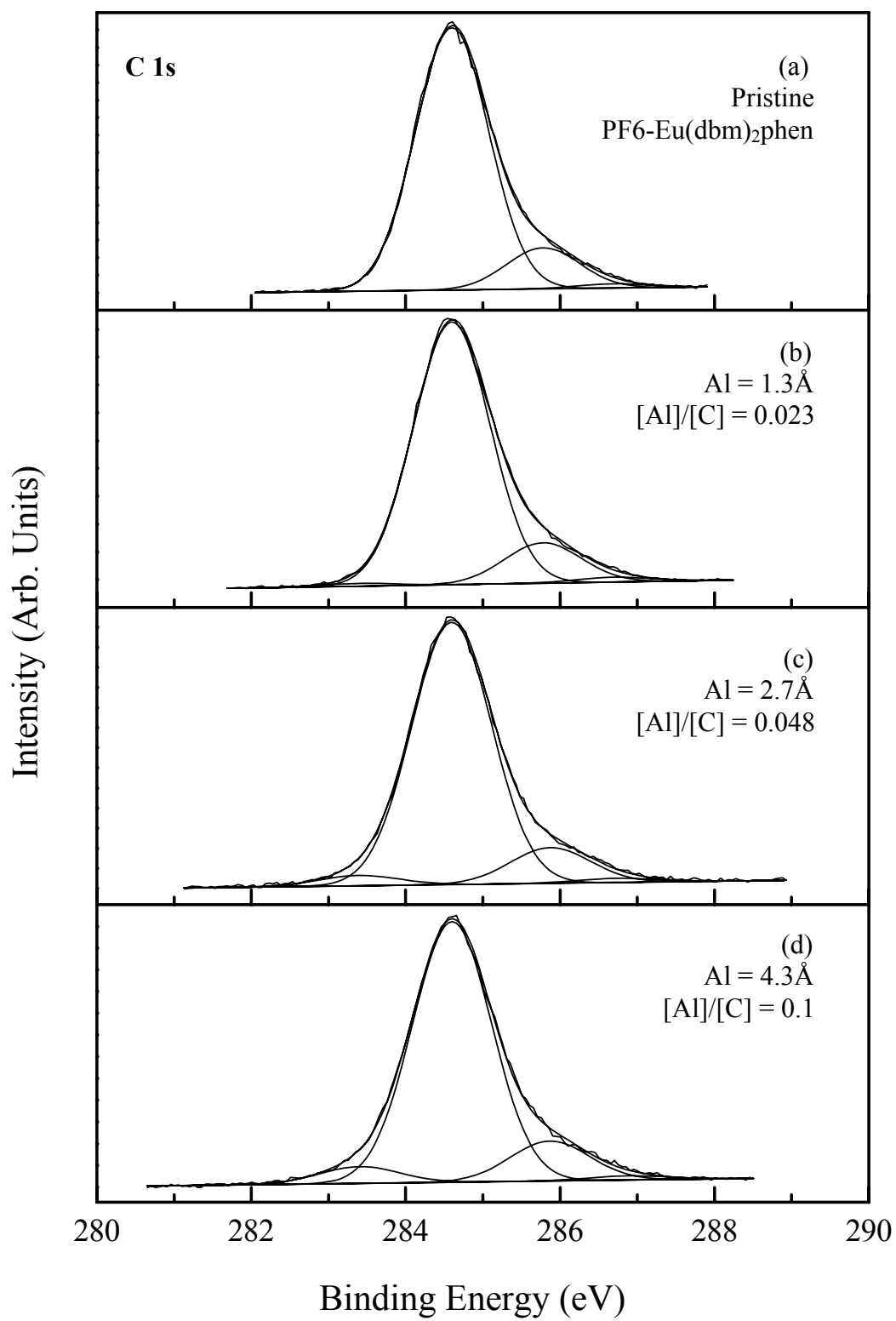


Figure 7.2 (a-d) Evolution of the C 1s core-level spectra as a function of Al coverage ($\alpha = 90^\circ$)

peak component corresponds to the formation of aluminium carbide species at the interface, as a consequence of the interaction of aluminium atoms with the carbon atoms. The formation of aluminium carbides, arising from electron transfer from aluminium to carbon atoms, have been widely observed in other Al/polymer interfaces (Kang et al., 1997; Dannetun et al., 1993). For the Al/ α -sexithiophene interface, a low-BE shoulder, attributable to the metal carbide species, appeared in the C 1s core-level spectrum immediately after Al was deposited on α -sexithiophene. However, for the Al/poly-3-octylthiophene and Al/polyethylene interfaces, the C 1s core-level spectra of the polymers were not affected, suggesting that only weak interactions exist between the Al atoms and the carbon atoms of the polymers. It was concluded that Al atoms tend to interact more strongly with carbon atoms in the conjugated system than with the aliphatic carbon atoms (Dannetun et al., 1993). Therefore, the aluminium atoms probably have reacted preferentially with the conjugated carbon atoms, over the aliphatic carbon atoms, in the present PF6-Eu(dbm)₂phen copolymer complex. In addition, the intensity of the low-BE C 1s peak component became stronger with progressive aluminium deposition. This phenomenon is consistent with the fact that the subsequent electron transfer is not to the same carbon atom in the conjugated system, because transfer of this nature will cause a further negative shift in BE rather than an increase in proportion of the same low-BE species. This observation also suggests that the aluminium atoms have been uniformly deposited on the surface of the polymer film. In devices fabrication, the electron transfer from aluminium atoms to polymer at the surface could increase the electron injection barrier, and a higher turn-on voltage could be expected. Moreover, the electroluminescent character of the

polymer probably will also be affected by the formation of Al complexes at the interface.

It is well established that photoelectrons of 1200 eV in energy, such as the C 1s photoelectrons collected using the Al K α X-ray source, have an inelastic mean free path of $\sim 29 \text{ \AA}$ in an organic layer (Briggs, 1998). Thus, 95% of the C1s photoelectron intensity originates from the top $\sim 87 \text{ \AA}$ layer of the sample. For the submonolayer, or the first few monolayers, of aluminium atoms deposited at the surface, the C 1s signal is contributed predominately by the underlying polymer. Therefore, the thicknesses of aluminium after each deposition process can be estimated by assuming that the attenuation of the C 1s photoelectron signal obeys the Beer-Lambert Law. The estimated thickness of aluminium after each deposition process is also included in Figure 7.4.

7.3.2 Interaction of Al with the heteratoms of PF6-Eu(dbm)₂phen

The Eu 3d core-level spectra, obtained at $\alpha = 90^\circ$, for the pristine PF6-Eu(dbm)₂phen film and the Al/PF6-Eu(dbm)₂phen interface after each aluminium deposition are shown in Figure 7.3. For the pristine PF6-Eu(dbm)₂phen surface, the doublet with the Eu 3d_{3/2} and Eu 3d_{5/2} peak components at the BE's of 1165.4 eV and 1135.4 eV, respectively, (Figure 7.3(a)) is assigned to the Eu(III) species (Uwamino et al., 1984). By taking into account of the carbon species associated with the two high BE C 1s peak components at 285.8 eV and 286.6 eV, the Eu 3d core-level spectrum of the pristine film confirms the interaction of the Eu atom with the oxygen atoms of dbm

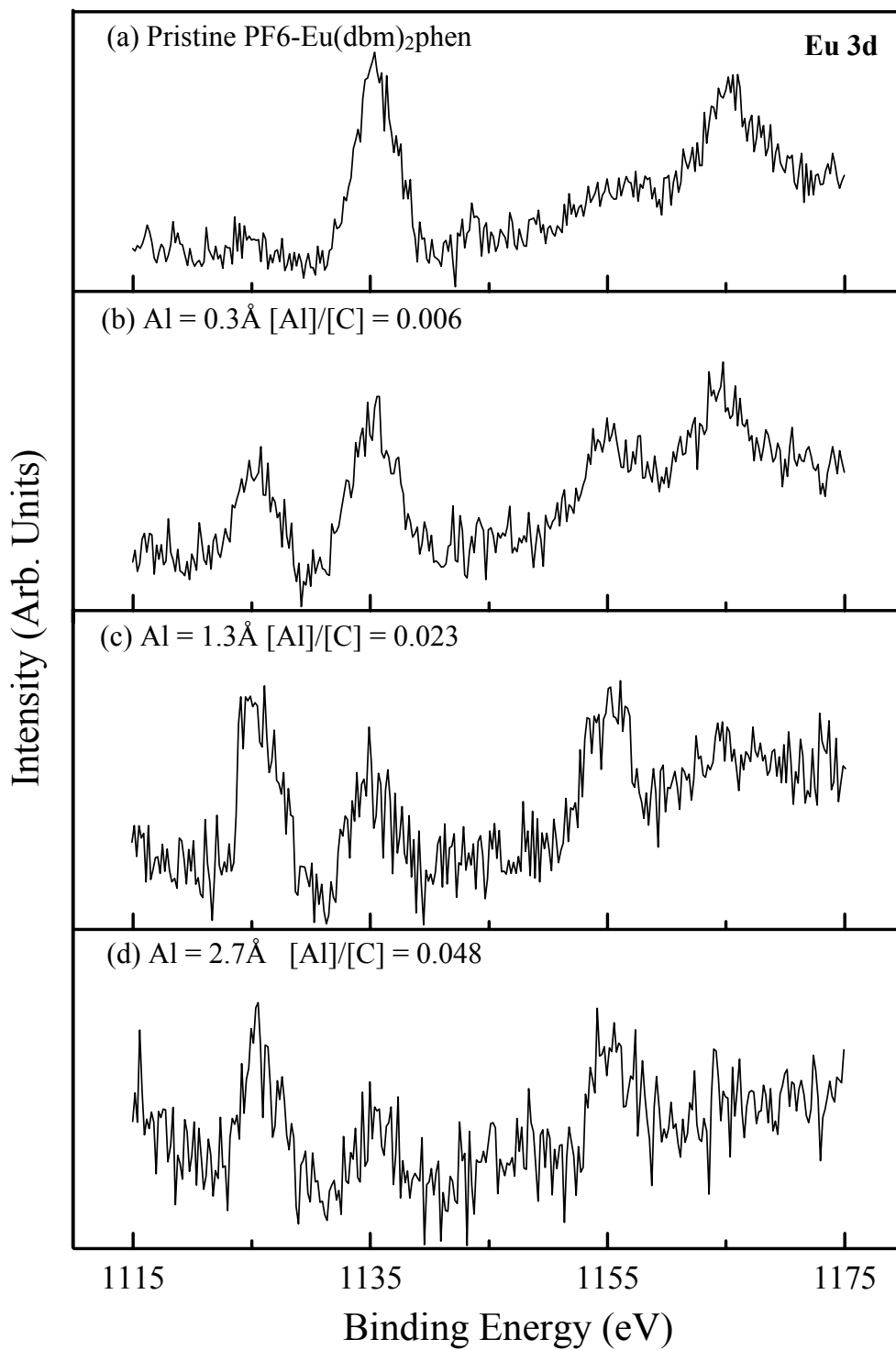


Figure 7.3 Evolution of the Eu 3d core-level spectra as a function of Al coverage ($\alpha = 90^\circ$).

and carboxyl ligand of the copolymer. After the first aluminium deposition process ($[Al]/[C] = 0.006$, 0.3 \AA), a new doublet with the BE's for the Eu $3d_{3/2}$ and Eu $3d_{5/2}$ peak components at 1155.4 eV and 1125.4 eV, respectively, attributable to the neutral europium atoms (Thole et al., 1985), has appeared (Figure 7.3(b)). The XPS result suggests that some of the europium ions have been reduced to the elemental form by the incoming aluminium atoms. With increasing aluminium loading ($[Al]/[C] = 0.023$, 1.3 \AA , and 0.048 , 2.7 \AA), the doublet associated with the neutral europium species dominates the Eu 3d spectra (Figure 7.3(c) and Figure 7.3(d)). However, the Eu 3d doublet of the europium ions persists. Since the kinetic energy of the Eu 3d photoelectrons is in the order of 300–360 eV, the inelastic mean free path of the Eu 3d photoelectrons is several times smaller than that of the C 1s photoelectrons (Briggs, 1998). Thus, the aluminium atoms probably have only interacted with the europium ions at the outmost surface of the film, and the europium ions in the sub-surface region are not affected.

The Al 2p core-level spectra, obtained at $\alpha = 90^\circ$, of the Al/PF6-Eu(dbm)₂phen interfaces at various stages of the metal deposition are shown in Figure 7.4(a-d). After the first aluminium deposition ($[Al]/[C] = 0.006$, 0.3 \AA), the Al 2p spectrum consists of one broad peak component at the BE of 74.8 eV and with a FWHM of 1.9 eV (Figure 7.4(a)), characteristic of that reported for the aluminium oxides (Seung et al., 2000). Taking into account of the changes in chemical state of the europium ions induced by the deposited aluminium atoms, the Al 2p spectral line- shape and BE are

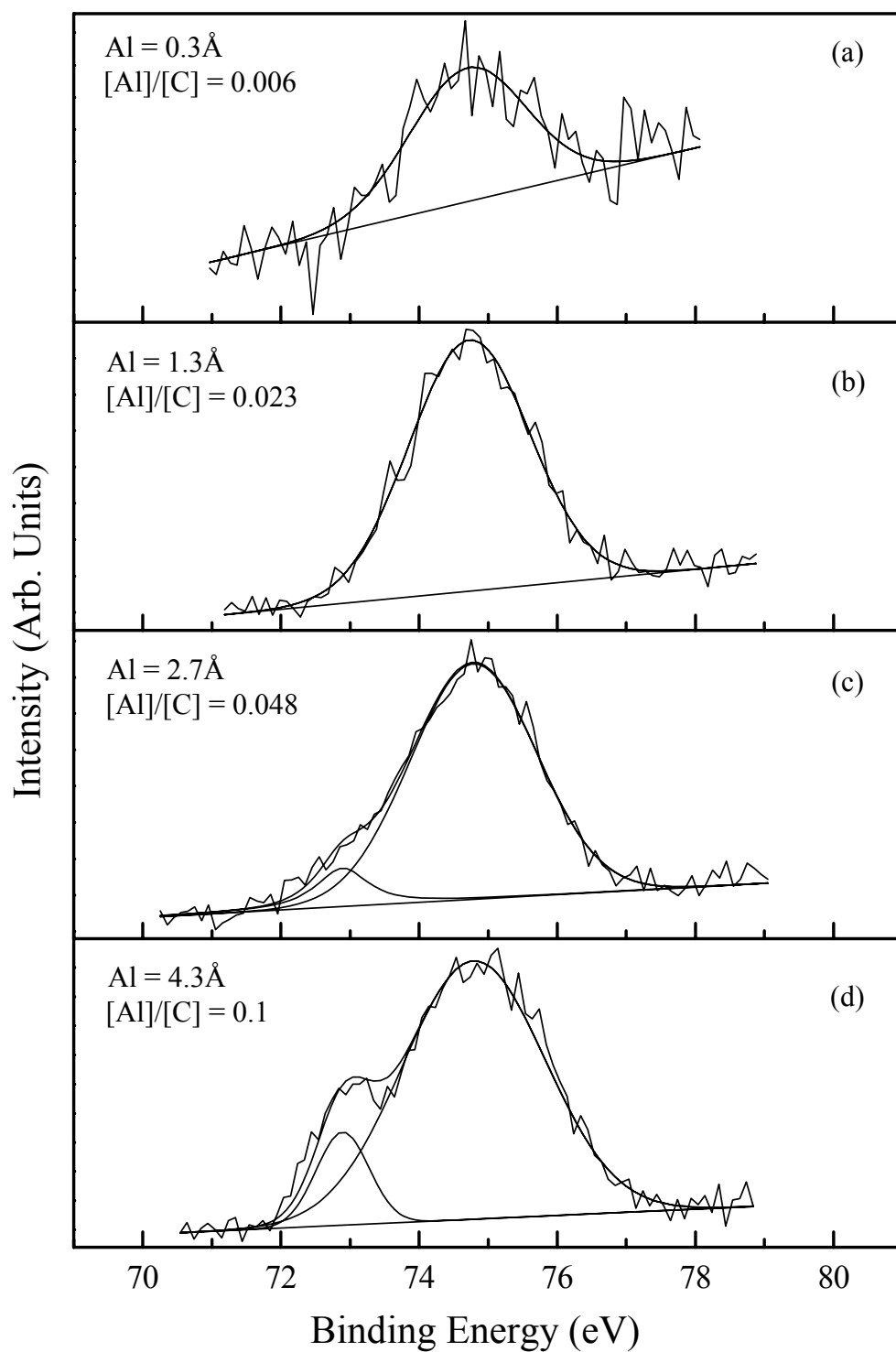


Figure 7.4 Evolution of the Al 2p core-level spectra as a function of Al coverage ($\alpha = 90^\circ$).

associated with the formations of the Al-O-C species and the Al_xO_y species, induced, respectively, by the interaction of aluminium with oxygen atoms of the copolymer and physically adsorbed oxygen in the film (see below). With further increase in aluminium deposition, the FWHM of the Al 2p peak component associated with the oxidized aluminium species increases gradually (FWHM = 2.43 eV when $[\text{Al}]/[\text{C}] = 0.1$, 4.3 Å), suggesting the formation of other oxidized aluminium species, such as aluminium carbide and Al(III)-N chelate (see below). At $[\text{Al}]/[\text{C}] = 0.048$ and an Al thickness of 2.7 Å, a low BE peak component at 72.9 eV (FWHM = 1.0 eV), attributable to metallic aluminium, appears in the Al 2p spectrum. This low BE component become more intense when the aluminium concentration is further increased to $[\text{Al}]/[\text{C}] = 0.1$.

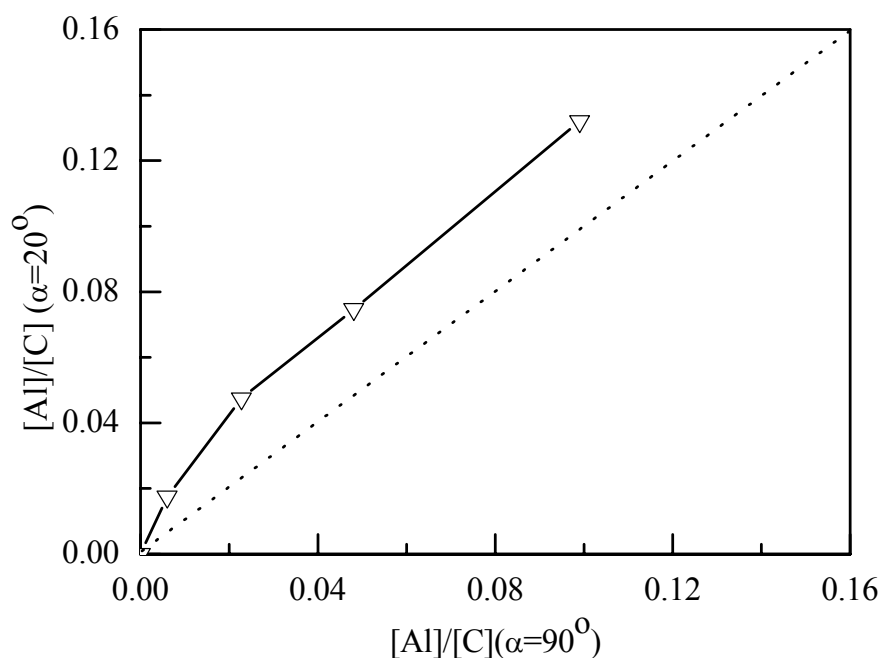


Figure 7.5 Surface concentration of Al, expressed as the $[\text{Al}]/[\text{C}]$ ratios, measured at take-off angles of $\alpha = 20^\circ$ and 90° , at different stages of the Al deposition.

The surface concentrations of aluminium on the PF6-Eu(dbm)₂phen film, measured at the α 's of 20° and 90°, are shown in Figure 7.5. At each stage of the aluminium deposition process, the concentration of aluminium at the more surface glancing angle of $\alpha = 20^\circ$ was higher than that at $\alpha = 90^\circ$, suggesting that the aluminium atoms did not diffuse extensively into the bulk of the polymer film (Atreya et al., 1999), consistent with the phenomena observed during the evolution of the C 1s and Eu 3d core-level spectra.

Figures 7.6(a-d) show the evolution of the N 1s core-level spectra, obtained at $\alpha = 90^\circ$, as a function of aluminium coverage on the PF6-Eu(dbm)₂phen film. For the pristine film, the N 1s spectrum consists of a peak component at the BE of 398.8 eV, with a FWHM of 1.0 eV. After the deposition of aluminium, the N 1s spectrum is broadened. Peak synthesis reveals that two new peak components, one at the higher BE of 399.8 eV and another at the lower BE of 397.7 eV, are discernible in the N 1s core-level spectra of the Al/copolymer interface. With increasing aluminium coverage on the polymer film, the lower BE peak component at 397.7 eV becomes more prominent.

Chelated metal ion complexes containing phenanthroline or their derivatives have been synthesized and investigated in organometallic chemistry (Bron et al., 2002; Milani et al., 2002). In these complexes, the nitrogen atoms of the phen ligand and the metal ions act as electron donors and electron acceptors, respectively, because of the higher electron affinity of the metal ions. Taking into account of the fact that the electron affinity of Al(III) ion is higher than that of Eu(III) ion (the third ionization

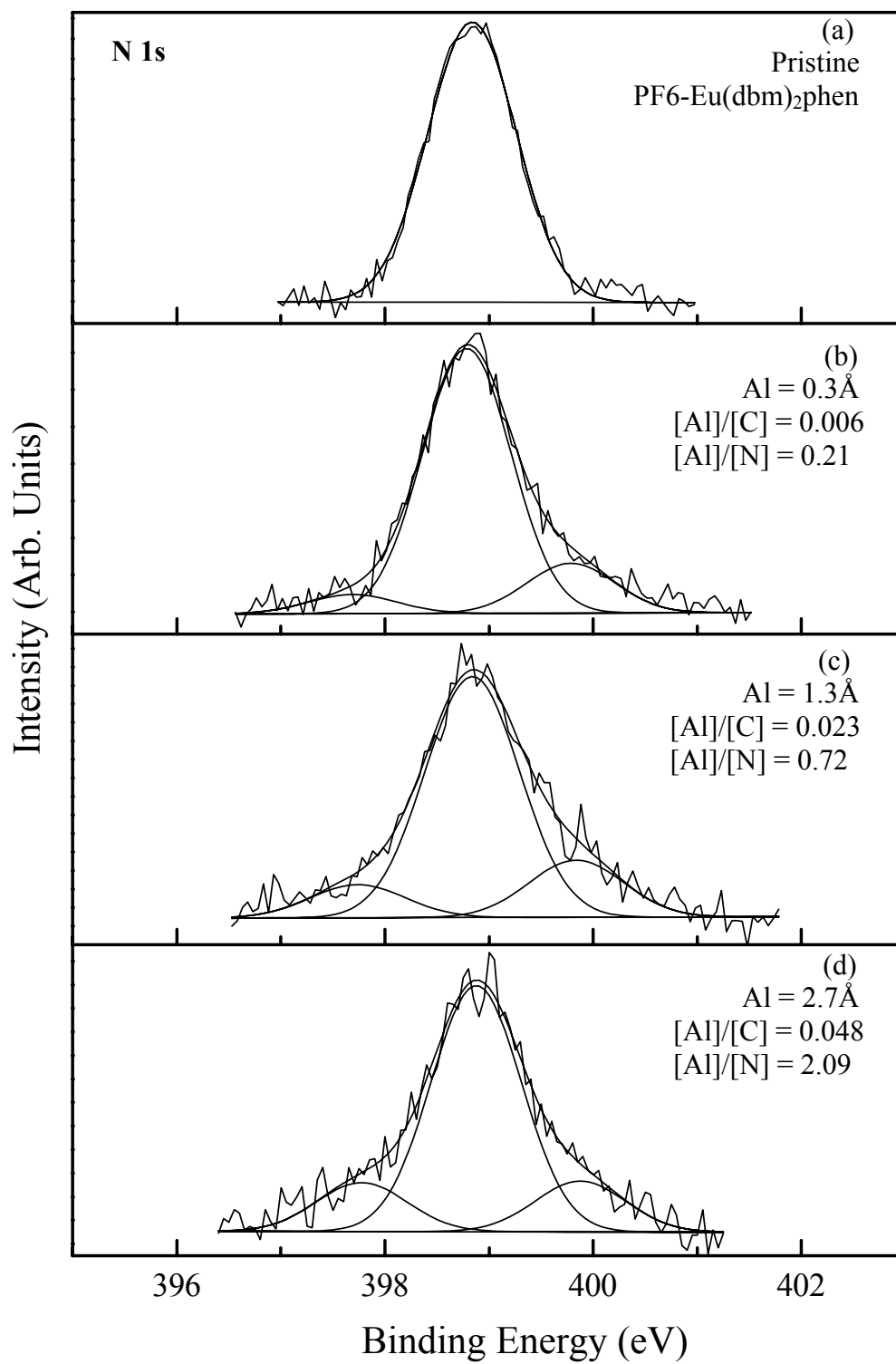


Figure 7.6 Evolution of the N 1s core-level spectra as a function of Al coverage ($\alpha = 90^\circ$)

potential of Al atom (~28.4 eV) is higher than that of the europium atom (~24.9 eV) (David, 1999)), the aluminium atoms deposited on the surface probably interact with the oxygen atoms of the copolymer and physically adsorbed oxygen at the surface, giving rise to Al(III) ions on the surface . In this process, the europium ions are reduced to the metallic state and Al(III) ions are chelated or partially chelated by the phen ligands. This chelation will contribute to the lowering of the electron density of the N atom. Thus, the appearance of the high N 1s peak component at the BE of 399.8 eV can be attributed to the formation the Al(III)-N chelate complex. On the other hand, the N 1s peak component at the lower BE of 397.7 eV, attributable to the imine (=N-) species of the phen ligand (Lim et al., 1998), also appears after the first deposition process ([Al]/[N] = 0.21), and becomes more prominent at [Al]/[N] = 2.09. This phenomenon suggests that more and more phen ligands, which chelate the Eu(III) ions, are decomplexed from the Eu(III) ions with progressive aluminium deposition at the interface.

With respect to the ideal intramolecular energy transfer in this copolymer, the dbm and phen ligands absorbs the energy transferred from PF6 (Figure 7.1), and undergoes an intersystem crossing into the triple state before the energy is transferred to the Eu(III) ions. However, the formation of Al carbide species suggests that the energy absorption of PF6 and energy transfer to dbm and phen ligands will be interrupted due to conjugated system was affected. The decomplexation of phen ligands and formation of Al-O-C and Al(III)-N species will interrupt the energy pathway from PF6 to Eu(III). Moreover, the reduction of Eu(III) will directly influence the light emission, thus, the

appearance of new interfacial states suggests that the intramolecular energy transfer in the copolymer will be affected to some extent. Thus, the expected decrease in turn-on voltage and improvement in performance of the LEDs based on rare earth complexes probably will be limited in the absence of a thin interfacial barrier. Light emitting devices based on Eu-complexes have been fabricated (McGehee et al, 1999; Kido et al., 2002). The performance of the devices has been shown to improve significantly in the presence of a thin insulating layer of LiF (1.5 nm) interposed between the cathode and the organic layer (Jabbour et al., 1999). The presence of a thin LiF layer at the Al/LiF/poly(9,9-dioctyl-fluorene) interface has been shown to protect the light-emitting polymer during aluminium deposition (Greczynski et al., 2000). It also stabilizes the interface and prevents the diffusion of metal atoms from the cathode into the organic layer.

7.3.3 Evolution of the O 1s core-level spectra and migration of oxygen from the bulk to the intersurface

The evolution of the O 1s core-level spectra upon aluminium deposition is shown in Figure 7.7. The O 1s core-level spectrum of the pristine PF6-Eu(dbm)₂phen film consists of a main peak component at the BE of about 532.2 eV and a low BE shoulder. The relative intensity of the main peak component at 532.2 eV decrease with the increase in coverage of the deposited aluminium from [Al]/[C] = 0 to [Al]/[C] = 0.1. The changes in the O 1s lineshape, arising from the increase in the relative intensity of the low BE component, indicate the presence of electrons transfer from aluminium atoms to the oxygen atoms at the interface.

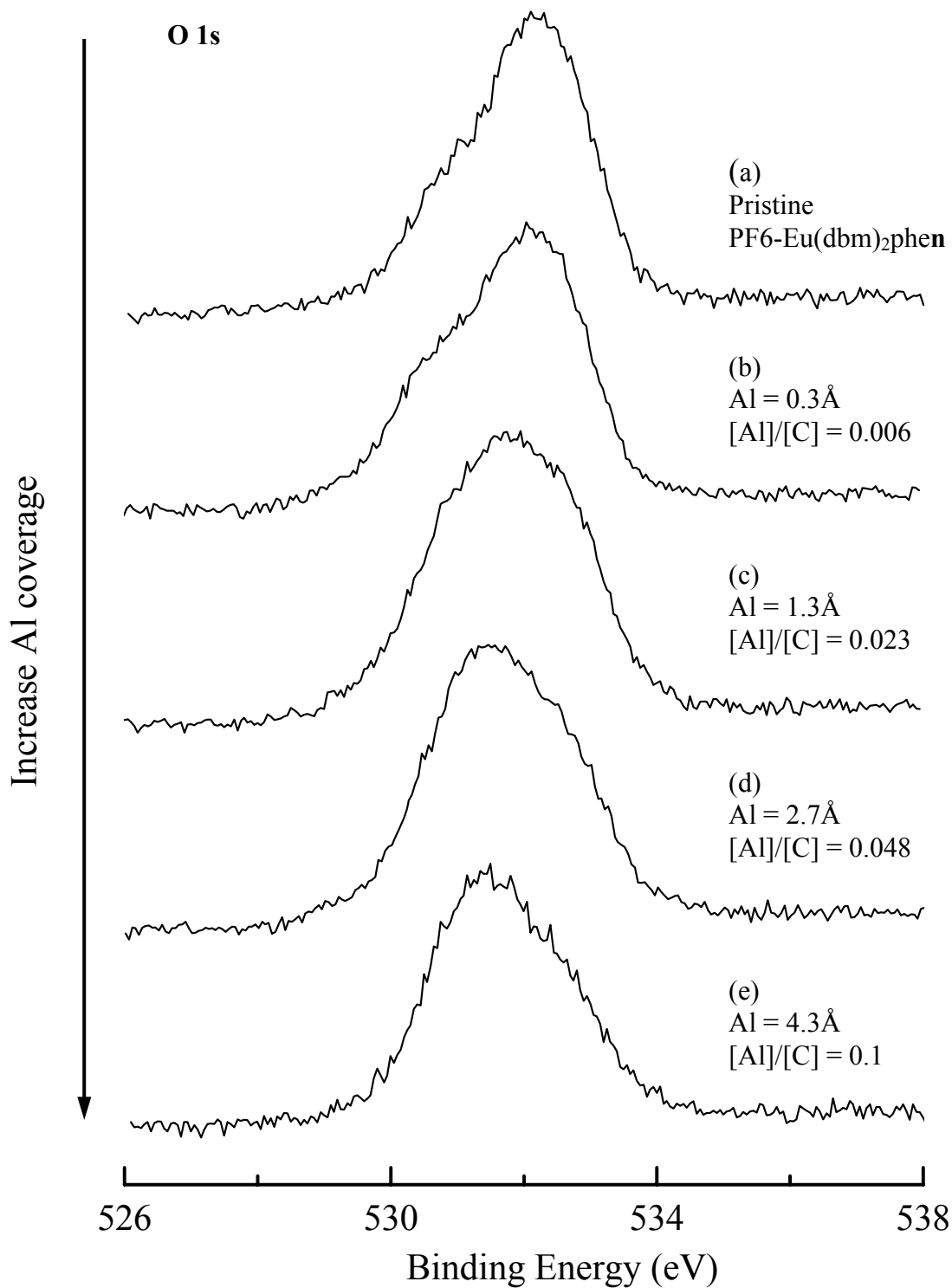


Figure 7.7 Evolution of the O 1s spectra at the Al/PF6-Eu(dbm)₂phen interface with increasing Al coverage.

Given the reactive nature of the conjugated polymer chains, the polymer film can serve as a reservoir for physically adsorbed oxygen (Uwamino et al., 1984). In order to study the behavior of the adsorbed oxygen, the oxygen concentration on the surface and in the near surface region of the conjugated polymer film was determined by angle-resolved XPS. Figure 7.8 shows the changes in [O]/[C] ratio of the surface as a function of aluminium coverage at the photoelectron take-off angles of 20° and 90° . For the pristine polymer surface, the concentration of oxygen ([O]/[C] = 0.28) measured at $\alpha = 20^\circ$ is much higher than that ([O]/[C] = 0.11) measured at $\alpha = 90^\circ$. This angular-dependent result suggests that the physically adsorbed oxygen is mostly concentrated in the outermost-surface region of the polymer film. Upon deposition of the aluminium atoms, the [O]/[C] ratio at $\alpha = 90^\circ$ increases continuously, indicating that the bulk-adsorbed oxygen has migrated to the sub-surface region of the polymer film in response to the incoming aluminium atoms. This migration behavior can be attributed to the high reactivity of the aluminium atoms, which exhibit a high affinity for the physically adsorbed oxygen. On the other hand, however, the [O]/[C] ratio in the outermost-surface region ($\alpha = 20^\circ$) decreases slightly, and levels off at about 0.25 with increasing aluminium loading. Taking into account of the evolution of the C 1s, Eu 3d, N 1s and Al 2p core-level spectra, the changes in the [O]/[C] ratios measured at $\alpha = 90^\circ$ and $\alpha = 20^\circ$ suggest that not only do the deposited aluminium atoms reduce the europium ions and form the Al-O-C complexes at the outermost surface, they also react with the physically adsorbed oxygen atoms to form aluminium oxides (Al_xO_y) layer. This aluminium oxides layer probably has prevented the diffusion of the

aluminium into the bulk, as well as the accumulation of the physically adsorbed oxygen atoms at the interface.

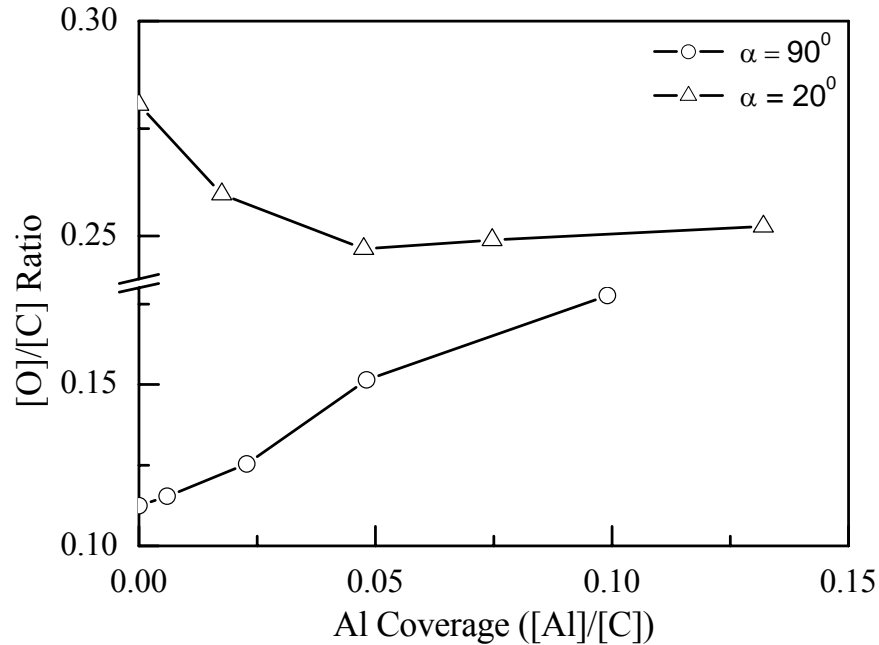


Figure 7.8 Changes in surface concentration of oxygen as a function of Al coverage.

For device fabrication, a 1.2 nm thick Al_2O_3 buffer layer interposed between Alq_3 and Al cathode was reported to improve the electron injection and electroluminescent efficiency (Li et al., 1997; Tang et al., 1997). Since Al_2O_3 is chemical stable, the improvement in the device performance is attributed to electron tunneling and removal of the exciton-quenching gap states that are intrinsic to the Al/organic interfaces. In addition to the prevention of diffusion of aluminium atoms into the organic layer, it is reasonable to expect that the performance of devices based on conjugated polymers containing rare earth complexes can be improved in the presence of a thin buffer layer of Al_2O_3 at the cathode/polymer interface.

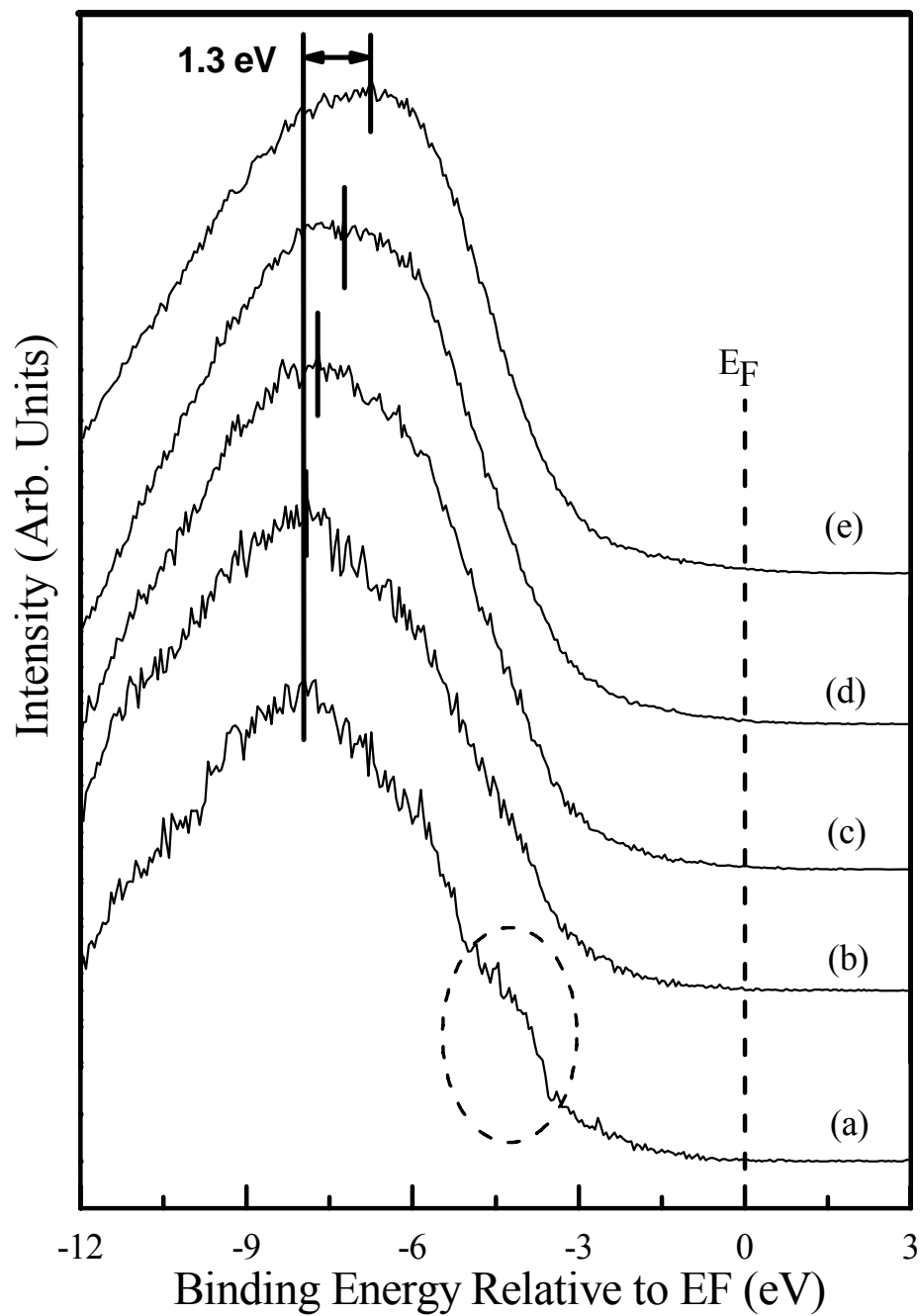


Figure 7.9 The evolution of UPS spectra as a function of Al coverage: (a) the pristine polymer, (b) $[Al]/[C] = 0.006$, 0.3\AA , (c) $[Al]/[C] = 0.023$, 1.3\AA , (d) $[Al]/[C] = 0.048$, 2.7\AA , and (e) $[Al]/[C] = 0.1$, 4.3\AA

7.3.4 Evolution of the UPS spectra upon Al deposition

The evolution of UPS spectra of the copolymer film surface as a function of aluminium coverage is shown in Figure 7.9. For the pristine copolymer (Figure 7.9(a)), a shoulder exists at the BE ~ 4 eV. However, it was no longer discernible after aluminium deposition. Further analysis of the UPS spectra of the Al/polymer interface is based on the valence state density of the polymer. From the theoretical and experimental studies (Dannetun et al., 1993), it is concluded that the σ -state due to the alkyl chain predominate in the high BE region, whereas the low BE region contains π -state contribution from the conjugated system. The disappearance of the observed shoulder (BE ~ 4 eV) after aluminium deposition suggests that the π -states of the conjugated system at the interface is interrupted by the deposited aluminium atoms. This result is consistent with the interactions between the conjugated system of the copolymer and the deposited aluminium atoms, as revealed by the *in situ* XPS analysis.

In addition, a gradual chemical shift towards lower BE's was also observed with increasing Al deposition. A shift of about 1.3 eV was observed at $[Al]/[C] = 0.1$, 4.3 \AA (Figure 7.9(e)). Since the spectral lineshape in this region is not significantly affected by Al deposition, the spectrum in this region is characteristic of the σ -states of the polymer system. Consistent with the XPS results discussed above, the chemical states of carbon atoms of the alkyl chain are not affected by the deposited aluminium atoms. The shift of the σ -states to lower BE's can probably be attributed to the electron transfer from aluminium atoms to the polymer and physically adsorbed oxygen at the interface. This phenomenon suggests that an unfavorable dipole layer, which can give

rise to a higher barrier for the electron injection in PLEDs, is formed at the interface (Hung et al., 2002). Theoretically, this dipole layer will contribute to an increase in turn-on voltage for the PLEDs.

7.4 Conclusions

The chemical states and electronic properties of the Al/PF6-Eu(dbm)₂phen interface were studied *in situ* by XPS and UPS. It was found that the deposited aluminium atoms interacted extensively with the polymer surface. In addition to the reaction with bulk adsorbed oxygen to form aluminium oxides, the deposited aluminium atoms also interacted with copolymer to cause the reduction of the Eu(III) ions and the formation of the Al carbide, Al-O-C complex, and Al(III)-N chelated complex at the interface. The interaction of aluminium with the conjugated system of the copolymer was also observed in the UPS spectra. A chemical shift ($\Delta \sim 1.3$ eV) of the UPS spectra to a low BE indicated the formation of an unfavorable dipole layer for electron injection at the interface. The observed changes at the interface suggest that the ideal intramolecular energy transfer in the copolymer required for electroluminescence will be affected by the newly formed interfacial states, albeit the formed interfacial aluminium oxide layer may serve as a beneficial barrier.

Chapter 8
Conclusions

The surface and interfacial interactions and reactions involving inorganic and organic semiconductors, such as GaAs, Si and a conjugated photoluminescent copolymer containing europium complexes (PF6-Eu(dbm)₂phen) were studied in this work. Firstly, GaAs-poly(methyl methacrylate) (GaAs-PMMA) hybrids with covalent bonded PMMA on the GaAs surface were successfully fabricated. A bifunctional molecule, 6-mercapto-1-hexanol, was used to passivate the fresh etched GaAs surface via the self-assembled of monolayers (SAMs) of 6-mercapto-1-hexanol on the GaAs surface. The Ga-S and As-S bonds formed on the GaAs surface were verified by XPS. After the immobilization of ATRP initiator on the GaAs surface by further functionalizing the OH groups (of 6-mercapto-1-hexanol) on the GaAs surface, the GaAs-PMMA hybrids were prepared via surface-initiated by ATRP of methyl methacrylate (MMA) at room temperature. The chemical states of the passivated GaAs surfaces were not significantly affected by the ATRP process. The preparation of GaAs-PMMA hybrid presented here provides a simple approach to the preparation of GaAs-polymer hybrids with well-defined polymer brushes and preserved interfacial states.

In addition, ZnO-PMMA core-shell hybrid nanoparticles were also successfully prepared via surface-initiated ATRP of MMA from ATRP initiators immobilized on ZnO nanoparticles by acid-base interaction. The chemical compositions of the nanoparticles were investigated by XPS. The morphology and structure of the nanoparticles were determined by FE-SEM and TEM. The optical properties of the nanoparticles were also studied by UV and photoluminescence measurement. The

polymer-functionalized ZnO nanoparticles could become well-dispersed with significant enhancement of UV-visible absorption and fluorescence intensities.

Self-assembled monolayers of ZnO colloidal QDs on the MPTMS-passivated GaAs surface were demonstrated. Not only does MPTMS act as a coupling agent for the ZnO QDs, it also passivates the GaAs surface through the formation of covalent As-S and Ga-S bonds. Thus, the present study provides a simple approach to the self-assembly of semiconductor ZnO colloidal QDs on an oriented single crystal GaAs substrate with simultaneous passivation of the latter. The strategy developed in this work based on the mercaptosilane coupling agent can be readily extended to the fabrication of micropatterned SAMs of colloidal QDs on GaAs substrates, for example, by microcontact printing

On the other hand, the different effects of the hydrogen-terminated silicon surfaces (H-Si surfaces) and oxide silicon surfaces (ox-Si surfaces) on the plasma-polymerized and -deposited fluoropolymer films were investigated. Ultra-thin fluoropolymer films were deposited on H-Si and ox-Si surfaces via plasma polymerization and deposition of four fluoro-monomers, PFS, HFB, HDFD, and PFH. XPS results revealed the formation of the F-Si bonds and Si-C bonds on the original H-Si surface, which were probably formed through the interaction of the monomer or oligomer fragments or radicals with the dangling bonds on the silicon surfaces during the plasma polymerization. Consequently, the plasma-deposited fluoropolymer films were strongly bonded to the H-Si surfaces. The preservation of the fluorinated aromatic

rings in the pp-PFS and pp-HFB films were suggested by FTIR results. In addition, ToF-SIMS results suggested selective polymerization of the PFS monomer through the vinyl group of PFS.

The chemical states and electronic properties of the interface between aluminium and a novel conjugated copolymer of hexylfluorene and benzoate containing chelated Eu complexes (PF₆-Eu(dbm)₂phen) were studied *in situ* by XPS and UPS. The deposited Al atoms was found to interact with the copolymer, resulting in reduction of the Eu(III) ions, formation of the Al carbide and Al-O-C complex, and formation of Al(III)-N chelate complex at the interface. In addition, the conjugated system of the copolymer was affected by the deposited aluminium atoms, as suggested by the UPS spectra. A chemical shift ($\Delta \sim 1.3$ eV) of the UPS spectra to a low BE indicated the formation of an unfavorable dipole layer for electron injection at the interface. The deposited aluminium atoms also reacted with adsorbed oxygen in copolymer thin film to form aluminium oxides, which might have prevented aluminium diffusion into the copolymer film. The observed changes at the interface suggest that the ideal intramolecular energy transfer leading to monochromatic red emission in the copolymer would be affected by the newly formed interfacial states and chemical species, albeit the formed interfacial aluminium oxide layer may serve as a beneficial barrier.

Chapter 9

References

Adlkofer, K. and M. Tanata. Stable Surface Coating of Gallium Arsenide with Octadecylthiol Monolayers, *Langmuir*, 17, pp. 4267-4273. 2001.

Adlkofer, K., W. Eck, M. Frunze and M. Tanaka. Surface Engineering of Gallium Arsenide with 4-mercaptobiphenyl Monolayers. *J. Phys. Chem. B*, 107, pp. 587-591. 2003.

Alivisatos, A.P. Semiconductor Clusters, Nanocrystals, and Quantum Dots, *Science*, 271, pp. 933-937. 1996.

Arens, M., J. Kinsky, W. Richter and K. Eberl. HREELS Analysis of Band Bending on Sulfur-Covered GaAs(100) Surfaces. *Surf. Sci.* 352-354, pp. 740-744. 1996.

Atreya, M., S. Li, E.T. Kang, K.G. Neo, Z.H. Ma and K.L. Tan. *In situ* X-Ray Photoelectron Spectroscopy Studies of Interactions of Evaporated Metals with Poly(*p*-phenylene vinylene) and Its Ring-Substituted Derivatives. *J. Vac. Sci. Technol. A*, 17, pp. 853-861. 1999.

Bahnemann, D.W., C. Kormann and M.R. Hoffmann. Preparation and Characterization of Quantum Size Zinc-Oxide: A Detailed Spectroscopic Study, *J. Phys.Chem.*, 91, pp. 3789-3798. 1987.

Baldo, M.A., C. Adachi and S.R. Forrest. Transient Analysis of Organic Electrophosphorescence. II. Transient Analysis of Triplet-Triplet Annihilation, *Phys. Rev. B*, 62, pp. 10967-10977. 2000.

Baldo, M.A., D.F. O'Brien, Y. You, A. Shoustikov, S. Sibley, M.E. Thompson and S.R. Forrest. Highly Efficient Phosphorescent Emission from Organic Electroluminescent Devices, *Nature*, 395, pp. 151-154. 1998.

Baldo, M.A., S. Lamansky, P.E. Burrows, M.E. Thompson and S.R. Forrest. Very High-Efficiency Green Organic Light-Emitting Devices Based on Electrophosphorescence, *Appl. Phys Lett.*, 75, pp. 4-6. 1999.

Baldo, M.A. and S.R. Forrest. Transient Analysis of Organic Electrophosphorescence. I. Transient Analysis of Triplet Energy Transfer, *Phys. Rev. B*, 62, pp. 10958-10966. 2000.

Baldo, M.A. and S. R. Forrest, Interface-Limited Injection in Amorphous Organic Semiconductors, *Phys. Rev. B*, 64, pp. 085201-1-085201-17. 2001.

Beamson, G. and D. Briggs. High Resolution XPS of Organic Polymer: The Scienta ESCA300 Database, Wiley, Chichester, 1992.

- Beek, W.J.E., M.M. Wienk and R.A.J. Janssen. Efficient Hybrid Solar Cells from Zinc Oxide Nanoparticles and a Conjugated Polymer. *Adv. Mater.*, 16, pp. 1009-1013. 2004.
- Benouada, H.B., H. Hommel, A.P. Legrand, H. Balard and E.J. Papirer. Organization of the Layers of Polyethylene Oxide Grafted with Different Densities on Silica. *J. Colloid Interface Sci.*, 122, pp. 441-449. 1998.
- Besser, R.S. and C.R. Helms. Effect of Sodium Sulfide Treatment on band Bending in GaAs, *Appl. Phys. Lett.*, 52, pp 1707-1709. 1988.
- Bimberg, D., M. Grundmann and N.N. Ledentsov. *Quantum Dot Heterostructures* (John Wiley & Sons, Chichester), 1999.
- Braun, D. and A.J. Heeger. Visible Light Emission from Semiconducting Polymer Diodes, *Appl. Phys. Lett.*, 58, pp. 1982-1984. 1991.
- Bridger, K. and B. Vincent. The Terminal Grafting of Poly(ethylene oxide) Chains to Silica Surfaces, *Eur. Polym. J.*, 16, pp. 1017-1021. 1980.
- Briggs, D. *Surface Analysis of Polymer by XPS and Static SIMS*, pp. 36-37. Cambridge University Press, Chambridge, 1998.
- Bron, M., J. Radnik, M. Fieber-Erdmann, P. Bogdanoff and S. Fiechter. EXAFS, XPS and Electrochemical Studies on Oxygen Reduction Catalysts Obtained by Heat Treatment of Iron Phenanthroline Complexes Supported on High Surface Area Carbon Black, *J. Electroanal. Chem.*, 535, pp. 113-119. 2002.
- Brown, A.R., D.D.C. Bradley, J.H. Burroughes, R.H. Friend, N.C. Greenham, P.L. Burn, A.B. Holmes and A. Kraft, Poly(*p*-phenylenevinylene) Light-Emitting Diodes: Enhanced Electroluminescent Efficiency Through Charge Carrier Confinement, *Appl. Phys. Lett.* 61, pp. 2793-2795. 1992.
- Buchmeiser, M.R., F. Sinner, M. Mupa and K. Wurst. Ring-Opening metathesis Polymerization for the Preparation of Surface-Grafted Polymer Supports, *Macromolecules*, 33, pp. 32-39. 2000.
- Burroughes, J.H., D.D.C. Bradley, A.R. Brown, R.N. Marks, K. Mackay, R.H. Friend, P.L. Burns and A.B. Homes, Light-Emitting Diodes Based on Conjugated Polymers, *Nature*, 347, pp. 539-541. 1990.
- Cai, Q.J., G.D. Fu, F.R. Zhu, E.T. Kang and K.G. Neoh. GaAs-Polymer Hybrids Formed by Surface-Initiated Atom-Transfer Radical Polymerization of Methyl Methacrylate, *Angew. Chem. Int. Ed.*, 44, 1104-1107. 2005.

Cao, X.Y. and R.J. Hamers. Formation of a Surface-Mediated Donor-Acceptor Complex: Coadsorption of Trimethylamine and Boron Trifluoride on the Silicon (001) Surface, *J. Phys. Chem. B*, 106, pp.1840-1842. 2002.

Cao, Y., I.D. Parker, G. Yu, C. Zhang and A.J. Heeger. Improved Quantum Efficiency for Electroluminescence in Semiconducting Polymers, *Nature*, 397, pp. 414-417. 1999.

Carlsson, N., W. Seifert, A. Petersson, P. Castrillo, M.E. Pistol and L. Samuelson. Study of the 2-Dimensional 3-Dimensional Growth Mode Transition in Metalorganic Vapour-Phase Epitaxy of GaInP/InP Quantum-Sized Structure, *Appl. Phys. Lett.*, 65, pp. 3093-3095. 1994.

Carpenter, M.S., M.R. Melloch and T.E. Dungan. Schottky Barrier Formation on $(\text{NH}_4)_2\text{S}$ -Treated *n*- and *p*-type (100)GaAs, *Appl. Phys. Lett.*, 53, pp.66-68. 1988.

Chen, W., A.Y. Fadeev, M.C. Hsieh, D. Oner, J. Youngblood and T.J. McCarthy. Ultrahydrophobic and Ultralyophobic Surfaces: Some Comments and Examples, *Langmuir*, 15, pp. 3395-3399. 1999.

Chhabra, V., V. Pillai, B.K. Mishra, A. Morrone and D.O. Shah. Synthesis, Characterization, and Properties of Microemulsion-Mediated Nanophase TiO_2 Particles, *Langmuir*, 11, pp. 3307-3311. 1995.

Chmiel, G. and H. Gerischer. Photoluminescence at A Semiconductor-Electrolyte Contact around and beyond the Flat-Band Potential, *J. Phys. Chem.* 94, pp. 1612-1619. 1990.

Choi, J., R. Puthenkovilakam and J.P. Chang. Band Structure and Alignment of the AlN/SiC Heterostructure, *Appl. Phys. Lett.*, 86, pp. 192101-192103. 2005.

Choong, Y.E., M.G. Mason, C.W. Tang and Y. Gao. Investigation of the Interface Formation between Calcium and Tris(8-hydroxyquinoline)aluminum, *Appl. Phys. Lett.* 72, pp. 2689-2691. 1998.

Cicero, R.L., M.R. Linford and C.E.D. Chidsey. Photoreactivity of Unsaturated Compounds with Hydrogen-Terminated Silicon(111), *Langmuir*, 14, pp. 5688-5695. 2000.

Clark, D.T. and M.Z. Abraham. Plasma Polymerization. VII. An ESCA Investigation of the RF Plasma polymerization of Perfluorobenzene and Perfluorobenzene/Hydrogen Mixtures. *J. Poly. Sci.*, 20, pp. 1717-1728. 1982.

Coulson, D.R. *Inorganic Synthesis*. Vol. XIII, pp. 121-197. McGraw-Hill, New York, 1972.

- Coulson, S.R., I. Woodward, J.P.S. Badyal, S.A. Brewer and C. Willis. Super-Repellent Composite Fluoropolymer Surfaces. *J. Phys. Chem.*, 104, pp. 8836-8840. 2000.
- Coulson, S.R., I. Woodward, J.P.S. Badyal, S.A. Brewer and C. Willis. Ultralow Surface Energy Plasma Polymer Films, *Chem. mater.*, 12, pp. 2031-2038. 2000.
- Cowans, B.A., Z. Dardas, W.N. Delgass, M.S. Carpenter and M.R. Melloch. X-Ray Photoelectron Spectroscopy of Ammonium Sulfide Treated GaAs(100) Surfaces, *Appl. Phys. Lett.*, 54, pp. 365-367. 1989.
- Crispin, X., V. Geskin, A. Crispin, J. Cornil, R. Lazzaroni, W.R. Salaneck and J. breads. Characterization of Interface Dipole at Organic/Metal Interfaces, *J. Am. Chem. Soc.*, 124, pp. 8131-8141. 2002.
- Dannetun, P., M. Boman, S. Stafström, W.R. Salaneck, R. Lazzarozi, C. Fredriksson, J.L. Brédas, R. Zamboni and C. Taliani. The Chemical and Electronic Structure of the Interface between Aluminum and polythiophene Semiconductors. *J. Chem. Phys.*, 99 pp. 664-672. 1993.
- Davis, K.A., H.-j. Paik and K. Matyjaszewski. Kinetic Investigation of the Atom Transfer Radical Polymerization of Methyl Acrylate. *Macromolecules*, 32, pp. 1767-1776. 1999.
- David, R.L. (Ed). *CRC Handbook of Chemistry and Physics on CD-ROM*, pp. 10-175, CRC Press, Boca Raton, 1999.
- de Boer, B., H.K. Simon, M.P.L. Werts, E.W. van der Vegte and G. Hadziioannou. "Living" Free Radical Photopolymerization Initiated from Surface-Grafted Iniferter Monolayers, *Macromolecules*, 33, pp. 349-356. 2000.
- Dietl, T. Ferromagnetic Semiconductors, *Semicond. Sci. Technol.*, 17, pp. 377-392. 2002.
- Dorsten, J.F., J.E. Maslar and P.W. Bohn. Near-Surface Electronic Structure in GaAs (100) Modified with Self-Assembled Monolayers of Octadecylthiol, *Appl. Phys. Lett.*, 66, 1755-1757. 1995.
- Eaton, P.J., P. Graham, J.R. Smith, J.D. Smart, T.G. Nevell and J. Tsibouklis. Mapping the Surface Heterogeneity of a Polymer Blend: An Adhesion-Force-Distribution Study Using the Atomic Force Microscope, *langmuir*, 16, pp. 7887-7890. 2000.
- Effenberger, F., G. Götz, B. Bidlingmaier and M. Wezstein. Photoactivated Preparation and Patterning of Self-Assembled Monolayers with 1-Alkene and Aldehydes on Silicon Hydroxide Surface, *Angew. Chem. Int. Ed.*, 37, pp. 2462-2464. 1998.

Ejaz, M., S. Yamamoto, K. Ohno, Y. Tsujii and T. Fukuda. Controlled Graft Polymerization of Methyl Methacrylate on Silicon Substrate by the Combined Use of the Langmuir-Blodgett and Atom Transfer Radical Polymerization Techniques, *Macromolecules*, 31, pp. 5934-5936. 1998.

Endo, K., K. Shinoda and T. Tatsumi. Plasma Deposition of Low-Dielectric-Constant Fluorinated Amorphous Carbon, *J. Appl. Phys.*, 86, pp. 2739-2745. 1999.

Ermolieff, A., S. Marthon, F. Bertin and F. Pierre. X-Ray photoelectron Spectroscopy Studies of Contamination and Cleaning of Surface Exposed to a Fluorocarbon Plasma, *J. Vac. Sci. Technol. A*, 9, pp. 2900-2906. 1991.

Etteedgui, E., H. Razafitrimo, Y. Gao and B.R. Hsieh. Schottky Barrier Formation at the Ca/Poly(p-phenylenevinylene) Interface and Its Role in Tunneling at the Interface, *Synth. Met.*, 78, pp. 247-252. 1996.

Fahlman, M., D. Beljonne, M. Lögdlund, P.L. Burn, A.B. Holmes, R.H. Friend, J.L. Brédas and W.R. Salaneck. Experimental and Theoretical Studies of the Electronic Structure of Na-doped Poly(p-phenylenevinylene), *Chem. Phys. Lett.*, 214, pp. 327-332. 1993.

Fahlman, M. and W.R. Salaneck. Surface and Interfaces in Polymer-Based Electronics, *Surf. Sci.*, 500, pp. 904-922. 2002.

Fischer, H. The Persistent Radical Effect: A Principle for Selective Radical Reactions and Living Radical Polymerizations, *Chem. Rev.*, 101, pp. 3581-3610. 2001.

Flores, M., V. Fuenzalida and P. Häberle. Thermal Effects in the Size Distribution of SiC Nanodots on Si(111), *Phys. Stat.sol.*, 202, pp. 1959-1966. 2005.

Fu, G.D., Y. Zhang, E.T. Kang and K.G. Neoh. Nanoporous Ultra-Low- κ Fluoropolymer Composite Films Via Plasma Polymerization of Allylpentafluorobenzene and Magnetron Sputtering of Poly(tetrafluoroethylene), *Adv. Mater.*, 16, pp. 839-842. 2004.

Fujihira, M., Y. Tani, M. Furugori, U. Akiba and Y. Okabe. Chemical Force Microscopy of Self-Assembled Monolayers on Sputtered Gold Films Patterned by Phase Separation, *Ultramicroscopy*, 86, pp. 63-73. 2001.

Gangopadhyay, S., G.C. Hadjipanyis, B. Dale, C.M. Sorenson, K.J. Klabunde, V. Papaefthymiou and A. Kosikas. Magnetic Properties of Ultrafine Iron Particles. *Phys. Rev. B*, 45, pp. 9778-9787. 1992.

Gao, Y. Surface Analytical Studies of Interface Formation in Organic Light-Emitting Devices, *Acc. Chem. Res.*, 32 pp. 247-255. 1999.

- Ghis, A., R. Meyer, R. Rambaud, F. Levy and T. Leroux. Sealed Vacuum Devices: Fluorescent Microtip Displays. *IEEE Trans, Electron Devices*, 38, pp. 2320-2322. 1991.
- Golub, M.A., T. Wydeven and A. Johnson. Similarity of Plasma-Polymerized Tetrafluoroethylene and Fluoropolymer Films Deposited by rf Sputtering of Poly(tetrafluoroethylene), *Langmuir*, 14, pp. 2217-2220. 1998.
- Greczynski, G., M. Fahlman and W.R. Salaneck. An Experimental Study of Poly(9,9-dioctyl-fluorene) and Its Interface with Li and LiF, *Appl. Surf. Sci.*, 166, pp. 380-386. 2000.
- Green, A.M. and W.E. Spicer. Do We Need A New Methodology for GaAs Passivation?, *J. Vac. Sci. Technol. A*, 11, pp. 1061-1069. 1993.
- Guha, S., A. Madhukar and K.C. Rajkumar. Onset of Incoherency and Defect Introduction in the Initial-Stages of Molecular-Beam Epitaxial-Growth of Highly Strained $\text{In}_x\text{Ga}_{1-x}\text{As}$ on GaAs(100), *Appl. Phys. Lett.*, 57, pp. 2110-2112. 1990
- Guo, L., S. Yang, C. Yang, P.Yu, J. Wang, W. Ge and G.K.L Wong. Synthesis and Characterization of Poly(Vinylpyrrolidone)-Modified Zinc Oxide Nanoparticles, *Chem. Mater.*, 12, pp. 2268-2274. 2000.
- Guo, L., Y.L. Ji, H. Xu, P. Simon and Z. Wu. Regularly Shaped, Single-Crystalline ZnO Nanorods with Wurtzite Structure, *J. Am. Chem. Soc.*, 124, pp. 14864-14865. 2002.
- Han, L.C.M., R.B. Timmons and W.W. Lee. Pulsed Plasma Polymerization of an Aromatic Perfluorocarbon Monomer: Formation of Low Dielectric Constant, High Thermal Stability Films, *J. Vac. Sci. Technol. B*, 18, pp. 799-804. 2000.
- Han, L.C.M., R.B. Timmons, W.W. Lee, Y. Chen and Z. Hu. Pulsed Plasma Polymerization of Pentafluorostyrene: Synthesis of Low dielectric Constant Films, *J. Appl. Phys.*, 84, pp. 439-444. 1998.
- Hanton, S.D. Mass Spectrometry of Polymers and Polymer Surfaces, *Chem. Rev.*, 101, pp. 527-570. 2001.
- He. J., R. Nötzel, P. Offermans, P.M. Koenrad, Q. Gong and G.J. Hamhuis. Formation of Columnar (In,Ga)As Quantum Dots on GaAs(100), *Appl. Phys. Lett.*, 85, pp. 2771-2773. 2004.
- Heinrichsdorff, F., A. Krost, M. Grundmann, D. Bimberg, A.O. Kosogov and P. Werner. Self-Organization Processes of InGaAs/GaAs Quantum Dots Grown by Metalorganic Chemical Vapor Deposition, *Appl. Phys. Lett.*, 68, pp. 3284-3286. 1996.

- Hermann, W.A., A.W. Stumpf, S. Bogdanovic, V. Dufaud and J.-M. Basset. A Molecularly Defined, Grafted Olefin Metathesis Catalyst from Tris(neopentyl)-nitridomolybdenum, *Angew. Chem., Int. Ed.*, 35, pp. 2803-2805. 1996.
- Hide, F., M.A. Díaz-García, B.J. Schwartz and A.J. Heeger, New Developments in the Photonic Applications of Conjugated Polymers, *Acc. Chem. Res.*, 30 pp. 430-436. 1997.
- Higashi, G.S., G. W. Chabal, G. W. Trucks and K. Raghavachari. Ideal Hydrogen Termination of the Si (111) Surface, *Appl. Phys. Lett.*, 56, pp. 656-658. 1990.
- Hill, I.G., A. Rajagopal and A. Kahn. Energy-Level Alignment at the Interfaces between Metals and Organic Semiconductor 4,4'-N,N'-dicarbazolyl-biphenyl, *J. Appl. Phys.*, 84, pp. 3236-3241. 1998.
- Hou, T., M. Greenlief, S.W. Leller, L. Nelen and J.F. Kauffman. Passivation of GaAs(100) with an Adhesion Promoting Self-Assembled Monolayer, *Chem. Mater.*, 9, pp. 3181-3186. 1997.
- Houston, M.R. and R. Maboudian. Stability of Ammonium Fluoride-Treated Si(100), *J. Appl. Phys.*, 78, pp. 3801-3808. 1995.
- Huang, M.B., K. McDonald, J.C. Keay, Y.Q. Wang, S.J. Rosenthal, R.A. Weller and L.C. Feldman. Suppression of Penetration of Aluminum into 8-hydroxyquinoline Aluminum via a Thin Oxide Barrier, *Appl. Phys. Lett.*, 73, pp. 2914-2916. 1998.
- Huang, M.H., Y. Wu, H. Feick, N. Tran, E. Weber and P. Yang. Catalytic Growth of Zinc Oxide Nanowires by Vapor Transport, *Adv. Mater.*, 13, pp.113-116. 2001.
- Huang, X. and M.J. Wirth. Surface Initiation of Living Radical Polymerization for Growth of Tethered Chains of Low Polydispersity, *macromolecules*, 32, pp. 1694-1696. 1999.
- Hung, C.H. and W.T. Whang. Effect of Surface Stabilization of Nanoparticles on Luminescent Characteristics in ZnO/poly(hydroxyethyl methacrylate) Nanohybrid Films, *J. Mater. Chem.*, 15, pp. 267-274. 2005.
- Hung, L.S. and C.H. Chen. Recent Progress of Molecular Organic Electroluminescent Materials and Devices, *Mat. Sci. Eng. R*, 39, pp. 143-222. 2002.
- Husemann, M., D. Mecerreyes, C.J. Hawker, J.L. Hedrick, R. Shah and N.L. Abbott. Surface-Initiated Polymerization for Amplification of Self-Assembled Monolayers Pattern by Microcontact Printing, *Angew. Chem., Int. Ed.*, 38, pp. 647-649. 1999.
- Husseman, M., E.E. Malmstron, M. McNamara, M. Mate, D. Mecerreyes, D.G. Benoit, J.L. Hedrick, P. Mansky, E. Huang, T.P. Russell and C. J. Hawker. Controlled

Synthesis of Polymer Brushes by "Living" Free Radical Polymerization Techniques, *Macromolecules*, 32, pp. 1424-1431.

Inagaki, N. *Plasma Surface Modification and Plasma Polymerization*, Chap.5, Technomic, Lancaster, PA, 1996.

Ingall, M.D.K., C.H. Houeyman, J.V. Mercure, P.A. Bianconi and P.R. Kunz. Surface Functionalization and Imaging Using Monolayers and Surface-Grafted Polymer Layers, *J. Am. Chem. Soc.*, 121, pp.3607-3613.1999.

Ishii, H. and K. Seki. Energy Level Alignment at Organic/Metal interfaces Studied by UV Photoemission: Breakdown of Traditional Assumption of a Common Vacuum Level at the Interface, *IEEE Trans. Electron. Devices*, 44, pp. 1295-1301. 1997.

Ishii, H., K. Sugiyama, E. Ito and K. Seki. Energy Level Alignment and Interfacial Electronic Structure at Organic/Metal and Organic/Organic interfaces, *Adv. Mater.*, 11, pp. 605-625. 1999.

Iucci, G., K. Xing, M. Lögdlund, M. Fahlman and W.R. Salaneck. Polaron to bipolaron transition in a conjugated polymer: Rubidium-doped poly(p-phenylenevinylene), *Chem. Phys. Lett.*, 244, pp. 139-144. 1995.

Jabbour, G.E., J.-F. Wang, B. Kippelen and N. Peyghambarian. Sharp Red Organic Light-Emitting Devices with Enhanced Efficiency, *Jpn. J. Appl. Phys.*, 38, pp. L1553-L1555. 1999.

Johansson, N., T. Osada, S. Stafstrom, W.R. Salaneck, V. Parente, D.A. dos Santos, X. Crispin and J.L. Bredas. Electronic Structure of Tris(8-hydroxyquinoline)aluminum Thin Films in the Pristine and Reduced States, *J. Chem. Phys.*, 111, pp. 2157-2163. 1999.

Joo, J., H.B. Na, T. Yu, Y.W. Kim, F. Wu, J.Z. Zhang and T. Hyeon. Generalized and Facile Synthesis of Semiconducting Metal Sulfide Nanocrystals, *J. Am. Chem. Soc.*, 125, pp. 11100-11105. 2003.

Jordan, R. and A. Ulman. Surface Initiated Living Cationic Polymerization of 2-Oxazolines, *J. Am. Chem. Soc.*, 120, pp. 243-247. 1998

Jordan, R., A. Ulman, J.F. Kang, M.H. Rafailovich and J. Sokolov. Surface-Initiated Anionic Polymerization of Styrene by Means of Self-Assembled Monolayers, *J. Am. Chem. Soc.*, 121, pp. 1016-1022. 1999.

Jun, Y.W., J.E. Koo and J. Cheon. One-Step Synthesis of Size Tuned Zinc Selenide Quantum Dots *via* a Temperature Controlled Molecular Precursor Approach, *Chem. Comm.*, pp. 1243-1244. 2000.

- Kaeriyama, K., M.A. Mehta, V. Chaturvedi and H. Masuda. Poly(alkyl benzoate)s: Preparation, Properties and Conversion to Polyphenylenes, *polymer*, 36 (15), pp. 3027-3033. 1995.
- Kamigaito, M., T. Ando and M. Sawamoto. Metal-Catalyzed Living Radical Polymerization, *Chem. Rev.*, 101, pp. 3689-3745. 2001.
- Kang, E.T., K.G. Neoh and K.L. Tan. Handbook of Organic Conductive Molecules and Polymers, Vol. 3, pp. 121-136. Wiley, Chichester, 1997.
- Kang, M.-G. and H.-H. Park. Surface Preparation and Effective Contact Formation for GaAs surface, *Vacuum*, 67, pp. 91-100. 2002.
- Kataoka, D.E. and S.M. Troian. Patterning Liquid Flow on the Microscopic Scale, *Nature*, 402, pp. 794-797. 1999.
- Katz, E. and I. Willner. Integrated Nanoparticle-Biomolecule Hybrid Systems: Synthesis, Properties, and Applications, *Angew. Chem. Int. Ed.* 43, pp. 6042-6108. 2004.
- Kauffman, J.F., B.A. Balko and G.L. Richmond. Power Dependent Effects in the Luminescence Decay of Gallium Arsenide/Electrolyte Contacts at the Flat Band Potential, *J. Phys. Chem.*, 96, pp. 6371-6374. 1992.
- Kauffman, J.F., B.A. Balko and G.L. Richmond. Power Dependent Effects in Photoluminescence vs Voltage Scans of Gallium Arsenide/Electrolyte Junctions Using Picosecond Pulse Excitation, *J. Phys. Chem.*, 96, pp. 6374-6377. 1992.
- Kido, J. and Y. Okamoto. Organo Lanthanide Metal Complexes for Electroluminescent Materials, *Chem. Rev.*, 102 pp. 2357-2368. 2002.
- Kim, C., K. Sung, T. Chung, D.Y. Jung and Y. Kim. Monodispersed ZnO Nanoparticles from a Single Molecular Precursor, *Chem. Comm.*, pp. 2068-2069. 2003.
- Kim, J., M.L. Bruening and G.L. Baker. Surface-Initiated Atom Transfer Radical Polymerization on Gold at Ambient Temperature. *J. Am. Chem. Soc.*, 122, pp. 7616-7617. 2000.
- Klug, H.P. and L.E. Alexander. X-Ray Diffraction Procedures for Polycrystalline and Amorphous Materials (Wiley, New York), 1967.
- Koch, U., A. Fojtik, H. Weller and A. Henglein. Photochemistry of Semiconductor Colloids. 13. Preparation of Extremely Small ZnO Particles, Fluorescence Phenomena and Size Quantization Effects, *Chem. Phys. Lett.*, 122, pp. 507-510. 1985.

- Kricka, L.J. Microchips, Microarrays, Biochips and Nanochips: Personal Laboratories for the 21st Century, *Clin. Chim. Acta*, 307, pp. 219-223. 2001.
- Krisnan, M., V. Namasivayam, R.S. Lin, R. Pal and M.A. Burns. Microfabricated Reaction and Separation Systems, *Curr. Opin. Biotechnol.*, 12, pp.92-98. 2001.
- Lahiri, J., L. Isaacs, B. Grzybowski, J.D. Carbeck and G.M. Whitesides. Biospecific Binding of Carbonic Anhydrase to Mixed SAMs Presenting Benzenesulfonamide Ligands: A Model System for Studying Lateral Steric Effects, *Langmuir*, 15, pp.7186-7198. 1999.
- Lao, J.Y., J.Y. Huang, D.Z. Wang and Z.F. Ren. ZnO Nanobridges and Nanonails, *Nano. Lett.*, 3, pp.235-238. 2003.
- Le, Q.T., L. Yan, Y. Gao, M.G. Mason, D.J. Giesen and C.W. Tang. Photoemission Study of Aluminum/Tris-(8-hydroxyquinoline)aluminum and Aluminum/LiF/Tris-(8-hydroxyquinoline)aluminum Interfaces, *J. Appl. Phys.*, 87, pp. 375-379. 2000.
- Lee, S.T., X.Y. Hou, M.G. Mason and C.W. Tang. Energy Level Alignment at Alq/Metal Interfaces, *Appl. Phys. Lett.*, 72, pp. 1593-1595. 1998.
- Leonard, D., M. Krishnamurthy, C.M. Reaves and S.P. Petroff. Direct Formation of Quantum-Sized Dots from Uniform Coherent Islands of InGaAs on GaAs-Surface, *Appl. Phys. Lett.*, 63, pp. 3203-3205, 1993.
- Li, F., H. Tang, J. Andereg and J. Shinar. Fabrication and Electroluminescence of Double-Layered Organic Light-Emitting Diodes with the Al₂O₃/Al Cathode, *Appl. Phys. Lett.*, 70, pp. 1233-1235. 1997.
- Li, G., J. Fan, R. Jiang and Y. Gao. Cross-linking the Linear Polymeric Chains in the ATRP Synthesis of Iron Oxide/Polystyrene Core/Shell Nanoparticles, *Chem. Mater.*, 16, pp. 1835-1837. 2004.
- Li, R., S. Yabe, M. Yamashita, S. Momose, S. Yoshida, S. Yin and T. Sato. UV-Shielding Properties of Zinc Oxide-Doped Ceria Fine Powders Derived via Soft Solution Chemical Routes. *Mater. Chem. Phys.*, 75, pp. 39-44. 20002.
- Li, Z.S., W.Z. Cai, R.Z. Su, G.S. Dong, D.M. Huang, X.M. Ding, X.Y. Hou and X. Wang. S₂Cl₂ Treatment: A New Sulfur Passivation Methods of GaAs Surface, *Appl. Phys. Lett.*, 64, pp. 3425-3427. 1994.
- Lide, D.R. (Ed). *CRC Handbook of the Chemistry and Physics on CD-ROM*, CRC press, Boca Raton, FL, pp. 12-43. 1999.

- Lim, S.L., K.L. Tan and E.T. Kang. Interactions of Evaporated Aluminum Atoms with Polyaniline Films: An X-Ray Photoelectron Spectroscopic Study, *J. Vac. Sci. Technol. A*, 16, pp. 13-20. 1998.
- Linder, M.R. and C.E.D. Chidsey. Alkyl Monolayers Covalently Bonded to Silicon Surfaces, *J. Am. Chem. Soc.*, 115, pp. 12631-12632.
- Linder, M.R., P. Fenster, P.M. Eisenberger and C.E.D. Chidsey. Alkyl Monolayers on Silicon Prepared from 1-Alkenes and Hydrogen-Terminated Silicon, *J. Am. Chem. Soc.*, 117, pp. 3145-3155. 1995.
- Ling, Q.D., E.T. Kang, K.G. Neoh and W. Huang. Synthesis and Nearly Monochromatic Photoluminescence Properties of Conjugated Copolymers Containing Fluorene and Rare Earth Complexes, *macromolecules*, 36, pp. 6995-7003. 2003.
- Little, T.W., and F. S. Ohuchi. Chemical Interaction of NF_3 Ion Beam and Plasma with Si (Part I): X-Ray Photoelectron Spectroscopy Studies, *Surf. Sci.*, 445, pp. 235-242. 2000.
- Loo, Y.-L., D.V. Lang, J.A. Rogers and J.W.P. Hsu. Electrical Contacts to Molecular Layers by Nanotransfer Printing, *Nano. Lett.*, 3, pp. 913-917. 2003.
- Lunt, S.R., G.N. Ryba, P.G. Santangelo and N.S. Lewis. Chemical Studies of the Passivation of GaAs Surface Recombination Using Sulfides and Thiols, *J. Appl. Phys.*, 70, pp. 7449-7467. 1991.
- Mackie, N.M., D.G. Caster and E.R. Fisher. Characterization of Pulsed Plasma-Polymerized Aromatic Films, *Langmuir*, 14, pp. 1227-1235. 1998.
- Madhukar, A., S. Lu, A. Konkar, Y. Zhang, M. Ho, S.M. Hughes and A.P. Alivisatos. Integrated Semiconductor Nanocrystal and Epitaxial Nanostructure Systems: Structural and Optical Behavior, *Nano. Lett.*, 5, pp. 479-482. 2005.
- Maier, G. Low Dielectric Constant polymer for Microelectronics, *Prog. Poly. Sci.*, 26, pp 3-65. 2001.
- Mansky, P., Y. Liu, E. Huang, T.P. Russell and C. Hawker. Controlling Polymer-Surface Interactions with Random Copolymer Brushes, *Science*, 275, pp. 1458-1460. 1997.
- Mason, M.G., C.W. Tang, L.S. Hung, P. Raychaudhuri, J. Madathil, D.J. Giesen, L. Yan, Q.T. Le, Y. Gao, S.T. Lee, L.S. Liao, L.F. Cheng, W.R. Salaneck, D.A. dos Santos and J.L. Bredas. Interfacial Chemistry of Alq_3 and LiF with Reactive Metals, *J. Appl. Phys.*, 89, pp. 2756-2765. 2001.

- Matyjaszewski, K. and J. Xia. Atom Transfer Radical Polymerization, *Chem. Rev.*, 101, pp. 2921-2990. 2001.
- Matyjaszewski, K., M. Wei, J. Xia and S.G. Gaynor. Atom Transfer Radical Polymerization of Styrene Catalyzed by Copper Carboxylate Complexes, *Macromol. Chem. Phys.*, 30, pp. 2289-2292. 1998.
- Matyjaszewski, K., P.J. Miller, N. Shukla, B. Immaraporn, A. Gelman, B.B. Luokala, T.M. Siclovan, G. Kickelbick, T. Vallant, H. Hoffmann and T. Pakula. Polymer at Interface: Using Atom Transfer Radical Polymerization in the Controlled Growth of Homopolymers and Block Copolymers from Silicon Surfaces in the Absence of Untethered Sacrificial Initiator, *Macromolecules*, 32, pp. 8716-8724. 1999.
- Meulenkamp, E.A. Synthesis and Growth of ZnO Nanoparticles. *J. Phys. Chem. B*, 102, pp. 5566-5572. 1998.
- McGehee, M.D., T. Bergstedt, C. Zhang, A.P. Saab, M.B. O'Regan, G.C. Bazan, V.I. Srdanov and A.J. Heeger. Narrow Bandwidth Luminescence from Blends with Energy Transfer from Semiconducting Conjugated Polymer to Europium Complexes, *Adv. Mater.*, 11, pp. 1349-1354. 1999.
- Milani, B., A. Scarel, G. Mestroni, S. Gladioli, R. Taras, C. Carfagna and L. Mosca. Very Stable Palladium(II)-(N-N) Catalysts for the Synthesis of High-Molecular-Weight CO/Styrene Polyketones, *Organometallics*, 21, pp. 1323-1325. 2002.
- Mitsuya, M. and N. Sato. Energy Shift for Core Electron Levels of Chemisorbed Molecules Observed by X-Ray Photoelectron Spectroscopy in the Course of Monolayer Growth on a Si(100) Surface, *Langmuir*, 15, pp. 2099-2102. 1999.
- Miyaura, N. and A. Suzuki. Palladium-Catalyzed Cross-Coupling Reactions of Organoboron Compounds, *Chem. Rev.*, 95, pp. 2457-2483. 1995.
- Mo, Y.W., D.E. Savage, B.S. Swartzentruber and M.G. Lagally. Kinetic Pathway in Stranski-Krastanov Growth of Ge on Si(001), *Phys. Rev. Lett.*, 65 pp. 1020-1023. 1990.
- Moison, J.M., F. Houzay, F. Barthe, L. Leprince, E. André and O. Vatel. Self-Organized Growth of Regular Nanometer-Scale InAs Dots on GaAs. *Appl. Phys. Lett.*, 64, pp. 196-198. 1994.
- Moulder, J.F., W.F. Stickle, P.E. Sobol and K.D. Bomben. In *X-ray Photoelectron Spectroscopy*, J. Chastian, Ed., Perkin-Elmer: Eden Prairie, MN, pp 41 and 95. 1992.
- Munro, H.S., R.J. Ward, M.C. Davies and R.D. Short. The Characterization of Plasma Polymers by XPS and Static SIMS, *Polymer*, 34, pp. 2250-2255. 1993.

- Nguyen, T.P., K. Amgaard, M. Cailler, V.H. Tran and S. Lefrant. XPS Analysis of Thermal and Plasma Treated Polyparaphenylene-vinylene Thin Films and Their Interface Formed with Aluminum Layer, *Synth. Met.*, 69, pp. 495-496. 1995.
- Nguyen, T.P., V. Massardier, V.H. Tran and A. Guyot. Studies of the Polymer-Metal Interface in Metal-PPV-Metal Devices, *Synth. Met.*, 55, pp. 235- 240. 1993.
- Niemeyer, C.M. Nanoparticles, Proteins, and Nucleic Acids: Biotechnology Meets Materials Science, *Angew. Chem. Int. Ed.*, 40, pp. 4128-4158. 2001.
- Noguera, C. *Physics and Chemistry at Oxide Surfaces*, Chapter 6, Cambridge University Press, Cambridge, 1996.
- Norton, D.P., Y.W. Heo, M.P. Ivill, K. Ip, S.J. Pearton, M.F. Chisholm and T. Steiner. ZnO: Growth, Doping & Processing, *Materialstoday*, 7(6), pp. 34-40. 2004.
- Nuss, S., H. Böttcher, H. Wurm and M.L. Hallensleben. Gold Nanoparticles with Covalently Attached Polymer Chains. *Angew. Chem. Int. Ed.*, 40, pp. 4016-4018. 2001.
- Ohta, H., M. Hirano, K. Nakahara, H. Maruta, T. Tanabe, M. Kamiya, T. Kamiya and H. Hosono. Fabrication and Photoresponse of a pn-Heterojunction Diode Composed of Transparent Oxide Semiconductors, p-NiO and n-ZnO, *Appl. Phys. Lett.*, 83, pp. 1029-1031. 2003.
- Ohta, H. and H. Hosono. Transparent Oxide Optoelectronics, *Materialstoday*, 7(6), pp. 42-51. 2004.
- Oshima, M., T. Scimeca, Y. Watanabe, H. Oigawa and Y. Nannichi. Oxidation of Sulfur-Treated GaAs Surfaces Studied by Photoluminescence and Photoelectron Spectroscopy, *Jpn. J. Appl. Phys.*, 32, pp. 518-522. 1993.
- Paget, D., J.E. Bonnet, V.L. Berkovits, P. Chiaradia and J. Avila. Sulfide-Passivated GaAs(001). I. Chemistry Analysis by Photoemission and Reflectance Anisotropy Spectroscopies, *Phys. Rev. B.*, 53, pp. 4604-4614. 1996.
- Paget, D., A.O. Gusev and V.L. Berkovits. Sulfide-Passivated GaAs (001). II. Electronic Properties, *Phys. Rev. B*, 53, pp.4615-4622. 1996.
- Parks, G.A. The Isoelectric Points of Solid Oxides, Solid Hydroxides, and Aqueous Hydroxo Complex Systems, *Chem. Rev.*, 65, pp. 177-198. 1965.
- Peng, X., J. Wickham and A.P. Alivisatos. Kinetics of II-VI and III-V Colloidal Semiconductor Nanocrystal Growth: "Focusing" of Size Distributions, *J. Am. Chem. Soc.*, 120, pp. 5343-5244. 1998.

- Percec, V., B. Barboin and M. van der Sluis. Self-Regulated Phase Transfer of Cu₂O/bpy, Cu(0)/bpy, and Cu₂O/Cu(0)/bpy Catalyzed "Living" Radical Polymerization Initiated with Sulfonyl Chlorides, *Macromolecules*, 31, pp. 4053-4056. 1998.
- Pusel, A., U. Wetterauer and P. Hess. Photochemical Hydrogen Desorption from H-Terminated Silicon(111) by VUV photons, *Phys. Rev. Lett.*, 81, pp. 645-648. 1998.
- Pyun, J., T. Kowalewski and K. Matyjaszewski. Synthesis of Polymer Brushes Using Atom Transfer Radical Polymerization, *Macromol. Rapid. Commun.*, 24, pp. 1043-1059. 2003.
- Pyun, J., K. Matyjaszewski, T. Kowalewski, D. Savin, G. Patterson, G. Kickelbick and N. Huesing. Synthesis of Well-Defined Block Copolymers Tethered to Polysilsesquioxane Nanoparticles and their Nanoscale Morphology on Surfaces. *J. Am. Chem. Soc.*, 123, pp. 9445-9446. 2001.
- Queffele, J., S.G. Gaynor and K. Matyjaszewski. Optimization of Atom Transfer Radical Polymerization Using Cu(I) Tri(2-(dimethylamino)ethyl)amine as a Catalyst, *Macromolecules*, 33, pp. 8629-8639. 2000.
- Rastelli, A., S. Stufler, A. Schliwa, R. Songmuang, C. Manzano, G. Costantini, K. Kern, A. Zrenner, D. Bimberg and O G. Schmidt. Hierarchical Self-assembly of GaAs/AlGaAs Quantum Dots, *Phys. Rev. Lett.*, 92, pp. 166104. 2004.
- Rao, V.J., V. Manorama and S.V. Bhoraskar. Passivation of Pinned n-GaAs Surface by Plasma-Polymerized Thin Film, *Appl. Phys. Lett.*, 54, pp. 1799-1801. 1989.
- Rogach, A.L., D.V. Talapin, E.V. Shevchenko, A. Kornowski, M. Haase and H. Weller. Organization of Matter on Different Size Scales: Monodisperse Nanocrystals and Their Superstructures, *Adv. Funct. Mater.*, 12, pp. 653-664. 2002.
- Sa, S.-H., M.-G. Kang, H.-H. Park and K.-S. Suh. The Investigation on the Structure Distribution of Passivated GaAs(100) Surface After (NH₄)₂S_x Treatment, *Surf. Coat. Technol.*, 100-101, pp.234-237. 1998.
- Sacher, E. Fluoropolymer Metallization for Microelectronic Applications, *Prog. Surf. Sci.*, 47, pp. 273-300. 1994.
- Sackmann, E. and M. Tanaka, Supported Membranes on Soft Polymer Cushions: Fabrication, Characterization and Applications, *Trends Biotechnol.*, 18, pp. 58-64. 2000.
- Sakohara, S., M. Ishida and M.A. Anderson. Visible Luminescence and Surface Properties of Nanosized ZnO Colloids Prepared by Hydrolyzing Zinc Acetate. *J. Phys. Chem. B*, 102, pp. 10169-10175. 1998.

- Salaneck, W.R., M. Logdlund, M. Fahlman, G. Greczynski and T. Kuglur. The Electronic Structure of Polymer-Metal Interfaces Studied by Ultraviolet Photoelectron Spectroscopy, *Mater. Sci. Eng. R*, 34, pp. 121-146. 2001.
- Salaneck, W.R., S. Stafström and J.L. Brédas. *Conjugated Polymer Surfaces and Interfaces*, pp. 110-126. Cambridge University Press, Cambridge, 1996.
- Sandroff, C.J., M.S. Hedge and C.C. Chang. Structure and Stability of Passivating Arsenic Sulfide Phase on GaAs Surfaces, *J. Vac. Sci. Technol.*, 7, pp. 841-844. 1989.
- Sandroff, C.J., M.S. Hegde, L.A. Farrow, C.C. Chang and J.P. Harbison. Electronic Passivation of GaAs Surfaces Through the Formation of Arsenic—Sulfur Bonds, *Appl. Phys. Lett.*, 54, pp. 362-364. 1989.
- Sandroff, C.J., R.N. Nottenburg, J.-C. Bischoff and R. Bhat. Dramatic Enhancement in the Gain of a GaAs/AlGaAs Heterostructure Bipolar Transistor by Surface Chemical Passivation, *Appl. Phys. Lett.*, 51, pp.33-35. 1987.
- Sankey, O.F., R.E. Allen, S.F. Ren and J.D. Dow. Dangling Bonds and Schottky Barriers. *J. Vac. Sci. Technol. B*, 3, pp. 1162-1166. 1985.
- Schmitt, J., P. Mächtle, D. Eck, H. Möhwald and C.A. Helm. Preparation and Optical Properties of Colloidal Gold Monolayers, *Langmuir*, 15, pp. 3256-3266. 1999.
- Seker, F., K. Meeker, T. F. Kuech and A.B. Ellis, Surface Chemistry of Prototypical Bulk II-VI and III-V Semiconductors and Implications for Chemical Sensing, *Chem. Rev.*, 100, pp. 2505-2536. 2000.
- Seung, H.Y. and J.E. Whitten. The Interaction of Aluminum with a Urethane-substituted Polythiophene with Electroluminescence Applications, *Synth. Met.*, 114, pp. 305-312. 2000.
- Shah, R.R., D. Merreceyes, M. Husemann, I. Rees, N.L. Abbott, C.J. Hawker and J.L. Hedrick. Using Atom Transfer Radical Polymerization to Amplify Monolayers of Initiators Patterned by Microcontact Printing into Polymer Brushes for Pattern Transfer. *Macromolecules*, 33, pp. 597-605. 2000.
- Shaporenko, A., K. Adlkofer, L.S.O. Johansson, M. Tanaka and M. Zharnikov. Functionalization of GaAs Surfaces with Aromatic Self-Assembled Monolayers: A Synchrotron-Based Spectroscopic Study, *Langmuir*, 19, pp. 4992-4998. 2003.
- Sheen, C.W., J.X. Shi, J. Martensson, A.N. Parikh and D.L. Allara. A New Class of Organized Self-Assembled Monolayers: Alkene Thiols on GaAs(100), *J. Am. Chem. Soc.*, 114, pp. 1514-1515. 1992.

Shen, C., A. Kahn and J. Schwartz. Chemical and Electrical Properties of the Interfaces between Magnesium and Aluminum and Tris-(8-hydroxyquinolino)aluminum, *J. Appl. Phys.*, 89, pp. 449-459. 2001.

Shen, C., I.G. Hill, A. Kahn and J. Schwartz. Organometallic Chemistry at the Magnesium-Tris(8-hydroxyquinolino)aluminum Interface, *J. Am. Chem. Soc.*, 122, pp. 5391-5392. 2000.

Shur, M. Introduction to Semiconductor Technology, GaAs and Related Compounds, C.T. Wang., Ed., pp.27-50. John Wiley: New York, 1990.

Sidorenko, A., S. Minko, K. Schenk-Meuser, H. Duschner and M. Stamm. Switching of polymer brushes, *Langmuir*, 15, pp. 8349-8355. 1999.

Sinha, R.P.N. New Synthesis Strategies, *Sci. Culture*, 25, pp.494-528. 1960.

Spindt, C.J., R.S. Besser, R. Cao, K. Miyano, C.R. Helms and W.E. Spicer. Photoemission Study of the Band Bending and Chemistry of Silicon Sulfide on GaAs(100), *Appl. Phys. Lett.*, 54, pp. 1148-1150. 1989.

Starkweather, H.W., R.C. Ferguson, D.B. Chane and J.M. Minor. Infrared spectra of amorphous and crystalline poly(tetrafluoroethylene), *Macromolecules*, 18, pp. 1684-1686. 1985.

Sung, M.M., G.J. Kluth, O.W. Yauw and R. Maboudian. Thermal Behavior of Alkyl Monolayers on Silicon Surfaces, *Langmuir*, 13, pp. 6164-6168. 1997.

Sze, S.M. *Physics of Semiconductor Devices*, 2nd ed., John Wiley & Sons, New York, 1981.

Szuber, J., E. Bergignat, G. Hollinger, A. Polakowska and P. Koscielniak. XPS study of the Surface Fermi level of (NH₄)₂S_x-Passivated GaAs(100) Surface. *Vacuum*, 67, pp. 53-58. 2002.

Teare, D.O.H., C.G. Spanos, P. Ridley, E.J. Kinmond, V. Roucoules, J.P.S. Badyal, S.A. Brewer, S. Coulson and C. Willis. Pulsed Plasma Deposition of Super-Hydrophobic Nanospheres, *Chem. Mater.*, 14, pp. 4566-4571. 2002.

Takahagi, T., I. Nagai, A. Ishitani, H. Kuroda and Y. Nagasawa. The Formation of Hydrogen Passivated Silicon Single-Crystal Surface Using Ultraviolet Cleaning and HF Etching. *J. Appl. Phys.*, 64, pp. 3516-3521. 1988.

Tang, H., F. Li and J. Shinar. Bright High Efficiency Blue Organic Light-Emitting Diodes with Al₂O₃/Al Cathodes, *Appl. Phys. Lett.*, 71, pp. 2560-2562. 1997.

- Thole, B.T., G. van der laan, J.C. Fuggle, G.A. Sawatzky, R.C. Karnatak and J.-M. Esteve. $3d$ X-Ray-Absorption Lines and the $3d^9 4f^{n+1}$ Multiplets of the Lanthanides, *Phys. Rev. B*, 32 pp. 5107-5118. 1985.
- Uwamino, Y., T. Ishizuka and H. Yamatera. X-Ray Photoelectron Spectroscopy of Rare-Earth Compounds, *J. Electron Spectrosc. Relat. Phenom.*, 34, pp. 67-78. 1984.
- Wade, C.P. and C.E.D. Chidsey. Etch-Pit Initiation by Dissolved Oxygen on Terraces of H-Si(111), *Appl. Phys. Lett.*, 71, pp. 1679-1681. 1997.
- Weck, M., J.J. Jackiw, R.R. Rossi, P.S. Weiss and R.H. Grubbs. Ring-Opening Metathesis Polymerization from Surfaces, *J. Am. Chem. Soc.*, 121, pp. 4088-4089. 1999.
- Weinberger, B.R., G.G. Peterson, T.C. Eschrich and H.A. Krasinski. Surface Chemistry of HF Passivated Silicon: X-Ray Photoelectron and Ion Scattering Spectroscopy Results. *J. Appl. Phys.*, 60, pp. 3232-3234. 1986.
- Wieder, H.H. VLSI Electronics Microstructure, 10th ed., edited by N.G. Einspruch and R.S. Bauer. pp. 201-236, Academic London. 1985.
- Woodworth, B.E., Z. Metzner and K. Matyjaszewski. Copper Triflate as a Catalyst in Atom Transfer Radical Polymerization of Styrene and Methyl Acrylate. *Macromolecules*, 31, pp. 7999-8004. 1998.
- Wright, P.J. and K.C. Saraswat. The Effect of Fluorine in Silicon Dioxide Gate Dielectrics, *IEEE Trans. Electron Devices*, 36, pp. 879-889. 1989.
- Vanheusden, K., W. Warren, C.H. Seager, D.R. Tallant, J.A. Voigt and B.E. Gnade. Mechanisms behind Green Photoluminescence in ZnO Phosphor Powders, *J. Appl. Phys.*, 79, pp. 7983-7990. 1996.
- Vestal, C.R. and Z. J. Zhang. Atom Transfer Radical Polymerization Synthesis and Magnetic Characterization of MnFe₂O₄/Polystyrene Core/Shell Nanoparticles, *J. Am. Chem. Soc.*, 124, pp. 14312-14313. 2002.
- van Dijken, A., A.H. Janson, M.H.P. Smitsmans, D. Vanmaekelbergh and A. Meijerink. Size-Selective Photoetching of Nanocrystalline Semiconductor Particles, *Chem. Mater.*, 10, pp. 3513-3522. 1998.
- von Werne, T. and T.E. Pattern. Preparation of Structurally Well-Defined Polymer-Nanoparticle Hybrids with Controlled/Living Radical Polymerizations. *J. Am. Chem. Soc.*, 121, pp. 7409-7410. 1999.
- von Werne, T. and T.E. Pattern. Atom Transfer Radical Polymerization from Nanoparticles: A Tool for the Preparation of Well-Defined Hybrid Nanoparticles and

for Understanding the Chemistry of Controlled/"Living" Radical Polymerization from Surface. *J. Am. Chem. Soc.*, 123, pp. 7497-7505. 2001.

Vondrak, T. and X.-Y. Zhu. Dissociation of a Surface Bond by Direct Optical Excitation: H-Si(100), *Phys.Rev. Lett.*, 82, pp. 1967-1970. 1999.

Wang, Y., X. Teng, J. Wang and H. Yang. Solvent-Free Atom Transfer Radical Polymerization in the Synthesis of Fe₂O₃@Polystyrene Core-Shell Nanoparticles. *Nano Lett.*, 3, pp. 789-793. 2003.

Wang, Z.L. Functional Oxide Nanobelts: Materials, Properties and Potential Applications in Nanosystems and Biotechnology. *Annu. Rev. Phys. Chem.*, 55, pp. 159-196. 2004.

Woggon, U., E. Herz, O. Schöps, M.V. Artemyev, C. Arens, N. Rousseau, D. Schikora, K. Lischka, D. Litvinov and D. Gerthsen. Hybrid Epitaxial-Colloidal Semiconductor Nanostructures, *Nano. Lett.*, 5, pp. 483-490. 2005

Xia, J., S.G. Gaynor and K. Matyjaszewski. Controlled/"living" Radical Polymerization. Atom Transfer Radical Polymerization of Acrylates at Ambient Temperature. *Macromolecules*, 31, pp.5958-5959. 1998.

Xia, Y. N. and G.M. Whitesides. Soft Lithography, *Angew. Chem. Int. Ed.*, 37, pp. 551-575. 1998.

Xu, D., E. T. Kang, K. G. Neoh, Y. Zhang, A. A. O. Tay, S. S. Ang, M. C. Y. Lo and K. Vaidyanathan. Selective Electroless Plating of Copper on (100)-Oriented Single Crystal Silicon Surface Modified by UV-Induced Coupling of 4-Vinylpyridine with the H-Terminated Silicon. *J. Phys. Chem. B*, 106, pp.12508-12516. 2002.

Yan, L., M.G. Mason, C.W. Tang and Y. Gao. Photoemission Study of Energy Alignment at the Metal/Alq₃ Interfaces, *Appl. Phys. Lett.*, 175-176, pp. 412-418. 2001.

Yang, G.H., S.W. Oh, E.T. Kang and K.G. Neoh. Plasma Polymerization and Deposition of Linear, Cyclic and Aromatic Fluorocarbons on (100)-oriented Single Crystal Silicon Substrates, *J. Vac. Sci. Technol. A*, 20, pp. 1955-1963. 2002.

Yang, G.H., Y. Zhang, E.T. Kang, K.G. Neoh, W. Huang and J.H. Teng. Surface Passivation of (100)-Oriented GaAs via Plasma Deposition of an Ultrathin S-Containing Polymer Film and Its Effect on Photoluminescence, *J. Phys. Chem.*, 107, pp. 8592-8598. 2003.

Yasuda, H. Plasma Polymerization, pp. 136-230. Academic Press: London, 1985.

Yasuda, H. and T.S. Hsu. Some Aspects of Plasma Polymerization of Fluorine-Containing Organic Compounds, *J. Poly. Sci.*, 15, pp. 2411-2425. 1977.

Yi, J.W., Y.H. Lee and B. Farouk. Low Dielectric Fluorinated Amorphous Carbon Thin Films Grown From C₆F₆ and Ar Plasma, *Thin Solid Films*, 374, pp. 103-108. 2000.

Yoshikawa, C., A. Goto and T. Fukuda. Quantitative Comparison of Theory and Experiment on Living Radical Polymerization Kinetics. 1. Nitroxide-Mediated Polymerization, *Macromolecules*, 35, pp. 5801-5907. 2002.

Zhan, X.W., Y.Q. Liu, D.B. Zhu, W.T. Huang and Q.H. Gong. Large Femtosecond Third-Order Nonlinear Optical Response in a Novel Donor-Acceptor Copolymer Consisting of Ethynylfluorene and Tetraphenyldiaminobiphenyl Units, *Chem. Mater.*, 13, pp. 1540-1544. 2001.

Zhang, Y., E.T. Kang, K.G. Neoh, W. Huang, A.C.H. Huan, H. Zhang and R.N. Lamb. Surface Modification of Polyimide Films via Plasma Polymerization and Deposition of Allylpentafluorobenzene, *Polymer*, 43, pp. 7279-7288. 2002.

Zhang, Y., G.H. Yang, E.T. Kang, K.G. Neoh, W. Huang, A.C.H. Huan and D.M.Y. Lai. Characterization of Fluoropolymer Films Deposited by Magnetron Sputtering of Poly(Tetrafluoroethylene) and Plasma Polymerization of Heptadecafluoro-1-decene (HDFD) on (100)-Oriented Single-Crystal Silicon Substrates, *Surf. Interface Anal.*, 34 pp. 10-18. 2002.

Zhao, B. and W.J. Brittain. Synthesis of Tethered Polystyrene-*block*-Poly(methylmethacrylate) Monolayer on a Silicate Substrate by Sequential Carbocationic Polymerization and Atom Transfer Radical Polymerization. *J. Am. Chem. Soc.*, 121, pp. 3557-3558. 1999.